FORWARD AND INVERSE MODELING OF RAYLEIGH WAVES FOR NEAR SURFACE INVESTIGATION

by
Swastika B. Nevaskar

SUBMITTED IN PARTIAL FULFILLMENT OF THE
REQUIREMENTS FOR THE DEGREE OF
DOCTOR OF PHILOSOPHY

AT

DALHOUSIE UNIVERSITY
HALIFAX, NOVA SCOTIA
MARCH 2011

DALHOUSIE UNIVERSITY

DEPARTMENT OF CIVIL AND RESOURCE ENGINEERING

The undersigned hereby certify that they have read and recommend to the Faculty of Graduate Studies for acceptance a thesis entitled "**FORWARD AND INVERSE MODELING OF RAYLEIGH WAVES FOR NEAR SURFACE INVESTIGATION**" by **Swastika B. Nevaskar** in partial fulfillment of the requirements for the degree of **Doctor of Philosophy**.

Dated: March 23, 2011

External Examiner: Derek Apel

Research Supervisor: Stephen Butt

Examining Committee: Phillip Bording

Donald Jones

Maria Rockwell

DALHOUSIE UNIVERSITY

Date: **March 23, 2011**

Author: **Swastika B. Nevaskar**

Title: **FORWARD AND INVERSE MODELING OF RAYLEIGH WAVES FOR NEAR SURFACE INVESTIGATION**

Department: **Civil and resource engineering**

Degree: **Ph.D.** Convocation: **May** Year: **2011**

Signature of Author

This dissertation is dedicated to my parents, Anjoli and Munin Sarmah.

Table of Contents

List of Tables

List of Figures

Abstract

This dissertation addresses forward and inverse modeling of Rayleigh waves for near surface investigation. Results were obtained by imaging abandoned mine openings using Rayleigh waves in the laterally inhomogeneous medium. The efficient staggered grid stencil method to solve elastic wave equations using 2-D finite difference technique is presented. This numerical scheme is used to conduct a series of parametric studies on the propagation of Rayleigh waves. The first parametric study was conducted on a flat layered model of increasing and decreasing velocity with depth. A Rayleigh waves dispersion curve is found to be sensitive on a layer's depth up to half of the minimum wavelength of Rayleigh waves. The phase velocity in the dispersion curve of Rayleigh waves is inversely and directly proportional to the frequency, depending on velocity increase or decrease with depth. The parametric study was carried out by introducing dipping layers in the model with increasing dip. The front (near the shot point) and back (at the end of receiver line) shot records are different if the subsurface contains dip. Dispersion is observed in near offset for down dip and in the far offset for up dip, computed from front and back shots respectively. Finally, a parametric study looked at subsurface anomalies with different shapes and sizes as well as their material properties. A Rayleigh wave is sensitive to very high material contrast and very low material contrast of the anomaly from it surrounding medium. The presence of a low material contrast anomaly from the surrounding medium traps the energy which causes reverberation. A Rayleigh wave is sensitive to an anomaly which is placed within the depth between one-third to half of minimum wavelength of Rayleigh wave from the surface. In order to resolve lateral heterogeneity, a new method is developed in this research which allows localization of the multichannel record in different panels. The dispersion curve of Rayleigh waves is computed in each panel using the slant stack technique. On the basis of parametric studies, an innovative inversion algorithm has been developed to minimize the error norm; "the sum of the squares of the difference of reference and model dispersion curves" in an iterative way using a Very Fast Simulated Re-annealing (VFSR) technique.

List of Symbols and Abbreviations Used

AARW	Attenuation Analysis of Rayleigh Waves
FK	Frequency Wavenumber
LMO	Linear Move Out
MASW	Multichannel Analysis of Surface Waves
P	Primary wave
p	Ray parameter
PML	Perfectly Matched Layer
S	Secondary wave
SASW	Spectral Analysis of Surface Waves
SIG	Subsurface Imaging Group
VFSR	Very Fast Simulated Re-annealing
V_p	Velocity of P wave
V_s	Velocity of S wave
$\triangle t$	Sampling time
$\triangle x = \triangle z = h$	Grid spacing
$S(t)$	Linear sweep source
$S_r(t)$	Numerical modeling source
f_1	Lowest frequency considered in the sweep source
f_2	Highest frequency considered in the sweep source
f_{max}	Maximum frequency of the numerical modeling source
T	Length of the sweep source
v_{min}	Minimum velocity for slant stacking
v_{max}	Maximum velocity for slant stacking
ν	Poisson's ratio
λ	Wavelength
X_i	Parameters to be updated in VFSR inversion technique
LB_i	Lower bound of X_i
UB_i	Upper bound of X_i

S_i	Sensitivity of each parameter X_i
T_{ik}	Temperature of each parameter X_i for iteration k
σ_{ij}	Stress tensor, where where $i, j = x, y, z$
$\varepsilon_{ij} = \varepsilon_{ji}$	Strain tensor, where where $i, j = x, y, z$
$\mathbf{C}$	Stiffness matrix
E	Young's modulus
K	Bulk modulus
ω	Wavenumber
f	Frequency
v_x	Velocity vector along x direction
v_z	Velocity vector along z direction
b	Lightness or inverse of density
F	Fitness function
A_{ref}	Amplitude array of reference dispersion curve
A_{mod}	Amplitude array of model dispersion curve
dv	Velocity sample
df	Frequency sample
U	Upper bound
L	Lower bound
Up	Upper bound of P wave velocity
Lp	Lower bound of P wave velocity
Us	Upper bound of S wave velocity
Ls	Lower bound of S wave velocity

Acknowledgements

I owe my deepest gratitude to my supervisor Dr. Stephen Butt for his continuous support, help, and encouragement in my PhD program. Not only Dr. Butt did expose me to an interesting area of study but his guidance and valuable suggestions, sound advice helped me during my PhD research to reach the final goal.

My sincere thanks goes to Dr. Phillip Bording, an external committee member who enhanced my understanding of numerical modeling and inversion and programming skills. Also, I would like to extend thanks to Dr. Charles Hurich who provided additional inspiration for creative and innovative approach to tackle problems. I wish to thank Dr. Andrea Atle for his great computational help. I collaborated with him to develop the code for inverse modeling of Rayleigh waves.

I would like to further thanks to my colleagues for their support throughout my doctoral work. In particular Chaoqiang Xu, Lujie Zhan and Waheduzzaman Talukder, for many times we shared knowledge and learning. I would like to thank Dawna Greening from Memorial University for proofreading and reviewing my dissertation.

Finally, a heartfelt thanks to my entire extended family for providing a loving and positive environment, my sister, Chandana Kausik Boruah, my uncles and aunties, Gokul and Deepali Sarma were particularly very supportive. A special thanks to my loving parents, Anjoli and Munin Sarmah who always supported and encouraged me to do my best in all aspects of life. At last, my husband Bhalchandra for his understanding, endless patience, and encouragement when it was most required.

Chapter 1

Introduction

1.1 Motivation

Near surface anomalies, such as mine cavities, tunnels etc. occur due to near surface engineering activities. They are very common in nature and have significantly different elastic properties from their surrounding medium. The transition from a normal to an anomalous zone may be either abrupt or gradual. Anomalies such as mine cavities or limestone cavities have very low material contrast, whereas anomalies such as buried boulders have very high material contrast from the rest of the medium. Near surface anomalies with low material contrast from the surrounding medium can cause a significant hazard of subsidence. On the other hand, near surface anomalies with very high material contrast from the surrounding medium may restrict the use of land for construction purposes. Hence, the presence of anomalies near the surface is not only a concern for civil, geotechnical and geoenvironmental engineering, but may also cause threats to public safety. In order to locate these shallow anomalies, it is crucial to develop a precise and cost-effective method using better imaging resolution techniques. Near surface anomalies leave their foot prints in different forms in the multichannel record of Rayleigh waves data. The size, shape, and depth of the anomaly from the surface affects Rayleigh waves phase velocities for those frequencies. A near surface anomaly also reveals its presence in the form of reflection, diffraction, and reverberation of Rayleigh wave energy in the multichannel record. The S wave velocity stiffness profile which can be generated from Rayleigh wave field data is found to be very effective in detecting and locating shallow subsurface anomalies. From the S wave velocity stiffness profile the lack of shear waves in air and water help to identify air or water filled anomalies (Al-Shayea, 1994). Therefore, consideration should be given to use seismic methods involving Rayleigh wave propagation to determine shear stiffness for near surface anomaly detection purposes. There are

both invasive and non-invasive seismic methods. Invasive methods require bore holes and may cause damage to the region. Large scale applications by drilling many holes are time consuming and expensive. Non-invasive methods, however, are conducted from a free surface and include: P and S waves seismic reflection and refraction, Spectral Analysis of Surface Waves (SASW), Multichannel Analysis of Surface Waves (MASW), etc. Even though the non-invasive methods are not free from uncertainties, they have proven to be more efficient and less expensive than invasive methods. The main advantage of non-invasive methods, however, is that large surface regions may be tested in a short period of time, without damaging the experimental area. The SASW/MASW are certainly becoming more popular non-invasive methods of soil characterization in civil engineering (Foti, 2000) and in stability analysis of pavements (Nazarian, 1984). These methods use Rayleigh waves to determine the S wave velocity stiffness profile. Elastic seismic numerical modeling and numerical inversion play an important role in validating the results from reference data.

1.2 Research Objective

The imaging and analysis of near surface anomalies to avoid possible hazard is inspired by the existing MASW technique. This method basically consists of three steps: data collection from the field, generation of a dispersion curve, and finally, inversion of the dispersion curve to obtain a S wave velocity stiffness profile. Traditionally, the MASW technique assumes that subsurface layers are horizontally flat when computing Rayleigh waves dispersion curves. The presence of different structures, like dipping layers or lateral heterogeneity in the subsurface, can invalidate this assumption of flat layers. Hence, this method needs to be improved to make it useful for imaging complex subsurface geometries.

The focus of this research is to improve the methodology used to image near surface anomalies using Rayleigh waves. To accomplish this goal, forward modeling of Rayleigh waves will be carried out by developing a 2-D finite difference algorithm which allows for a general inhomogeneous parametrized models. These general models will allow for the development of a new inversion method that overcomes the difficulties of flat layer assumption. The finite difference modeling of Rayleigh waves will

then be used to conduct a parametric study to see the effect of different parameters on Rayleigh wave propagation by analyzing Rayleigh wave dispersion curves. Several elastic parameters of the subsurface can be roughly estimated from Rayleigh wave dispersion curves. Therefore, it is crucial to compute the dispersion curves accurately. There are several techniques to compute Rayleigh wave dispersion curves, but most of the existing techniques only work for flat layered models. As a result, an extensive literature review to find or modify existing methods for computing dispersion curves for laterally heterogeneous medium is a focus of this research. An inversion algorithm will be developed on the basis of the parametric study conducted to image the Stellarton mine site near Nova Scotia. In this inversion, the least sensitive parameters of the Rayleigh wave dispersion curve will be fixed and the most sensitive parameters will be updated to minimize the objective function. In general, the creative objective of this research can be stated as:

- 2-D finite difference modeling of Rayleigh waves propagating in inhomogeneous or non flat layered models.
- Decomposing multichannel data into horizontal panels to compute localize dispersion curves. This new approach resolves lateral heterogeneity in the subsurface.
- Use VFSR, a non linear optimization method for inverse modeling of Rayleigh waves for obtaining subsurface image.

1.3 Thesis Outline

This dissertation has been organized into eight chapters. The first three chapters discuss the properties of Rayleigh waves and their usefulness in near surface imaging. The next four chapters are on methodology, sensitivity analysis of different parameters on Rayleigh wave propagation, and on Rayleigh wave inversion for near surface imaging. The last chapter contains conclusions.

In more detail, Chapter 2 discusses literature sources which were reviewed to develop an improve methodology for near surface imaging using Rayleigh waves. Numerical modeling of Rayleigh waves, various methods to compute dispersion curves,

parametric study on Rayleigh wave propagation and finally the literature sources on numerical inversions are presented.

Chapter 3 theorizes on elastic wave propagation and the derivation of Rayleigh waves from the elastic wave equation. The properties of Rayleigh waves which make them useful for near surface imaging are also reviewed. Different methods which use Rayleigh waves for near surface imaging and their advantages and disadvantages are discussed. The techniques to compute dispersion curves for different subsurface conditions are studied.

Chapter 4 presents on the methodology used in this research, beginning with the formulation of a 2-D finite difference model with staggered grid stencil to model Rayleigh waves. The slant stack technique adopted to compute localized Rayleigh wave dispersion curves is also discussed. The formulation of a fitness function for the inversion is also presented, and finally, the mathematical formulation of a VFSR technique is derived along with a flow chart of the associated computer code.

Chapter 5 is devoted to detailed parametric studies of the effects of a layer's depth and dip on Rayleigh wave propagation. There are three parametric studies of layer depth: increasing velocity with depth, decreasing velocity with depth, and an alternate velocity layer. The synthetic seismogram and dispersion curve for each case is analyzed. The effect of layer dip on Rayleigh waves is studied by increasing the layer's dip. The front and back shot records for each dipping model are presented. Multichannel data are divided into sequences of traces in a lateral direction in order to compute a localized dispersion curve to study the effect of dip on Rayleigh waves.

Chapter 6 discusses how material contrast of the anomaly affects Rayleigh wave propagation. In each case, the reflection from the side of the anomaly is presented in a negative dispersion curve. The study of depth of the anomaly is carried out by placing the anomaly between one-third of a wavelength to one wavelength below the surface. The synthetic seismogram and dispersion curves are analyzed and presented. The effect of shape of the anomaly on Rayleigh wave propagation is studied by changing the height and width of a rectangular anomaly, and changing the radius of a circular anomaly from one to one-third of a wavelength.

Chapter 7 discusses the application of inverse modeling using the new algorithm

based on a VFSR technique on the data set acquired from the Stellarton, Nova Scotia mine site. This is a model based inversion. The parameters of the synthetic model are updated with each iteration in order to match the reference data set. The fitness function, which is sum of the square of the difference of the model and reference dispersion curves is minimized by accepting good and bad solutions in a probabilistic manner.

Chapter 8 presents the final conclusions of this research. The pros and cons of the methodology, developed for near surface imaging is discussed in this chapter. Localized velocity analysis using panel methods works very well when subsurface contain dipping layers or anomalies. This method breaks when the minimum number of traces for computing Rayleigh waves dispersion curves is less than 10. VFSR, a random search method is used for numerical inversion of Rayleigh waves data from Stellarton coal field. This method can minimize a complex objective function or cost function. Improvement of the minimization algorithm which is developed for this research is required to handle more parameters and to obtain more accurate solution to the reference one.

Chapter 2

The Literature Review

2.1 Overview

Numerous literature sources were reviewed in order to develop a methodology for near surface imaging using Rayleigh wave. This review is presented in several stages which correspond to the steps needed to develop the methodology: numerical modeling of Rayleigh waves, methods to compute dispersion curves, sensitivity analysis of different parameters on Rayleigh wave propagation, finally, implementation of the VFSR technique to numerical invert Rayleigh waves data for near surface imaging of the Stellarton coal field.

This chapter will review and discuss literature which is relevant to each of these stages.

2.2 Finite Difference Technique

Elastic wave propagation problems of varying complexity and the numerical approaches to solve these problems have been addressed in many literature sources. Most of these methods are reviewed in (Alterman and Karal, 1968),(Alterman and Burridge, 1972), and (Boore, 1972). Finite difference is a popular numerical technique for solving wave equations because it is easy to implement and it handles simple geometry very well, such as rectangular shape. This method is classified into two categories: explicit and implicit. Both of these schemes replace the hyperbolic partial differential wave equation and boundary conditions by simple finite difference approximations in such a way that an explicit scheme determines the motion for a space location at an advanced time exclusively from the motion already determined for the previous times. Implicit schemes on the other hand, determine the motion at

all space locations simultaneously at an advanced time from known values at previous times through a matrix solution technique. Both explicit and implicit approaches are time marching procedures while solving the wave equation. Explicit schemes are simpler from the computational stand point when a few number of shot experiments are required and is implemented in this research.

2.3 2-D Finite Difference Modeling of Rayleigh Waves

The method of (Kelly et al., 1976) solved a second order hyperbolic elastic wave equation system using a 2-D finite difference technique in order to compute a synthetic seismograms of different models of exploration interest. In this paper, the authors described various implementational aspects of the finite difference approach such as grid dispersion, artificial reflection from the edge of the model, choice of spatial and temporal sampling, etc. In more detail, when a continuous medium is approximated by a discrete grid then calculated seismic responses or wave propagation on the discrete grid become dispersed with increasing travel time. This phenomenon is called grid dispersion. The effect of grid dispersion increases with larger grid spacing. As a rule of thumb, the number of grid points per wavelength should be greater than 10. The artificial reflection from the boundary edges of the model is a serious issue which is addressed in this paper. Different modes of elastic waves were identified from the synthetic seismogram computed from various geological models.

2-D finite difference staggered grid approach was used for solving a first order hyperbolic system with velocity and stress components (Virieux, 1986). A staggered grid stencil allows computation of different components of velocity and stress at different node points. The major difference between a staggered grid stencil from the usual stencils is that different components of the velocity field are not known at the same grid point.

The stability condition for the finite difference explicit scheme for n dimensional spaces is given by

$$V_p \frac{\triangle t}{\triangle x} = \frac{1}{\sqrt{n}} \tag{2.1}$$

where, V_p is P wave velocity, $\triangle t$ is sampling time, and $\triangle x$ is the grid spacing. This paper analyzed P and S wave numerical phase velocity dispersion curves. The

quantity γ which controls the numerical dispersion is given by:

$$\gamma = \sqrt{2} V_p \frac{\triangle t}{\triangle x} \tag{2.2}$$

and the quantity H is defined by: $H = \frac{\triangle x}{\lambda}$, controls number of grid points per wavelength, where λ represents the wavelength. P wave phase velocity dispersion curves do not depend on Poisson's ratio as shown in Figure 2.1. The value of the non-dimensional phase velocity of P waves is shown to be less than 1, and it approaches 1 when $H \approx 0.1$ for different angles θ of plane waves and for the dispersion parameter, $\gamma = 0.8$. Therefore it is recommended that grid point per wavelength should be at least 10. S wave phase velocity dispersion curves depend upon Poisson's ratio. For $\gamma = 0.8$, the value of the non-dimensional phase velocity of S wave is always less than 1 for different angles θ and for different Poisson's ratios, ν, as represented in Figure 2.2. The important observation made is that the behavior of a non-dimensional S wave plot does not degrade when ν tends to 0.5. Hence, it is suggested that this scheme can be used for models with a liquid solid interface.

In (Leparoux et al., 2000) demonstrated the effectiveness of Rayleigh waves for detecting and locating underground cavities, first through modeling, and then through two field experiments. The authors used a 2-D finite difference method to simulate wave propagation in an elastic media. The numerical model considered for this simulation introduced a cavity in the medium. From the analysis of simulated wavefront and corresponding shot gathers, it was observed that the lateral position of the cavity can be determined from the reflected wavefront in the shot gather. The amplitude plot in the dispersion curve of Rayleigh waves confirms that frequency of Rayleigh waves is affected by the cavity. Amplitudes of Rayleigh waves are locally attenuated for a specific frequency range according to the depth of the cavity.

A new idea in (Gelis et al., 2005) used a Perfectly Matched Layer (PML) boundary condition in the 2-D finite difference modeling of an elastic wave equation in order to avoid boundary reflections into the computational domain. This modeling package was used to study the interaction of Rayleigh waves with near surface heterogeneity. The effect of different cavity shapes, depths and altered zones is evaluated from the direct and diffracted seismograms and corresponding Rayleigh wave dispersion curves.

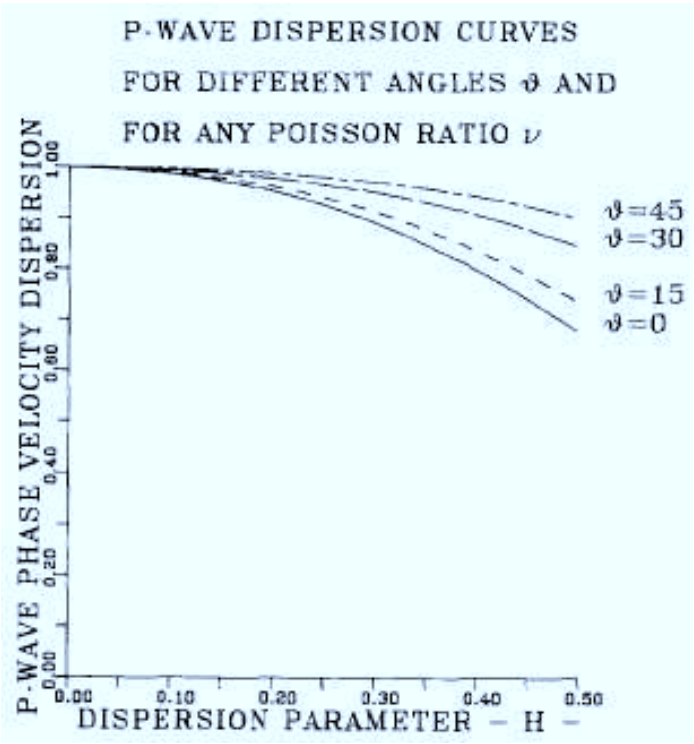

Figure 2.1: P wave dispersion curves (from Virieux 1986).

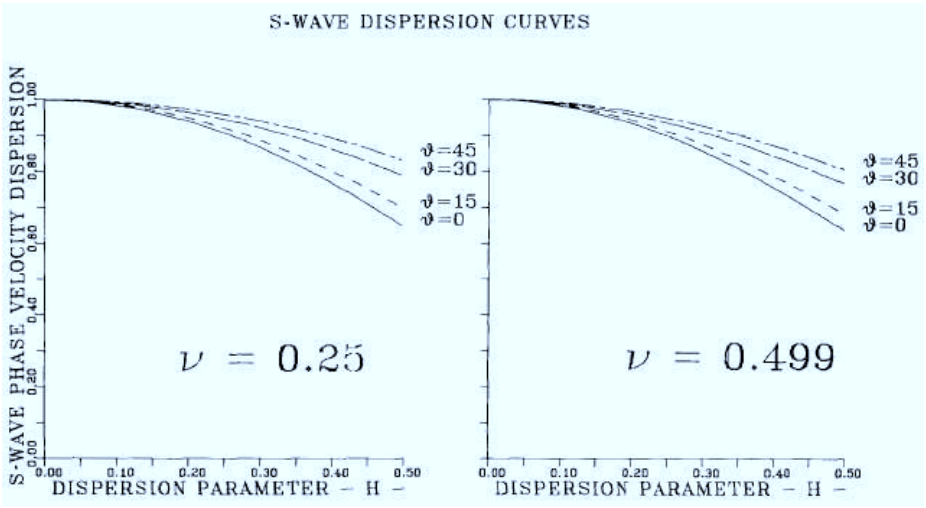

Figure 2.2: S wave dispersion curves (from Virieux 1986).

A complex, non-symmetrical diffraction pattern was observed in a differential seismogram which was computed by taking the difference of seismograms for models both with and without a cavity. The dispersion curve corresponding to the differential seismogram shows well-localized scattering from heterogeneity. Missing coherent energy appears in specific frequency bands related to the cavity depth, shape, and material properties of the surrounding medium. The results of Figure 2.3 indicate that the deeper the cavity, the later the diffracted wave comes from the cavity in time. Differential seismograms shows the interaction between diffracted and converted waves in very complex manner. Some of the wave trains are highly disturbed which are represented by label 3. This complex phenomenon is confirmed by differential images as well. The lower amplitudes on the dispersion curves of the shot gather indicate that a wave of that particular frequency band is not propagating with regular phase velocity in the forward direction. The seismogram indicates that shallow cavities have more impact on wave propagation. Moreover, rectangular cavity generates more severe perturbations than a circular cavity, as shown in the right column of Figure 2.3. In general, man made cavities are easier to detect than karst geology. Due to the sharp edges of a rectangular cavity, the diffracted waves become stronger. The influence of altered medium around the cavity shows very complex phenomena of wave propagation in the seismogram, in Figure 2.4. The differential seismogram shown in Figure 2.3 highlights the ringing due to the trapped waves in a low velocity zone as shown in Figure 2.4.

2.4 MASW and Methods to Compute Dispersion Curves

In (Park et al., 1999) discussed the effectiveness of MASW method for detecting near surface anomalies which are of geotechnical interest. In most of the surface seismic surveys, more than 80% of the total energy generated by a compressional source is imparted into Rayleigh waves. Therefore, they are very high in amplitude. Due to the change of elastic properties with depth in a medium, different frequency components of Rayleigh waves propagate with different phase velocities. The frequency-dependence or dispersive properties of Rayleigh waves are key to utilizing these waves for near surface imaging purposes. One of the most common uses of the dispersive properties

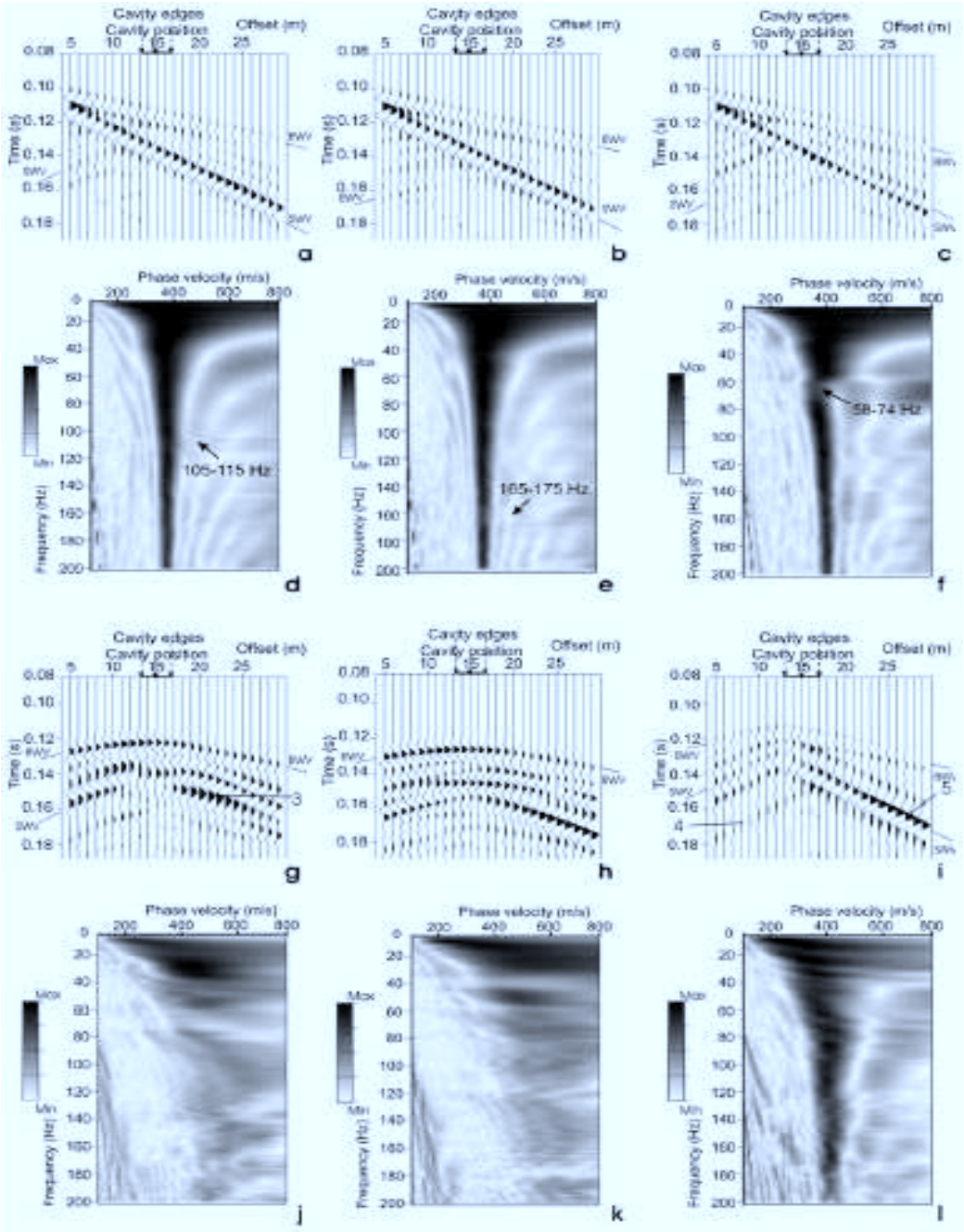

Figure 2.3: Seismograms (a,b,c), corresponding dispersion images (d,e,f), differential seismograms (g,h,i) and the corresponding dispersion images (j,k,l) for the homogeneous medium with 5 meter deep circular cavity(a,d,g,j), an 8 meter deep circular cavity (b,e,h,k) and 2 meter deep rectangular cavity (c,f,i,l). Label 3 for disturbed arrival train, label 4 for diffracted body wave, and label 5 for diffracted surface waves (from Gelis et al. 2005).

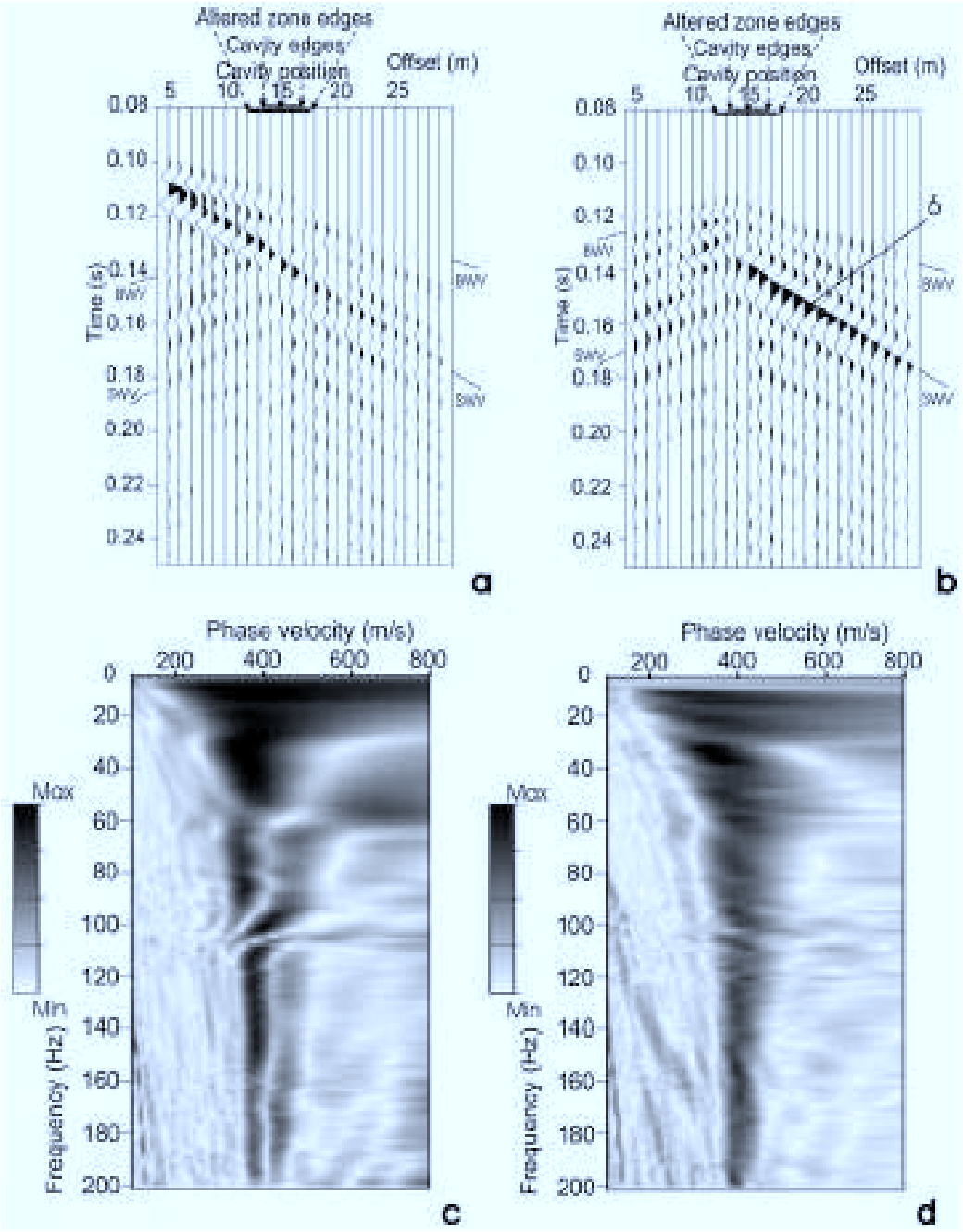

Figure 2.4: Seismogram (a), corresponding dispersion image (c), differential seismogram (b), and corresponding dispersion image (d) for a homogeneous medium with a 2 meter deep circular cavity and surrounding circular zone of altered media. Label 6 for forward diffracted surface waves. Labels BWV and SWV are respectively P wave and Rayleigh wave (from Gelis et al. 2005).

of Rayleigh waves is to obtain a S wave velocity with depth or stiffness profile through the analysis of the plane fundamental mode of Rayleigh waves. This analysis evaluates the near surface stiffness variation with depth. The authors described the importance of the accurate computation of the Rayleigh waves dispersion curve, i.e. phase velocity versus frequency, in order to obtain a reliable subsurface image though the inversion of the dispersion curve. MASW requires the plane fundamental mode of Rayleigh waves as the main component of analysis. However, a variety of waves types, such as body waves, non-planar Rayleigh waves, higher mode Rayleigh waves, back-scattered waves, ambient noise, etc., are also generated during the creation of plane fundamental mode of the Rayleigh waves. Decomposition of multichannel data in to a swept-frequency format permits the identification of noise based on frequency content and offset. Hence, a high signal to noise ratio can be achieved during acquisition of Rayleigh wave's data. A simple multichannel coherency measurement can be used to compute the phase velocity at frequency from frequency sweep data. In this paper multichannel data of Rayleigh waves are decomposed into a time-variable frequency format, or swept frequency record, where each frequency component is displayed in a unique and continuous format. The coherent noise which may contaminate the fundamental mode of Rayleigh waves can then be examined and isolated during data acquisition and processing. Linear separation of each Rayleigh wave frequency component allows calculation of phase velocity by simply measuring the linear slope of each frequency component. The accuracy of the Rayleigh wave's dispersion curves determined using this method is proven through field comparisons of inverted S wave velocity profiles with down-hole S wave profiles.

2.5 Near Offset Geometry

In spite of the dominance of Rayleigh waves on seismic data, optimal recording of Rayleigh waves requires proper field configurations. In order to record the plane fundamental mode of Rayleigh waves, the recommended distance x_1 (Richart et al., 1970) of the nearest receiver from the source to avoid a near offset effect should be greater than half of the maximum desired wavelength (λ_{max}) (Stokoe et al., 1994).

$$x_1 = 0.5\lambda_{max}$$

2.6 Far Offset Geometry

High frequency Rayleigh waves attenuate quite rapidly with distance away from the source (Bullen, 1963). Therefore, high frequency Rayleigh waves will not dominate the high frequency component of the spectrum if the maximum receiver distance is far away from the source. Contamination by body waves because of attenuation of high-frequency Rayleigh waves at longer offset is known as the far offset effect. In order to minimize the far offset effect, offset from the source needs to be reduced. Figure 2.5 represents the quality of field vibroseis records with near field and far field effects. These effects can be reduced in the swept shot record through a optimum field configuration and high signal to noise ratio can achieved. The frequency swept data obtained after noise analysis allows computation of an accurate dispersion curve.

In (Xia et al., 2007) an algorithm was presented for calculating an image of dispersive energy in the frequency-velocity domain. Impulsive data in the offset-time domain is first converted into frequency sweep data. This step converts time to frequency. The slant stack technique is then used on the frequency swept data to complete the transformation from offset to velocity. This simple two step algorithm generates an image of a Rayleigh waves dispersion curve in the frequency-velocity domain. Mathematically, each trace of multichannel impulsive data $x\left(d,t\right)$ in the offset-time domain is convolved with a linear sweep source $S(t)$. This transforms $x\left(d,t\right)$ into frequency-sweep data $X\left(d,t\right)$ by the equation given below:

$$X(d,t) = S(t) * x(d,t), \tag{2.3}$$

The linear sweep source is represented by,

$$S(t) = \sin\left(2\pi f_1 t + \frac{\pi\left(f_2 - f_1\right)}{T} t^2\right), \tag{2.4}$$

where f_1, f_2 and T are lowest, highest frequencies and length of $S(t)$ respectively. Next, Linear Move Out (LMO) correction is applied to $X\left(d,t\right)$ through a coordinate

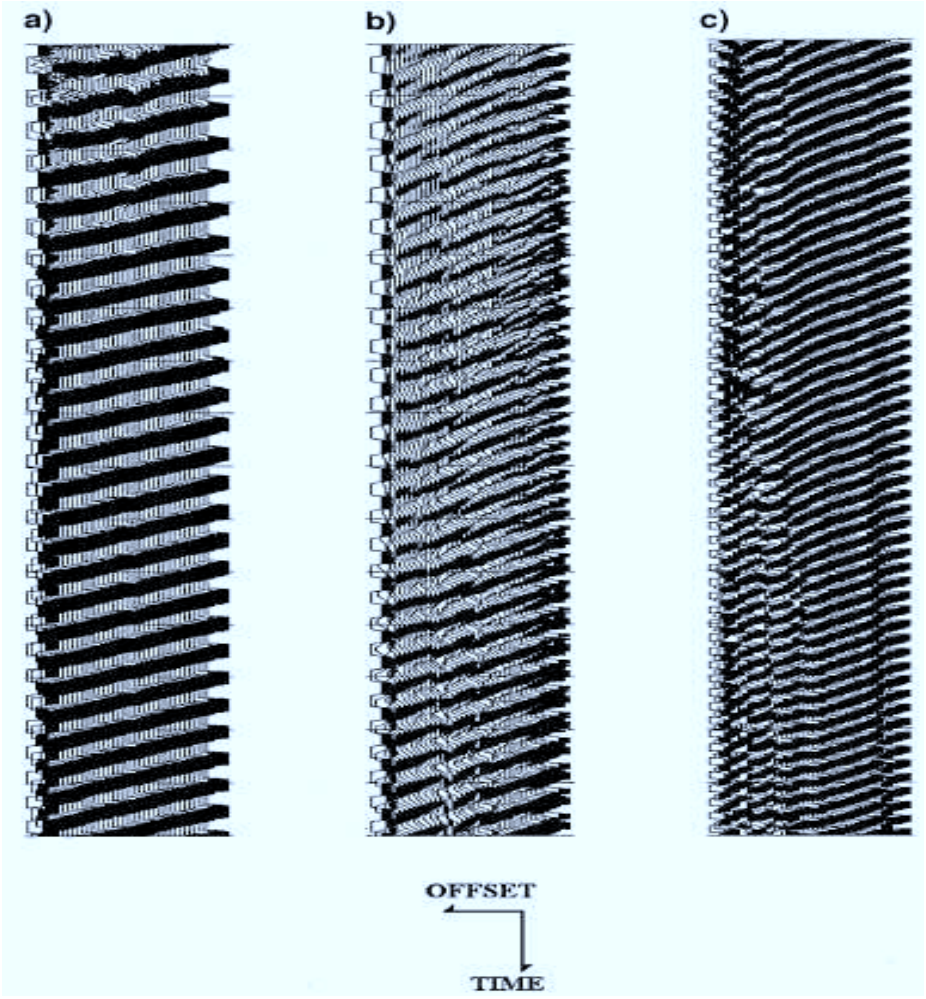

Figure 2.5: Field data example of different qualities in recorded Rayleigh waves obtained using Vibroseis, (a) indicating good quality, (b) near field effect that is identified by either weak energy or reduced coherency with fragmented energy packets, and (c) far-offset effect that is identified by decreased slopes or reduced coherency. The distance of the nearest receiver from the source is (a) 27 m, (b) 1.8 m and (c) 89 m (from Park et al. 1999).

transformation,

$$\tau = t - d/v. \tag{2.5}$$

After LMO correction, and the direct arrival with slope $1/v$ on $X(d,t)$ becomes flat, then data are summed over the offset to obtain,

$$X(v,\tau) = \sum X(d, \tau + d/v). \tag{2.6}$$

Repeating the LMO correction for values $v \in (v_{min}, v_{max})$ and stacking the data, an image in time-velocity domain. After transforming time to frequency using their linear relationship, the dispersion curves of Rayleigh waves $X(d,t)$ can be obtained.

2.7 A Synthetic Example

The method of generating a dispersive image of Rayleigh waves data by frequency decomposition and slant stacking is verified with an example of synthetic data. A 20 seconds long linear up sweep data from 2 Hz to 50 Hz was used to perform frequency decomposition of multichannel synthetic data with a 10 Hz dominant frequency. Figure 2.6 shows the first 8 seconds of frequency sweep data. A dispersive image is obtained after slant stacking of frequency sweep data through a velocity range from 100 m/sec to 700 m/sec at an increment of 5 m/sec. This is represented in Figure 2.7. Higher mode of Rayleigh waves are seen in the dispersion curve between 25 to 40 Hz along with the fundamental mode.

A new technique by (Moghaddam, 2006) proposed a method called Attenuation Analysis of Rayleigh Waves (AARW) to determine the location of voids and to estimate its embedment depth. This technique is based on the observed damping effect of the void on the surface responses. Moghaddam first simulated MASW test by constructing two and three dimensional numerical models and investigated the effect of lateral inhomogeneities on the propagation of Rayleigh waves by introducing voids with different sizes and at different depths. Combined effect of voids and layered systems are also studied. Finally, experimental field and laboratory data are presented and trends are compared with numerical results.

Figure 2.8 (a and b) show contour plots of the horizontal and vertical normalized

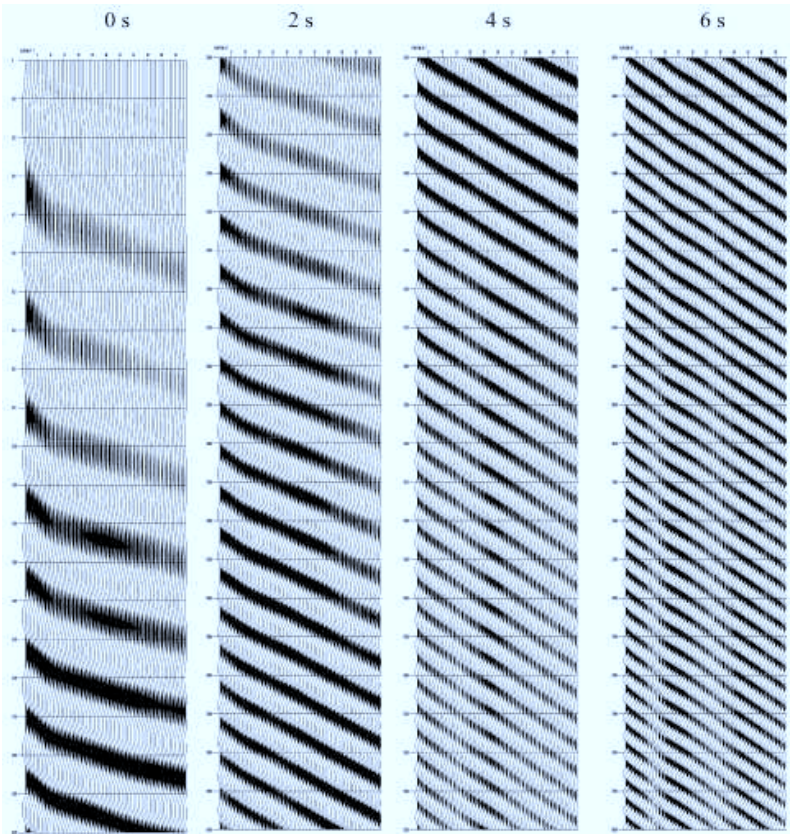

Figure 2.6: The first 8 seconds of frequency swept data shown in four panels with the starting time of each panel given at the top (from Xia et al. 2007).

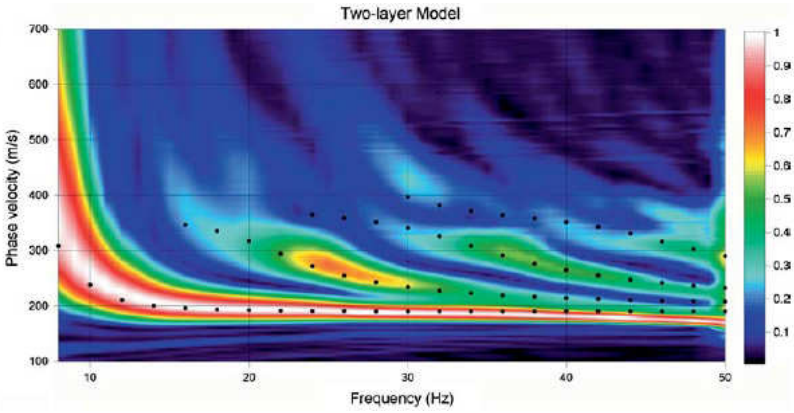

Figure 2.7: Dispersion curve generated by slant stacking of frequency swept data (from Xia et al. 2007).

surface responses in presence of a void. Dashed lines represent the projection of the void boundaries to the surface. Event A is the incident Rayleigh wave and it is reflected back after the interaction with the near boundary of the void. Reflected Rayleigh wave is represented by event D1. Most part of reflected energy is in the form of Rayleigh wave and the rest is in the form of P wave, event G1. Event B represents part of the incident energy that is transmitted into the void region. This energy splits into three parts. One part travels with velocity of P wave, another part travels with the velocity of Rayleigh waves and the remaining energy travels with low velocity. When event B hits the far boundary of the void, the P wave part passes without the interaction with the void. Transmitted part of Rayleigh wave energy, event C interacts with the void and part of its energy transformed into P wave, event G2, and part of its energy reflected back from the far boundary of the void. The slower part of event B is trapped in between the void boundaries and is represented by event E and its energy decreases after each interaction with the void boundaries. The trapped energy bounces back and forth until it attenuates completely. Figure 2.9 shows normalized Rayleigh wave group velocity which is measured at the surface. A drop of group velocity is observed over the void i.e. in between the dashed line. Even though, group velocity increases after the void, but is not regained its original value.

The frequency content of the recorded surface responses are shown in Figure 2.10. All frequency amplitudes of traces recorded at different locations along the surface are shown in plot 'a' and 'b'. The amplitude spectrum of traces in a homogeneous media as shown in plot 'a', are smooth and their shape does not change with distance from the source. The amplitude of the traces in plot 'a' decreases with the increase of distance from the source and peak energy occurs at a frequency of about 100 Hz. If this is compared with the frequency content of the source it can be concluded that the medium filters some of the low frequencies. Amplitude spectrum of traces in plot 'b' are distorted in presence of a void. Different shape of frequency spectrum indicate that the medium is dispersive. Contour plots of these data are shown in 'c' and 'd'. Presence of void cause ripples in plot 'd' before the void. The distance between consecutive ripples is a function of time delay between the main signal and its reflection i.e. larger the delay time closer will be the ripples to each other. Hence,

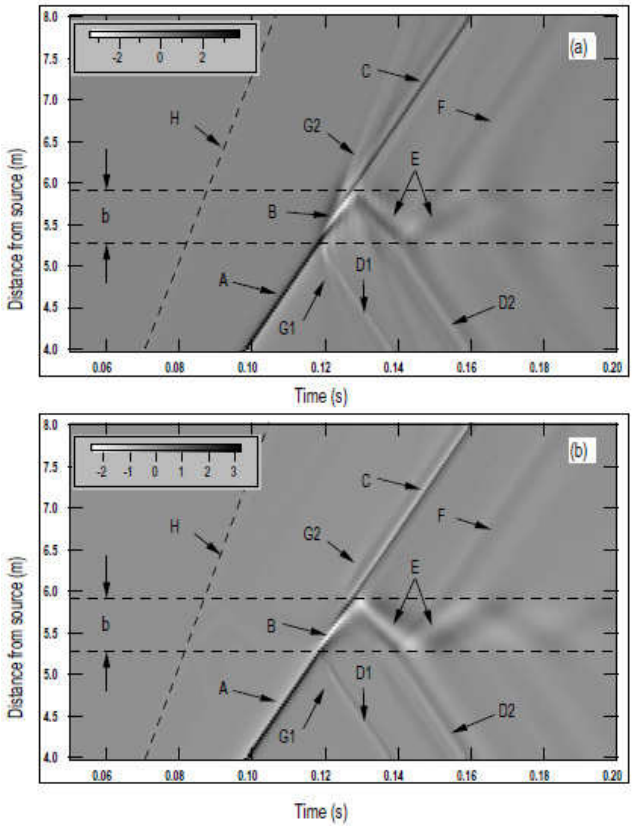

Figure 2.8: Time responses along the surface in presence of a void. (a) Horizontal responses, (b) vertical responses (from Moghaddam 2006).

ripples in plot 'd' means, different frequencies are reflected back from the void with different time delays. Two energy concentrations are observed over the void region. Later one is related to depth of the void however former value could not be associated with any meaningful parameter. Moghaddam observed that effect of trapped energy is present as a region in the vicinity of voids in the frequency domain. The extent of this region depends on the void size and the frequency contents of the incident energy. Hence, in some cases it is possible to map the size of a void to the extent of the region with energy concentration.

2.8 Sensitivity Analysis of Rayleigh Waves

In a parametric study conducted by (Bodet et al., 2004) on the influence of dipping layers on Rayleigh wave propagation in order to investigate the reliability of a flat

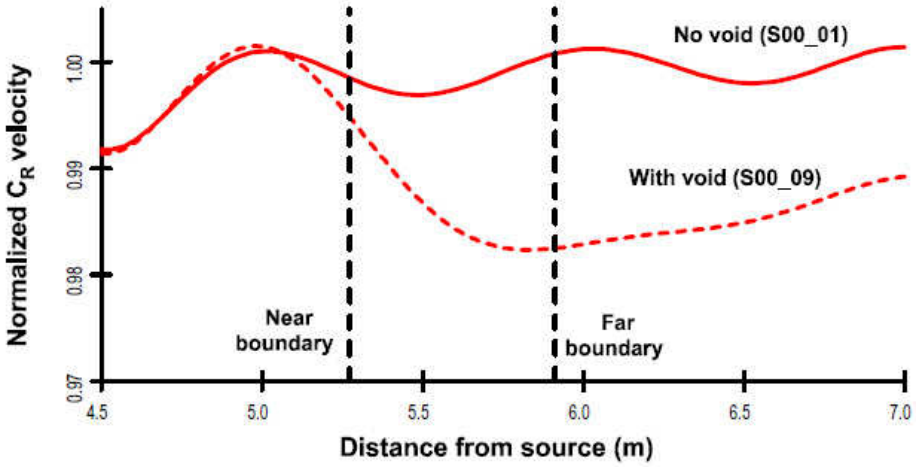

Figure 2.9: Group velocity measured at the surface (from Moghaddam 2006).

layer assumption inherent to the inverse problem. In this parametric study, a flat layered model was considered as a reference model. The material properties, layer thickness and the frequency band of the source of this model were chosen in such a way so that the main Rayleigh wave's wavelength were suitable to perform the parametric study on the first interface. A reference dispersion curve was then computed from the synthetic data using a wavefield transform technique. In Figure 2.11 the reference model for this parametric study is shown at the top and the corresponding shot gather is shown at the bottom. The reference dispersion curve is shown in Figure 2.12 with error bar.

2.9 Parametric Study on the Interface Slope

The slope interface was modified using a range of slopes which were determined on the basis of recording points versus Rayleigh waves penetration depth. The interface below the source location has been set to the reference model's first layer thickness. Some selected slopes are given in Table 2.1. The global dispersion curves computed for the slopes given in Table 2.1 are represented in Figure 2.13. It was observed that the dispersion curves are shifted upward and downward in a significant manner even for slight slopes. This shift increases with the slope but depends on its direction. The dispersion curves calculated over down slope are less shifted than those calculated over

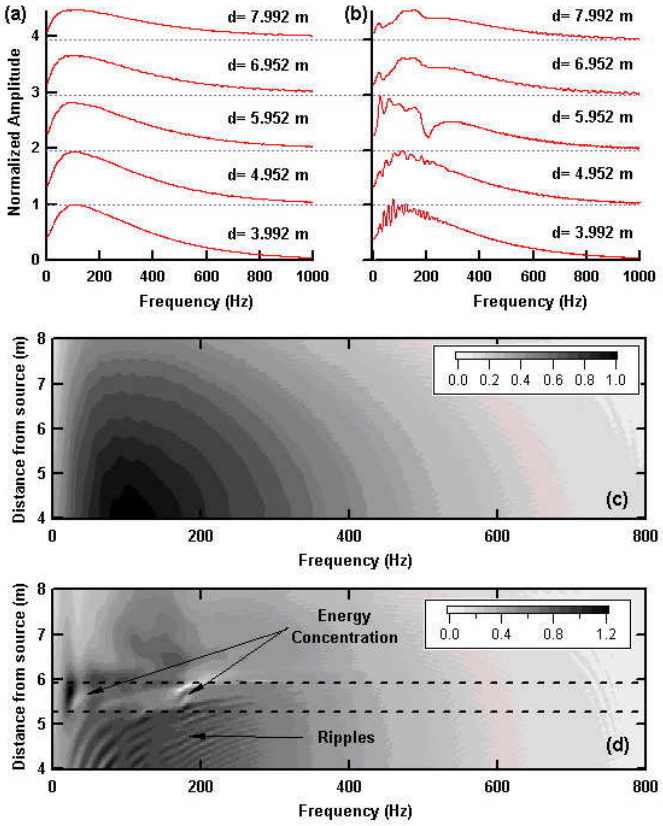

Figure 2.10: Frequency spectra at the surface of the medium. Study in homogeneous medium represented by (a) and (c). Study of a medium in presence of a void is represented by (b) and (d) (from Moghaddam 2006).

up slopes. This is related the penetration depth of Rayleigh waves. The maximum penetration depth of Rayleigh waves is assumed to be one-third of a main Rayleigh waves wavelength. As the slope increases, Rayleigh waves generated over a down slopes are traveling with the velocity of the first layer. On the other hand, Rayleigh waves generated over an up slope are traveling with combined velocity of both layers and this causes a shifting of the dispersion curve to the second layer velocity. Another important thing to notice is that the shape of the dispersion curves for the up slopes are modified as the slope increases. The authors concluded that the influence of a layer's dip cannot be summed up to a typical first layer thickness variation influence.

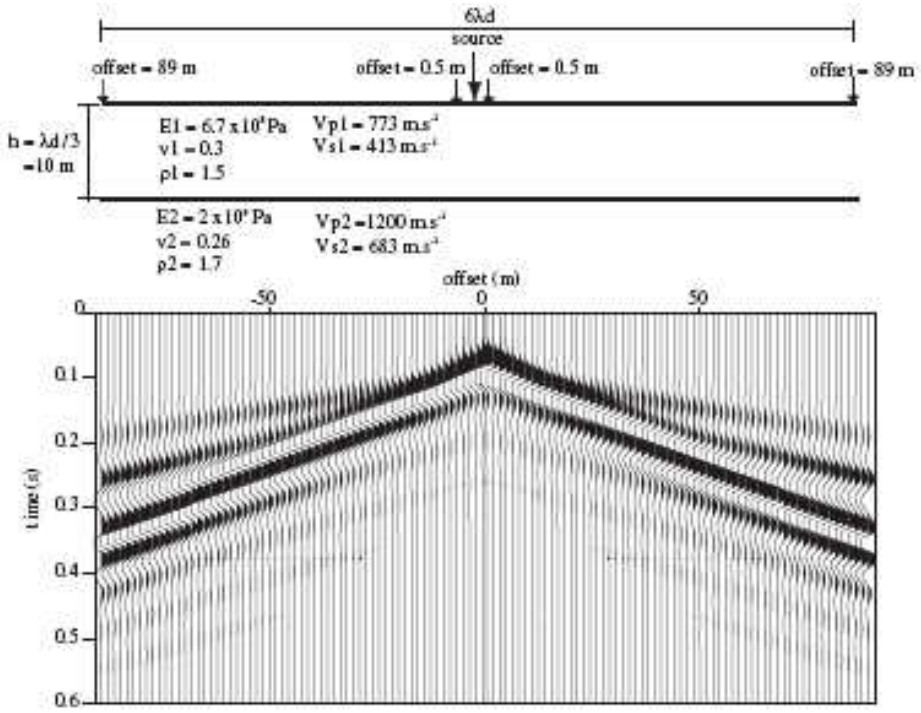

Figure 2.11: Reference of finite element horizontally layered model. Ei, νi and ρi are respectively the Young modulus, Poisson's ratio and density of the layer i. Vpi, and Vsi are corresponding P and S wave velocities. Synthetic seismogram is shown at the bottom (from Bodet et al. 2004).

2.10 Rayleigh Wave Inversion

A method of search is needed for a suitable parameter description of an earth model. The Rayleigh wave data are known but the layer thickness and the velocity parameters are unknown. This is an inverse problem. A method is needed to find parameters for the modeling process to generate data that best fit the reference data. The following literature describes search methods to solve inverse problem. Gradient descent method works for a convex function with a single global minimum. The random search method can solve problem with many local minimums.

2.10.1 Gradient Descent Method

Gradient decent or method of steepest descent is a first order optimization algorithm to find a local minimum of a function. In this optimization method the steps needed

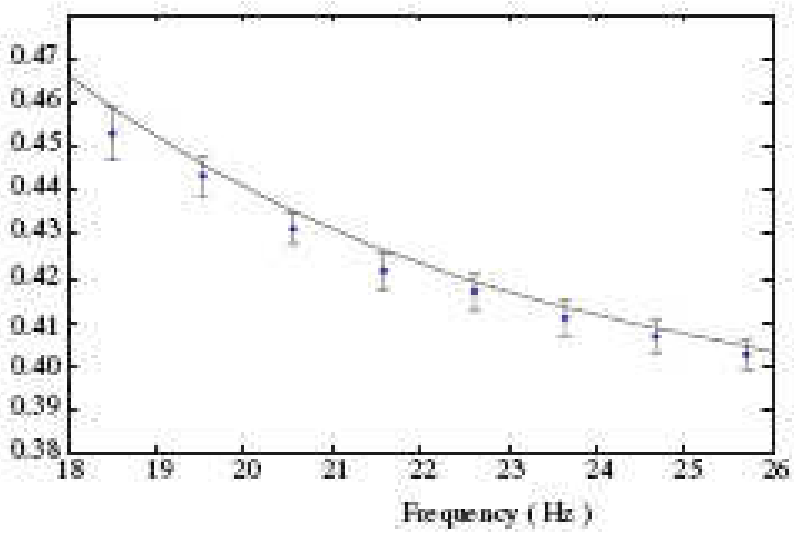

Figure 2.12: The reference dispersion curve with error bar (from Bodet et al. 2004).

		thickness(m)	
slope (o)	hu ($x = -89m$)	h ($x = 0m$)	hd ($x = 89m$)
0	10	10	10
0.87	8.6	10	11.4
1.73	7.3	10	12.7
1.79	7.2	10	12.8
1.85	6.9	10	13.1
2.2	6.5	10	13.5
2.49	6.1	10	13.9
2.86	5.5	10	14.5
3	5.3	10	14.7

Table 2.1: Some selected points of the parametric study on the interface slope. The thickness h is at the base of the source, hu is the thickness at the base of the leftmost offset, and hd is the thickness at the base of the rightmost offset (from Bodet et al. 2004).

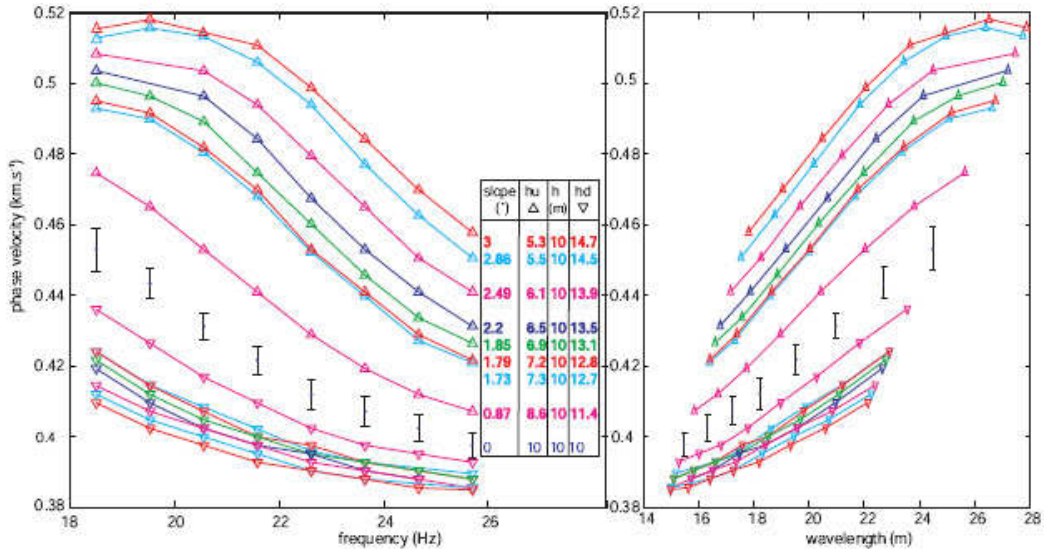

Figure 2.13: Dispersion curves for the slopes listed in Table 2.1. Downward triangles refer to the down slope (hd), upward triangles refer to the up slope (hu). The blue dots correspond to the reference model (from Bodet et al. 2004).

to be taken which are proportional to the negative of the gradient of the function at the current point. The outline of this method is as follows.

If the real valued function $f(\mathbf{X})$ is defined and differentiable in a neighborhood of a point $\mathbf{P}_0$ then the negative gradient of f at $\mathbf{P}_0$ i.e. $-\nabla f(\mathbf{P}_0)$ points locally in the direction of greatest rate of decreases. Hence, by starting at the point $\mathbf{P}_0$ and search along the line through $\mathbf{P}_0$ in the direction $\mathbf{S}_0 = -\nabla f(\mathbf{P}_0) / \| -\nabla f(\mathbf{P}_0) \|$ will arrive at a point $\mathbf{P}_1$, where a local minimum occur i.e. $\mathbf{P}_1 = \mathbf{P}_0 + \gamma \mathbf{S}_0$, for $\gamma > 0$ a small number so that $\mathbf{P}_0 > \mathbf{P}_1$. Next to compute $-\nabla f(P_0)$ and search along the line through $\mathbf{S}_1 = -\nabla f(\mathbf{P}_1) / \| -\nabla f(\mathbf{P}_1) \|$ and arrive at the point $\mathbf{P}_2$, where a local minimum occurs i.e. $\mathbf{P}_2 = \mathbf{P}_1 + \gamma \mathbf{S}_1$, for $\gamma > 0$ a small number so that $\mathbf{P}_1 > \mathbf{P}_2$. Iteration continues and will produces a sequence of points, $\{\mathbf{P}_k\}_{k=0}^{\infty}$ with the property of $\mathbf{P}_0 > \mathbf{P}_1 > ... > \mathbf{P}_k ....$ the $\mathbf{P}$ will be a local minimum of $f(\mathbf{X})$. Figure 2.14 illustrate the gradient descent optimization. The minimization function f shown in the Figure 2.14 has a bowl shape. The blue curves are the contour lines where the function f has constant value. The starting guess point of the minimization process is shown by a red arrow in the direction of the negative gradient at that point. It is observed that gradient descent ends up to the global minimum of the function

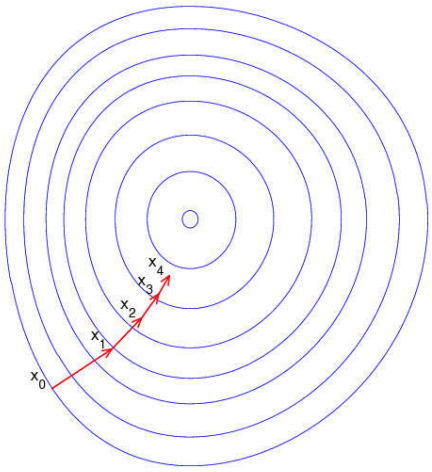

Figure 2.14: Gradient descent optimization (from wikipedia).

f. If the minimization problem is convex it is observed that gradient descent ends up to the global minimum of the function. However for objective function which has multiple local minimum the gradient method will fail unless the starting point is in the region of a global minimum and there is no guarantee of the starting point is in the right place.

2.10.2 Random Search Methods

A simple Monte Carlo simulation randomly selects a point somewhere in the search space and by repeating this process by many many times all these points are used to find out information about the search space. This method can be used to solve some specific problems, e.g. finding the area of certain region, an example of a numerical integration technique. A modification to the simple Monte Carlo simulation was made with a new sampling procedure which incorporates the temperature of the system. The modified version is known as the Metropolis Monte Carlo simulation. In this method, a new point in the search space is sampled by making a small random change to the current point. If the current solution is less than the old solution, then the current solution is accepted. If the current solution is greater than the old solution, then it will either be probabilistically accepted or probabilistically rejected, depending on whether the difference between the current and previous solution is

small or large enough (Metropolis et al., 1953). The Metropolis Monte Carlo simulation was modified in order have better control in sampling the search space. This was done using a slow cooling schedule, which is known as annealing, and the method is known as simulated annealing (Kirkpatrick et al., 1983). A simulated annealing optimization starts with a Metropolis Monte Carlo simulation at high temperature. A large number of random steps at high temperature will be accepted and after sufficient number of iterations, the temperature is decreased which results in a decreased search space. A computer program which replicates simulated annealing consists of a set of nested Do loops. The outer loop sets the temperature and the inner loop runs the Metropolis Monte Carlo simulation at that temperature. The method by which the temperature is decreased is known as the cooling schedule. The simulated annealing algorithm was found to have limitations in solving inverse problems with an N dimensional model space. Each model parameter in N dimensional space has a different finite range of variation and each parameter has a different effect on the fitness function, therefore it was realized that each parameter was allowed to have different degree of perturbation from their current position. The use of different temperatures corresponding to each model parameter with a low cooling schedule leads to a very fast simulated annealing technique (Ingber, 1989) and (Ingber, 1993). Further modification to very fast simulated annealing was carried out by occasionally changing the cooling schedule for the model parameters based on how the parameter affected the fitness function (Ingber, 1989). The modified version is known as very fast simulated re-annealing.

$$LB_i \leq X_i^k \leq UB_i, \tag{2.7}$$

where LB_i and UB_i are the lower and upper bounds of the model parameter X_i. The updated model parameter at $k+1$ is represented by the following relation

$$X_i^{k+1} = X_i^k + Y_i \left(UB_i - LB_i\right), \tag{2.8}$$

such that $Y_i \in [-1, 1]$ and

$$LB_i \leq X_i^{k+1} \leq UB_i, \tag{2.9}$$

where Y_i is expressed as

$$Y_i = sgn\left(U_i - \frac{1}{2}\right) T_i \left[\left(1 + \frac{1}{T_i}\right)^{|2U_i - 1|} - 1\right], \tag{2.10}$$

where, U_i is a random number from a uniform distribution. The cooling schedule to obtain a global minimum is

$$T_i\left(k\right) = T_{0i} exp\left(-c_i k^{\frac{1}{q}}\right), \tag{2.11}$$

where T_{0i} is the initial temperature for the model parameter i. It is claimed that when the value of q is equal to the number of parameters, then the convergence will be achieved (Ingber, 1989). But if the number of parameters is very large, then this will slow down the speed of convergence. The parameter c_i is used to control temperature (Ingber, 1989). The sensitivity S_i for each parameter is computed for re-annealing by

$$S_i = \frac{\partial F\left(\mathbf{X}\right)}{\partial X_i}, \tag{2.12}$$

The temperature T_{ik} of each model parameter i at iteration k is modified by

$$T_{ik'} = T_{ik}\left(\frac{S_{max}}{S_i}\right), \tag{2.13}$$

where S_{max} is the largest value of S_i. This will allow an increased search space of relatively insensitive parameters by increasing the temperature. The acceptance criteria of the very fast simulated reannealing algorithm is similar to that used in Metropolis simulated annealing.

Chapter 3

Background Theory

3.1 Overview

Seismic waves can be used as a tool to image a subsurface. The theory of elasticity helps us to understand the phenomenon of seismic wave propagation, interpret the seismic data, analysis, and implement new survey designs, etc. This research uses Rayleigh waves to image near surface anomalies, therefore it is important to review the theory of Rayleigh wave propagation and the physical properties of the medium that can be obtained when a Rayleigh wave is propagated in the medium. This chapter reviews the theory of elasticity in order to understand the propagation of Rayleigh waves in a linearly elastic isotropic medium. The contents of this chapter is based on the work presented in (Aki and Richards, 1980), (Ikelle and Amundsen, 2005), (Sheriff and Geldart, 1998) and (Yilmaz, 1987).

3.2 Theory of Elasticity

Elastic waves are associated with three main physical properties: first, a seismic source which can be regarded as an external force to the medium; second, a deformation caused by the source, which can be measured as displacement or strain; and third, the internal forces or stress which restore the medium to equilibrium. The material parameters used in elastic wave propagation are discussed below.

3.2.1 Stress

Force per unit area is called stress. If a force is perpendicular to an area, then the stress is said to be normal stress and if it is tangential to an area, then the stress is said to be shearing stress. If a force is neither parallel nor perpendicular to the area, the stress can be resolved into normal and shear stress components. The stresses are

related to a point in the propagation of elastic waves. Therefore, if we describe a particle as a volume element, the stresses acting on six faces of a cube can be resolved into nine components of stress. For example, the stress components acting on the area element facing the +x direction is represented by:

$$\mathbf{S_x} = \begin{pmatrix} \sigma_{xx} \\ \sigma_{yx} \\ \sigma_{zx} \end{pmatrix}$$

In these components, the second subscript, x, indicates that the surface is perpendicular to the x-axis. Similarly, the stress components acting on the areas facing the +y and +z directions are:

$$\mathbf{S_y} = \begin{pmatrix} \sigma_{xy} \\ \sigma_{yy} \\ \sigma_{zy} \end{pmatrix} \text{, and } \mathbf{S_z} = \begin{pmatrix} \sigma_{xz} \\ \sigma_{yz} \\ \sigma_{zz} \end{pmatrix}$$

All of these nine components of stress are represented by a stress tensor as :

$$\sigma_{ij} = \begin{pmatrix} \sigma_{xx} & \sigma_{xy} & \sigma_{xz} \\ \sigma_{yx} & \sigma_{yy} & \sigma_{yz} \\ \sigma_{zx} & \sigma_{zy} & \sigma_{zz} \end{pmatrix}$$

where $i, j = x, y, z$. In a state of equilibrium, stresses acting on opposite faces balance their corresponding stresses.

3.2.2 Strain

The measure of deformability of materials is described as strain. This is an important characteristic of wave propagation. Strains can also be described as a set of relative displacements. There are three basic types of strain: change in length per unit length, or longitudinal strain, change in volume per unit volume, or volumetric strain, and change in shear per unit length, or shear strain.

The three components of longitudinal strain in the directions of the x, y, and z

coordinate axes are respectively represented by:

$$\varepsilon_{xx} = \frac{\partial u}{\partial x}$$
$$\varepsilon_{yy} = \frac{\partial v}{\partial y}$$
$$\varepsilon_{zz} = \frac{\partial w}{\partial z}$$

where, the quantities $\frac{\partial u}{\partial x}$, $\frac{\partial v}{\partial y}$ and $\frac{\partial w}{\partial z}$ are the relative increase in length in the directions of the x, y and z coordinate axes respectively.

The longitudinal strains result in the change in dimensions, which is the change in volume when the body is stressed. The change in volume per unit volume is called dilation and is represented by volume strain as :

$$\triangle = \varepsilon_{xx} + \varepsilon_{yy} + \varepsilon_{zz}$$

The amount of change angle in the xy, yz, and zx planes is represented by shear strain. The shear strains in the xy, yz, and zx planes are:

$$\varepsilon_{xy} = \varepsilon_{yx} = \frac{\partial v}{\partial x} + \frac{\partial u}{\partial y}$$
$$\varepsilon_{yz} = \varepsilon_{zy} = \frac{\partial w}{\partial y} + \frac{\partial v}{\partial z}$$
$$\varepsilon_{zx} = \varepsilon_{xz} = \frac{\partial u}{\partial z} + \frac{\partial w}{\partial x}$$

where the quantities $\frac{\partial v}{\partial x} + \frac{\partial u}{\partial y}$, $\frac{\partial w}{\partial y} + \frac{\partial v}{\partial z}$ and $\frac{\partial u}{\partial z} + \frac{\partial w}{\partial x}$ are the amount by which the right angles of xy, yz, and zx planes are reduced. A deformation can be described as a strain tensor made up of nine components, similar to the stress tensor. Hence,

$$\varepsilon_{ij} = \begin{pmatrix} \varepsilon_{xx} & \varepsilon_{xy} & \varepsilon_{xz} \\ \varepsilon_{yx} & \varepsilon_{yy} & \varepsilon_{yz} \\ \varepsilon_{zx} & \varepsilon_{zy} & \varepsilon_{zz} \end{pmatrix}$$

where $i, j = x, y, z$. Strain tensors are symmetric. i.e. $\varepsilon_{ij} = \varepsilon_{ji}$; i,j=x,y,z. In water and other nonviscous fluids, only changes in volume are possible; therefore shear strains are zero for nonviscous fluids.

3.2.3 Hooke's Law

Hooke's Law states that for small deformation, a strain in a deformed body is linearly proportional to the stress applied. The relationship between stress and strain can be expressed in matrix form where stress and strain are 1×6 matrices and Hooke's Law of proportionality is a 6×6 matrix whose elements are elastic constants or stiffness components. For an isotropic medium, the relationship between stress σ_{ij} and strain ε_{ij} , $i, j = x, y, z$ can be expressed as

$$\begin{aligned} \sigma_{xx} &= \lambda\triangle + 2\mu\varepsilon_{xx} \\ \sigma_{yy} &= \lambda\triangle + 2\mu\varepsilon_{yy} \\ \sigma_{zz} &= \lambda\triangle + 2\mu\varepsilon_{zz} \\ \sigma_{yz} &= \mu\varepsilon_{yz} \\ \sigma_{zx} &= \mu\varepsilon_{zx} \\ \sigma_{xy} &= \mu\varepsilon_{xy} \end{aligned} \tag{3.1}$$

where $\triangle = \varepsilon_{xx} + \varepsilon_{yy} + \varepsilon_{zz}$. These equations are often expressed as a matrix equation:

$$\sigma = \mathbf{C}\varepsilon \tag{3.2}$$

where σ, ε, and $\mathbf{C}$ are respectively stress, strain, and stiffness matrices.

3.2.4 Physical Interpretation of Elastic Constant for an Isotropic Medium

The quantities μ and λ are the components of stiffness in matrix C. They are called *Lamé* parameters. Since, $\varepsilon_{ij} = \frac{\sigma ij}{\mu}$, it evident that ε_{ij} is small for a larger μ. Therefore, the constant μ is a measure of resistance to shear. It is positive and has a unit of stress. For water and other non-viscous fluids, $\mu = 0$. The second constant, λ, has no simple physical meaning but it simplifies Hooke's law to a great extent. There are three other important elastic constants which can be expressed in terms of *Lamé* parameters. There are Young's modulus (E), Poisson's ratio (ν) and bulk modulus (K). These parameters are often used to characterize physical properties of rocks. In order to define E and ν, we consider a medium where all stresses are zero except σ_{xx}. Assume that σ_{xx} is normal stress. Then the dimension parallel to σ_{xx} will increase.

Therefore, ε_{xx} is positive due to elongation in the x direction. The dimension normal to σ_{xx} will decrease and ε_{yy} and ε_{zz} are negative. Hence, 3.2 gives

$$\begin{aligned} \sigma_{xx} &= (\lambda + 2\mu)\,\varepsilon_{xx} + \lambda\,(\varepsilon_{yy} + \varepsilon_{zz}) \\ 0 &= (\lambda + 2\mu)\,\varepsilon_{yy} + \lambda\,(\varepsilon_{xx} + \varepsilon_{zz}) \\ 0 &= (\lambda + 2\mu)\,\varepsilon_{zz} + \lambda\,(\varepsilon_{xx} + \varepsilon_{yy}) \end{aligned} \tag{3.3}$$

Solving for ε_{xx}, ε_{yy}, and ε_{zz} gives

$$\begin{aligned} \varepsilon_{xx} &= \frac{\lambda + \mu}{\mu\,(3\lambda + 2\mu)}\sigma_{xx} \\ \varepsilon_{yy} &= \varepsilon_{zz} = -\frac{\lambda}{2\mu\,(3\lambda + 2\mu)}\sigma_{xx} \end{aligned} \tag{3.4}$$

Thefore, E and ν can be defined as

$$\begin{aligned} E &= \frac{\sigma_{xx}}{\varepsilon_{xx}} \\ &= \frac{\mu\,(3\lambda + 2\mu)}{\lambda + \mu} \end{aligned} \tag{3.5}$$

$$\begin{aligned} \nu &= -\frac{\varepsilon_{yy}}{\varepsilon_{xx}} = -\frac{\varepsilon_{zz}}{\varepsilon_{xx}} \\ &= \frac{\lambda}{2\,(\lambda + \mu)} \end{aligned} \tag{3.6}$$

E is a measure of stiffness of an isotropic elastic material. It has a dimension of pressure. ν is dimensionless and has a maximum value 0.5 when $\mu = 0$. The values range from 0.05 for very hard rock to about 0.45 for soft, poorly unconsolidated material. Incompressible fluids like water cannot sustain shear, so, for them, $\mu = 0$ and $\nu = 0.5$. The bulk modulus, K, is a measure of incompressibility. If a solid is subjected to uniform hydrostatic pressure, it leads to

$$\sigma_{xx} = \sigma_{yy} = \sigma_{zz} = -p$$

$$\sigma_{xy} = \sigma_{yz} = \sigma_{zx} = 0$$

The first three equations in 3.2 give

$$\varepsilon_{xx} = \varepsilon_{yy} = \varepsilon_{zz} = -\frac{p}{3\lambda + 2\mu} \tag{3.7}$$

$$K = -\frac{p}{\triangle} = \lambda + \frac{2}{3}\mu \tag{3.8}$$

Hence, K is the measure of resistance to a change in volume.

3.3 Elastic Waves: P and S Waves

When stress is applied to an elastic medium it undergoes deformation, and stored energy propagates in the form of elastic waves. This equation is derived from Newton's equation of motion: force equals the product of mass and acceleration. The components of force are derived from components of stress acting on an elemental volume representing a particle x at time t. In a homogeneous, isotropic, and linearly elastic medium, the equation of wave motion can be written as:

$$\rho\partial_t^2\mathbf{u} = (\lambda+\mu)\,\nabla\,(\nabla.\mathbf{u}) + \mu\nabla^2\mathbf{u} \tag{3.9}$$

where $\mathbf{u} = u\mathbf{i} + v\mathbf{j} + w\mathbf{k}$. using vector identity

$$\begin{aligned} \nabla^2\mathbf{u} &= \nabla\,(\nabla.\mathbf{u}) - \nabla\times(\nabla\times\mathbf{u}) \\ &= \nabla\,(\mathrm{div}\mathbf{u}) - \nabla\times(\mathrm{curl}\mathbf{u}) \end{aligned} \tag{3.10}$$

The alternate form of 3.9 can be expressed as:

$$\rho\partial_t^2\mathbf{u} = (\lambda+2\mu)\,\nabla\,(\nabla.\mathbf{u}) - \mu\nabla\times(\nabla\times\mathbf{u}) \tag{3.11}$$

The Helmholtz decomposition states that any arbitary vector field can be expressed as a sum of a curl-free and divergence free form (Ikelle and Amundsen, 2005). The Helmholtz decomposition of elastic displacement field $\mathbf{u}$ is given as:

$$\begin{aligned} \mathbf{u} &= \nabla\chi + \nabla\times\psi, \quad \nabla.\psi = 0 \\ &= \mathbf{u_1} + \mathbf{u_2} \end{aligned} \tag{3.12}$$

with

$$\begin{aligned} \nabla\times\mathbf{u_1} &= \nabla\times(\nabla\chi) = 0 \\ \nabla.\mathbf{u_2} &= \nabla.\,(\nabla\times\psi) = 0 \end{aligned} \tag{3.13}$$

The scalar potential, χ, and vector potential ψ, are called dilational and rotational displacement potentials respectively. Substituting 3.12 into equation 3.11, the following equation is obtained:

$$\begin{aligned}(\lambda+2\mu)\,\nabla\left[\nabla^2-\frac{\rho}{\lambda+2\mu}\partial_t^2\right]\chi\\ -\mu\nabla\times\left[\nabla\times\nabla\times+\frac{\rho}{\mu}\partial_t^2\right]\psi=0\end{aligned}\tag{3.14}$$

Equation 3.14 will exist if the following two equations hold:

$$\left(\nabla^2-V_P^{-2}\partial_t\right)\chi=0\tag{3.15}$$

$$\left(\nabla\times\nabla\times+V_S^{-2}\partial_t^2\right)\psi=0\tag{3.16}$$

Equation 3.15 is the wave equation for scalar potential, χ, also known as P wave displacement potential. The medium is alternately compressed and dilated in the direction of the wave propagation. Equation 3.16 represents the wave equation for vector potential ψ, also known as shear wave displacement potential. Since $\nabla.\mathbf{u}=0$ for this type of displacement, it means that the medium is displaced perpendicular to the direction of propagation of the wave. The displacement in S wave propagation can have any direction in the plane normal to the direction of the wave. The waves are called vertically polarized SV and horizontally polarized SH shear waves. Figure 3.1 shows the particle motion of P and S waves traveling in the x-direction. The vertically and horizontally polarized S waves are also shown in Figure 3.1. It can be observed that the scalar and vector potential of the displacement field serve to uncouple the elastodynamics wave equation into two wave equations, traveling with distinct velocities V_p and V_s. This uncoupling holds only in an infinite homogeneous medium, i.e. if motion begins as a P wave, then $\psi=0$ and it will continue to be a P wave. If it begins as an S wave, then $\chi=0$ and it will continue to be an S wave. The presence of a layer or interface in the medium generates a coupling between the P and S waves which is called mode conversion.

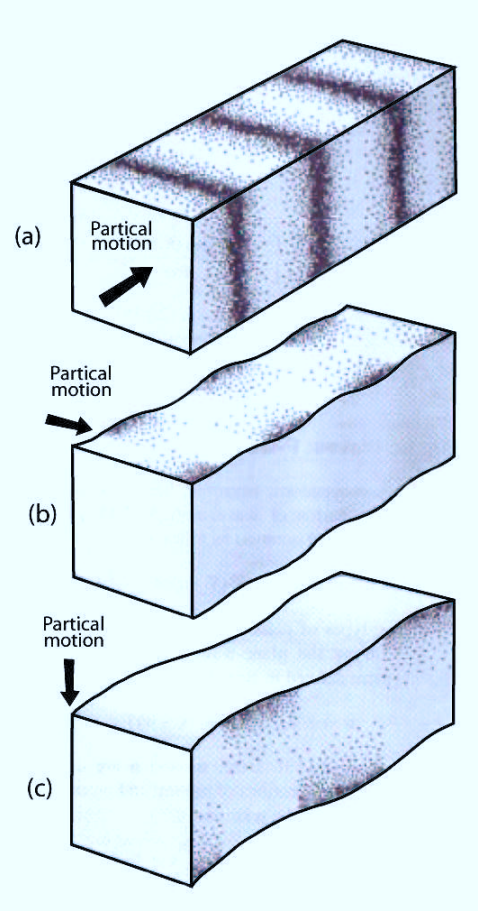

Figure 3.1: P and S waves. Particle motion of P waves (a) along x direction. Particle motion of S wave in two directions (b) horizontal or SH, and (c) vertical or SV motion (from Ikelle and Amundsen 2005).

3.4 Rayleigh, and Love Waves

There are a family of surface waves which can exist at a horizontal interface between two media, where one of the media is a solid. The surface waves for which the displacement of the medium is in the horizontal plane are called horizontally polarized surface waves, and the surface waves for which the displacement of the medium is in the vertical plane are called vertically polarized surface waves. The family of horizontally polarized surface waves are called Love waves (Love, 1911). They are formed by the constructive interference of multiple reflections of SH waves at the free surface. They are the fastest surface waves and move the ground from side-to-side. The particle motion for Love waves is parallel to the surface but perpendicular to the direction of propagation of the wave. The Rayleigh waves are vertically polarized surface waves. In 1885, Rayleigh first predicted the existence of this waves (Rayleigh, 1885) They are generated when the P and SV waves combine in the presence of a free surface, i.e. in an air-solid interface. Rayleigh waves move the ground up and down and side-to-side in the same direction that the wave is moving. Most of the shaking felt from an earthquake is due to Rayleigh waves, which can be much larger than the other waves. Rayleigh waves will be discussed in more detail since these waves are of interest for near surface imaging. Figure 3.2 shows the particle motion of Love and Rayleigh waves.

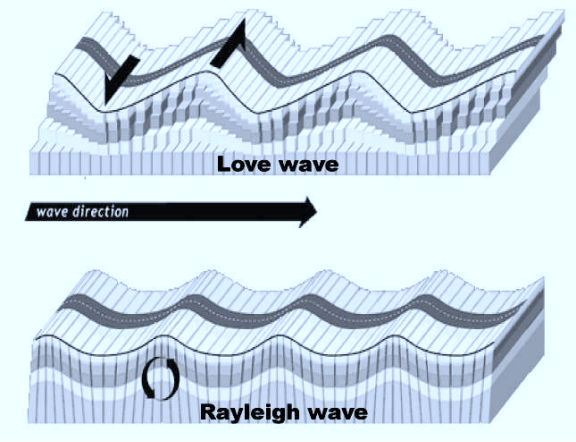

Figure 3.2: Schematic diagram that shows the particle motion of Love and Rayleigh waves (from http://www.exploratorium.edu).

3.5 Rayleigh Waves Solution Using a Plane Wave

Rayleigh waves are not the homogeneous plane wave solution for an elastic wave equation (Ikelle and Amundsen, 2005). The homogeneous plane wave is in the form:

$$\exp\left[ik_p\left(x\sin\theta + z\cos\theta\right) - i\omega t\right]; \quad k_p = \omega/V_p \tag{3.17}$$

Equation 3.17 represents a downward travelling plane P wave in the positive x direction. Vp and θ are the propagation velocity and direction relative to the x-axis respectively. The phase velocity of the plane wave in the x-axis direction is $v = V_p/\sin\theta$ and the phase velocity of the plane wave in the z-axis direction is $v = V_p/\cos\theta$. The horizontal wave number k can be expressed as:

$$k = \omega/v = kp\sin\theta \tag{3.18}$$

Therefore,

$$k_p\cos\theta = \sqrt{k_p^2 - k^2} \tag{3.19}$$

Using Equations 3.18 and 3.19, Equation 3.17 can be rewritten as:

$$\exp\left\{i\left[\sqrt{k_p^2 - k^2 z} + kx - \omega t\right]\right\} \tag{3.20}$$

For $k \geq k_p$, Equation 3.20 takes the form

$$\exp\left\{\pm k\left[\sqrt{1 - \left(k_p/k\right)^2}|z|\right] + i\left(kx - \omega t\right)\right\} \tag{3.21}$$

Equation 3.21 is also a solution of the scalar wave equation. This solution shows that a wave is traveling in the positive x direction and is decaying exponentially as $z \to \infty$. It is noted that when $k < k_p$, then $v < V_p$ and the factor $\cos\theta$ becomes imaginary. This means that the source only excites a wave with a curved wavefront in seismic experiment and the surface waves formed by diffraction of incoming P or S waves at the interface of the curved wavefront (Ikelle and Amundsen, 2005). The source must be placed very near the surface in order to excite high amplitudes of Rayleigh waves.

3.6 Characteristic Equation Governing the Particle Motion of Rayleigh Waves

Rayleigh waves travel along the free surface of a solid medium. Therefore there is no vertical stress on the boundary. i.e. if we consider an xy plane with the z-axis being positive downward, then $\sigma_{zz} = \sigma_{xz} = 0$. The surface wave considered has polarization in the vertical plane, with vanishing displacement with increasing y direction. The displacement potentials associated with inhomogeneous plane P and SV wave modes are considered to be χ and ψ respectively, traveling with a velocity V in the x direction. They can be expressed as:

$$\chi = Ae^{-mkz}e^{jk(x-V_Rt)}, \quad \psi_V = Be^{-nkz}e^{jk(x-V_Rt)} \tag{3.22}$$

where V_R is the velocity of the Rayleigh waves, and m and n are real positive constants which allow the amplitudes to decrease away from the surface. Substituting χ and ψ_V in equations 3.15 and 3.16 gives:

$$m^2 = \left(1 - V_R^2/\alpha^2\right), \quad n^2 = \left(1 - V_R/\beta^2\right) \tag{3.23}$$

where $\alpha = (\lambda + 2\mu)/\rho$ and $\beta = \mu/\rho$ represent P and S wave velocities. Since m and n are real and positive, $V_R < \beta < \alpha$. Hence, the velocity of the Rayleigh waves is less than the S wave velocity. The stress-free boundary condition at $z = 0$ gives

$$\begin{aligned} \sigma_{zz} &= \lambda\nabla^2\chi + 2\mu\left(\frac{\partial^2\chi}{\partial z^2} - \frac{\partial^2\psi_V}{\partial x\partial z}\right) = 0 \\ \sigma_{xz} &= \mu\left(2\frac{\partial^2\chi}{\partial x\partial z} + \frac{\partial^2\chi_V}{\partial z^2} - \frac{\partial^2\chi_V}{\partial x^2}\right) = 0 \end{aligned} \tag{3.24}$$

Substituting 3.22 into equation 3.24 and simplifying yields the characteristic equation of Rayleigh waves as

$$V_R^6 - 8\beta^2V_R^4 + \left(24 - 16\beta^2/\alpha^2\right)\beta^4V_R^2 + 16\left(\beta^2/\alpha^2 - 1\right)\beta^6 = 0 \tag{3.25}$$

For given values of α and β, one solution of Equation 3.25 exists for $0 < V_R < \beta$. If $V_R = 0$, then left hand side of Equation 3.25 is negative, and for $V_R = V_S$, the left

hand side becomes positive. Thus, there must be one real root of Equation 3.25 lying between 0 and V_S, and that root is the velocity of the Rayleigh waves. In general, for many rocks the value of $\beta/\alpha = 1/3$. Using this value, Equation 3.25 gives three roots which are $V_R^2 = 4\beta^2, 2\left(1 \pm 1/\sqrt{3}\right)\beta^2$. Since V_R/β has to be less than one, the only solution is $V_R^2 = 2\left(1 - 1/\sqrt{3}\right)\beta^2$ or $V_R = 0.919\beta$. Hence, we have the values : $V_R/\alpha = 0.531$, $m = 0.848$, $n = 0.393$, and $B/A = +1.468j$. Substituting all these into Equation 3.22 gives

$$\begin{aligned} \chi &= Ae^{-0.848kz}e^{jk(x-V_Rt)} \\ \psi_v &= 1.468jAe^{-0.393kz}e^{jk(x-V_Rt)} \end{aligned}$$

Substituting the values of χ and ψ in $u = \frac{\partial\chi}{\partial x} + \frac{\partial\psi}{\partial z}$ and $w = \frac{\partial\chi}{\partial z} - \frac{\partial\psi}{\partial x}$ yields the particle displacement at the surface:

$$\begin{aligned} u &= -0.423kA\sin k\left(x - V_Rt\right) \\ w &= 0.620kA\cos k\left(x - V_Rt\right) \end{aligned} \tag{3.26}$$

Therefore, any point on the surface describes an ellipse in the vertical xz plane as shown in Figure 3.3

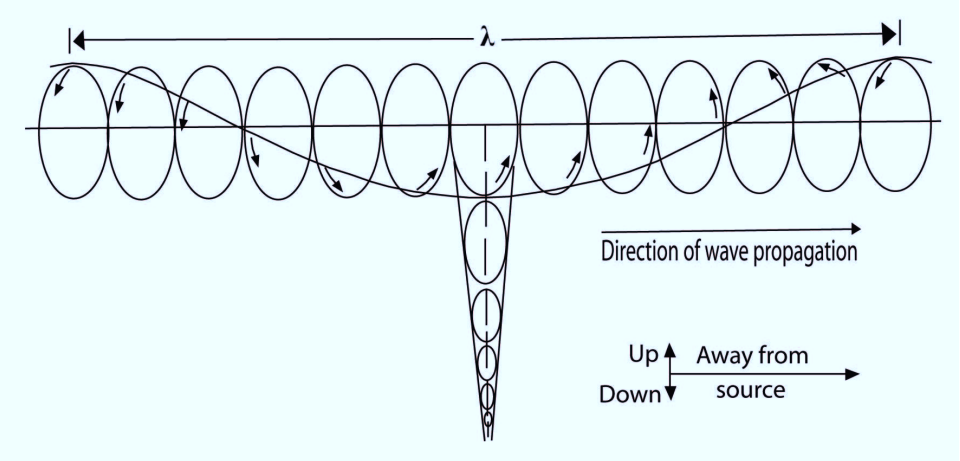

Figure 3.3: Schematic diagram that shows the particle motion of Rayleigh waves and diminishing with depth (from Sheriff and Geldart 1998).

The characteristic equation of Rayleigh waves shows that the velocity of Rayleigh waves is not a function of frequency. Hence, they are not dispersive in a homogeneous medium and travel with a velocity which is slightly less than the S wave velocity. Rayleigh waves become dispersive in a heterogeneous medium though. The real earth is not ideally isotropic and homogeneous, in which case Rayleigh waves become dispersive. Rayleigh waves are low velocity and low frequency waves with a broad frequency spectrum. The different frequencies travel with different velocities in the medium. However, most of the energy is confined to a zone between one to two wavelengths thick.

Chapter 4

Methodology

4.1 Overview

A near surface anomaly introduces lateral heterogeneity in the subsurface. The traditional flat layer assumption for imaging and analysis of a shallow subsurface using Rayleigh wave become unrealistic when near surface anomalies or lateral heterogeneity exist in the subsurface. In order to overcome the difficulty of a flat layer assumption, this research develops an improved methodology for near surface investigation using Rayleigh waves. The methodology begins with the numerical modeling of Rayleigh waves using a 2-D elastic wave equation finite difference technique. The multichannel record is divided into lateral panels of sequences of traces to resolve the lateral heterogeneity and a dispersion curve is computed in each panel using a slant stack technique. A parametric study is performed to analyze the effect of different parameters on Rayleigh wave propagation. Finally, an inversion algorithm is developed on the basis of the parametric study to obtain a subsurface image. This chapter focuses on the detailed methodology which is used to obtain near surface images using Rayleigh waves.

4.2 Numerical Modeling of Rayleigh Waves

Numerical modeling plays an important role in evaluating the reliability and performance of any geophysical technique. Furthermore, the wave propagation phenomenon in complex subsurface geometry cannot be studied without modeling. A finite difference technique has been using to solve an elastic wave equation to compute the seismograms of different models of exploration interest (Alterman and Karal, 1968), (Kelly et al., 1976), (Aki and Richards, 1980) and (Boore, 1972). Different wave

modes can be identified in those seismograms. The finite different time domain technique is also used to study the effect of the near surface anomaly on Rayleigh wave propagation (Leparoux et al., 2000). The effect of the spectral content of Rayleigh waves according to the depth of the anomaly can be observed on synthetic dispersion curves which are generated from Rayleigh wave numerical data (Ganji et al., 1997), (Hevin et al., 1992) and (Gelis et al., 2005). Hence, the forward modeling of Rayleigh waves is crucial in order to analyze the effect of different parameters on their propagation. The parametric study of Rayleigh waves is not only useful for developing an inversion algorithm, but also helps to reveal the material properties and structural organization of the subsurface which can affect the dispersion curve.

4.2.1 Elastic Wave Equation and Discretization in a Staggered Grid

In order to generate synthetic Rayleigh waves data, a 2-D finite difference elastic wave modeling package was needed and has been developed for this research. Numerical formulation of wave equations uses velocity-stress components in modeling code (Virieux, 1986). The elastic wave equation in a first-order hyperbolic system is given as follows:

$$\begin{aligned}
\frac{\partial v_x}{\partial t} &= b\left(\frac{\partial \tau_{xx}}{\partial x}+\frac{\partial \tau_{xz}}{\partial z}\right), \\
\frac{\partial v_z}{\partial t} &= b\left(\frac{\partial \tau_{xz}}{\partial x}+\frac{\partial \tau_{zz}}{\partial z}\right), \\
\frac{\partial \tau_{xx}}{\partial t} &= (\lambda+2\mu)\frac{\partial v_x}{\partial x}+\lambda\frac{\partial v_z}{\partial z}, \\
\frac{\partial \tau_{zz}}{\partial t} &= (\lambda+2\mu)\frac{\partial v_z}{\partial z}+\lambda\frac{\partial v_x}{\partial x}, \\
\frac{\partial \tau_{xz}}{\partial t} &= \mu\left(\frac{\partial v_x}{\partial z}+\frac{\partial v_z}{\partial x}\right),
\end{aligned} \tag{4.1}$$

where (v_x, v_z) is the velocity vector, $(\tau_{xx}, \tau_{zz}, \tau_{xz})$ is the stress tensor, $b = 1/\rho\,(x, z)$ is lightness, $\lambda\,(x, z)$ and $\mu\,(x, z)$ are *Lamé* parameters. All derivatives of first-order elastic wave equations are discretized by using a first-order central difference formulation. This leads to a unique staggered grid which allows computation of the different components of velocity and stress at different node points. Figure 4.1 represents the

staggered stencil which is used in the modeling code. The discretization of the above elastic wave equation is given below:

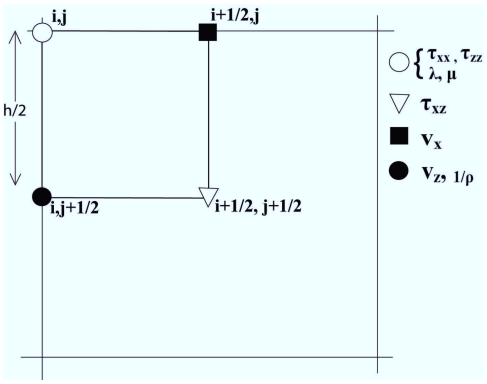

Figure 4.1: 2-D staggered grid stencil.

$$
\begin{aligned}
(v_x)^{k+\frac{1}{2}}_{i+\frac{1}{2},j} &= (v_x)^{k-\frac{1}{2}}_{i+\frac{1}{2},j} + b_{i+\frac{1}{2},j}\frac{\triangle t}{\triangle x}\left\{(\tau_{xx})^{k}_{i+1,j} - (\tau_{xx})^{k}_{i,j}\right\} \\
&\quad + b_{i+\frac{1}{2},j}\frac{\triangle t}{\triangle z}\left\{(\tau_{xz})^{k}_{i+\frac{1}{2},j+\frac{1}{2}} - (\tau_{xz})^{k}_{i+\frac{1}{2},j-\frac{1}{2}}\right\}, \\
(v_z)^{k+\frac{1}{2}}_{i,j+\frac{1}{2}} &= (v_z)^{k-\frac{1}{2}}_{i,j+\frac{1}{2}} + b_{i,j+\frac{1}{2}}\frac{\triangle t}{\triangle x}\left\{(\tau_{xz})^{k}_{i+\frac{1}{2},j+\frac{1}{2}} - (\tau_{xz})^{k}_{i-\frac{1}{2},j+\frac{1}{2}}\right\} \\
&\quad + b_{i,j+\frac{1}{2}}\frac{\triangle t}{\triangle z}\left\{(\tau_{zz})^{k}_{i,j+1} - (\tau_{zz})^{k}_{i,j}\right\}, \\
(\tau_{xx})^{k+1}_{i,j} &= (\tau_{xx})^{k}_{i,j} + (\lambda+2\mu)_{i,j}\frac{\triangle t}{\triangle x}\left\{(v_x)^{k+\frac{1}{2}}_{i+\frac{1}{2},j} - (v_x)^{k+\frac{1}{2}}_{i-\frac{1}{2},j}\right\} \\
&\quad + \lambda_{i,j}\frac{\triangle t}{\triangle z}\left\{(v_z)^{k+\frac{1}{2}}_{i,j+\frac{1}{2}} - (v_z)^{k+\frac{1}{2}}_{i,j-\frac{1}{2}}\right\}, \\
(\tau_{zz})^{k+1}_{i,j} &= (\tau_{zz})^{k}_{i,j} + (\lambda+2\mu)_{i,j}\frac{\triangle t}{\triangle z}\left\{(v_z)^{k+\frac{1}{2}}_{i,j+\frac{1}{2}} - (v_z)^{k+\frac{1}{2}}_{i,j-\frac{1}{2}}\right\} \\
&\quad + \lambda_{i,j}\frac{\triangle t}{\triangle x}\left\{(v_x)^{k+\frac{1}{2}}_{i+\frac{1}{2},j} - (v_x)^{k+\frac{1}{2}}_{i-\frac{1}{2},j}\right\}, \\
(\tau_{xz})^{k+1}_{i+\frac{1}{2},j+\frac{1}{2}} &= (\tau_{xz})^{k}_{i+\frac{1}{2},j+\frac{1}{2}} + \mu_{i+\frac{1}{2},j+\frac{1}{2}}\frac{\triangle t}{\triangle z}\left\{(v_x)^{k+\frac{1}{2}}_{i+\frac{1}{2},j+1} - (v_x)^{k+\frac{1}{2}}_{i+\frac{1}{2},j}\right\} \\
&\quad + \mu_{i+\frac{1}{2},j+\frac{1}{2}}\frac{\triangle t}{\triangle x}\left\{(v_z)^{k+\frac{1}{2}}_{i+1,j+\frac{1}{2}} - (v_z)^{k+\frac{1}{2}}_{i,j+\frac{1}{2}}\right\},
\end{aligned}
$$

where the i and j indices represent space and the k index represents time. $\triangle x = \triangle z = h$. The components of velocity and stress of the elastic wave equation in the staggered grid stencil are evaluated at the following locations:

$$
\begin{aligned}
v_x\left(\left(i-1/2\right)h,\left(j-3/2\right)h,k\triangle t\right)\\
v_z\left(\left(i-1\right)h,\left(j-1\right)h,k\triangle t\right)\\
\tau_{xx}\left(\left(i-1\right)h,\left(j-3/2\right)h,\left(k+1/2\right)\triangle t\right)\\
\tau_{zz}\left(\left(i-1\right)h,\left(j-3/2\right)h,\left(k+1/2\right)\triangle t\right)\\
\tau_{xz}\left(\left(i-1/2\right)h,\left(j-1\right)h,\left(k+1/2\right)\triangle t\right).
\end{aligned}
$$

4.2.2 Initial and Boundary Conditions

The medium is considered to be at equilibrium at time $t = 0$. Hence, velocity and stress are set to zero everywhere in the medium. The stress-free boundary condition is implemented at the top of the model i.e., vertical stresses are considered zero at the surface or

$$\tau_{xz} = \tau_{zz} = 0 \quad ; \quad at \quad z = 0. \tag{4.2}$$

Equation 4.2 can be expressed in staggered grid nodes as :

$$
\begin{aligned}
\tau_{xz}\left(\left(i-1/2\right)h,0,\left(k+1/2\right)\triangle t\right)=0,\\
\left(\tau_{zz}\left(i-1\right)h,-1/2h,\left(k+1/2\right)\triangle t+\tau_{zz}\left(i-1\right)h,+1/2h,\left(k+1/2\right)\triangle t\right)=0,
\end{aligned}
$$

τ_{xx} and v_x are never computed in the node points which are above the surface i.e. $z < 0$. The absorbing or sponge boundary conditions are used on the other three edges of the model (Bording, 2004) and (Chen et al., 2010).

4.2.3 Numerical Modeling Source

A Ricker wavelet is used as the source in finite difference formulation. The velocity components v_x and v_z are computed at the source point and added to the stress components τ_{xx}, τ_{zz} and τ_{xz}. The source function is given by:

$$S_r\left(t\right) = \left(1-2\left(\pi f_{max}\right)^2\left(t-t_1\right)^2\right)\exp\left(-\left(\pi f_{max}\right)^2\left(t-t_1\right)^2\right), \tag{4.3}$$

where, f_{max} is the maximum source frequency and $t_1 = \sqrt{\left(\log\left(1.0E5\right)\right)/\left(\pi f_{max}\right)^2}$ is the time delay.

4.3 Dispersion Curve Computation

Accurate computation of the Rayleigh wave dispersion curve is important in order to obtain the S wave velocity stiffness profile through inversion. There are several different techniques to compute Rayleigh wave dispersion curves. In the frequency wave number or FK transform (Foti, 2000), time domain x-t data are transformed into the FK domain. The phase velocity at each frequency is computed by using the equation $v = \frac{f}{k}$, where v, f and k are phase velocity, frequency, and wave number respectively. In the τ-p transform (McMechan and Yedlin, 1981), time domain, or x-t data are first transformed into the τ-p domain and time or p is converted into frequency. In computing dispersion curves, all these transform techniques assume that subsurface layers are flat and there is no lateral variation in velocities. The smooth image of a dispersion curve obtained by averaging all traces in FK and τ-p techniques may miss the localized anomaly zone in the lateral direction. Cross-power spectra calculation (Xu and Butt, 2006) can be used to compute a dispersion curve for every two channels of a multichannel array where the subsurface consists of lateral heterogeneity. The signal-to-noise ratio in this method is very low. Considering all advantages and disadvantages of the above mentioned techniques of computing dispersion curves, this dissertation presents a new and innovative idea of laterally panelizing multichannel data into a sequence of traces, and then using localized processing using a slant stack technique (Xia et al., 2007).

4.3.1 Slant Stack Technique

A slant stack is a transformation technique where a wave-field can be decomposed into its plane wave components, each traveling at a certain angle from the vertical (Yilmaz, 1987). The time delay associated with a plane wave that travels at an angle θ from the vertical is given by:

$$\triangle t = (\sin\theta / v)\, \triangle x, \tag{4.4}$$

where the quantity $\sin\theta/v$, is the inverse of the horizontal phase velocity, which is also known as the ray parameter or p. According to Snell's law, the ray parameter p

is constant along a ray path in a layered medium. Equation 4.4 can be rewritten as:

$$\triangle t = p \triangle x. \tag{4.5}$$

When a plane wave travels in a layered earth, it changes its direction of propagation at each layered boundary. Therefore, the ray path associated with a single p value can be traced if the velocities of the earth model are known. Since, the receivers at all offsets record plane waves of many p values, an offset gather contains plane waves of many p values. In order to decompose the offset gather into plane wave components, the first step is to apply LMO correction to the data (Yilmaz, 1987):

$$\tau = t - px, \tag{4.6}$$

where p is the ray parameter, x is the offset, t is the two-way travel time, and τ is the linearly moved out time. Next, the LMO corrected data are summed over the offset axis to obtain:

$$S(p, \tau) = \sum_{x} P\left(x, \tau + px\right), \tag{4.7}$$

where, $S\left(p, \tau\right)$ represents a plane wave with ray parameter $p \sin\theta / v$. A complete slant stack gather or p gather can be obtained by repeating the LMO for various p values and performing the sum along the offset axis.

4.3.2 Dispersion Curve Computation by Slant-Stacking Multichannel Swept-Frequency Data

In this technique, each trace of multichannel impulsive data $x_{i,j}$ is convolved with a linear sweep source, $S\left(t\right)$ of a certain frequency range. The i and j indices are the grid point in the x and z axes respectively. This results in stretching $x_{i,j}$ into frequency sweep data $X_{i,j}$ where all Rayleigh wave frequencies get separated from lower to higher frequency in linear order. In order to resolve lateral heterogeneity or dipping layers, stretched data are divided into a number of panels consisting of sequences of traces in each panel (Sharma et al., 2008). Next, LMO is applied to each panel and the amplitudes are summed over the offset axis, which is also known as slant stacking. This will give the image in the time-velocity domain. Finally, time is converted into frequency from their linear relationship. The maximum coherency of

the amplitude trend in the velocity frequency domain maps the required dispersion curve.

4.3.3 Sweep Frequency Data

Each trace of the multichannel record $x_{i,j}$ is convolved with a sweep source $S(t)$ to obtain :

$$X_{i,j} = x_{i,j} * S(t),$$

where * denotes the convolution operation. The sweep source is a sinusoidal function which is represented as:

$$S(t) = \sin\left(2\pi f_1 t + \frac{\pi (f_2 - f_1)}{T} t^2\right),$$

where f_1 and f_2 are the minimum and maximum frequency of the sweep source. The total time length of sweep is given by T. Figure 4.2 shows the convolution of multichannel data with a 10 second long linear sweep source. Stretched data is shown in Figure 4.3. Frequency separation of the Rayleigh wave from low to high frequencies over time is observed. The phase velocity of Rayleigh waves can be computed by just measuring the slope at different frequencies using the slant stack.

4.4 The Fitness Function Developed for Rayleigh Wave Inversion

The multichannel data is collected using two survey lines. Each survey line has two front and back shots at each end of the line. These four shot records with 96 receivers for each shot are added together. Each shot record is then divided into six panels of sequences of traces. This gives a total of 24 panels from all four shot records. The dispersion curve is computed for all 24 panels using the slant stack technique, which is an amplitude plot for each frequency for all velocities. To generate a smooth image, the amplitudes for the time samples are summed till zero-crossing. The frequency samples are computed in each zero-crossing. Therefore the frequency samples are not evenly spaced in the dispersion curve. The required fitness function for the minimization is the sum of the square of differences of the corresponding reference and model dispersion curves. In order to subtract the amplitude of the corresponding

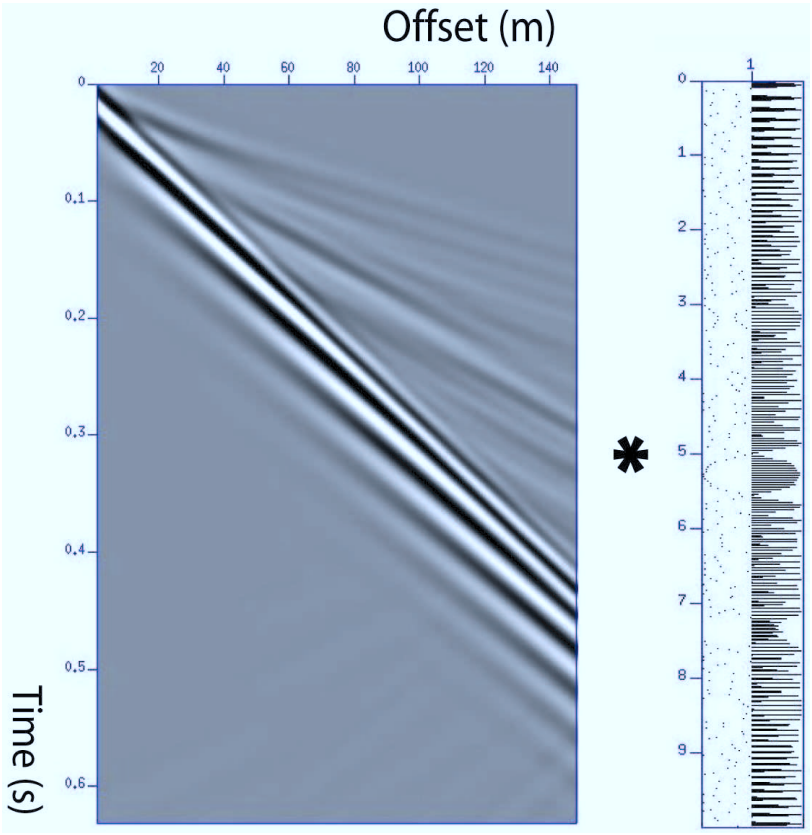

Figure 4.2: Convolution of multichannel data with a linear sweep source.

dispersion curve of model data from reference data, both frequency and velocity samples of model and reference data must be identical. The steps to compute the fitness function are given below:

- Compute the dispersion curves for front and back shots of two survey lines for the reference data of the Stellarton field. Develop a numerical model which to mimic the reference data. Generate a synthetic shot records and compute the dispersion curves for all four shots of the numerical model.

- Sort the combined frequency samples of both reference and model dispersion curves in increasing order.

- Interpolate or extrapolate the amplitudes for all velocities in both reference and model dispersion curves for missing frequencies. This will construct the reference and model dispersion curves with identical velocity and frequency

samples.

- Compute the fitness function by integrating the square of the difference of the corresponding amplitudes of the reference and the model dispersion curves along the velocity and frequency axes.

$$F = \iint \left(A_{ref} - A_{mod}\right)^2 \, dv \, df,$$

where dv and df are, respectively, velocity, and frequency sample. A_{ref} and A_{mod} are, respectively, the amplitude arrays of the reference and model dispersion curves.

- Sum all the fitness functions obtained from the corresponding panels of the model and reference dispersion curves. The total value of the fitness function is then divided by the number of panels.

4.5 Pseudo Code of VFSR Inversion

In order to develop the VFSR algorithm, the cost function F for initial parameters X and the re-annealing temperature need to be computed. The algorithm for very fast simulated annealing described in (Sen and Stoffa, 1995) given below, and is the method used to invert the dispersion curves in this research.

do loop over temperature T_k

do loop over the number of iterations at same temperature T

do loop over the model parameters X_i

$U_i \in U\,[0,1]$

$Y_i = sgn\left(U_i - \frac{1}{2}\right) T_i \left[\left(1 + \frac{1}{T_i}\right)^{|2U_i - 1|} - 1\right]$

$XN_i = X_i + Y_i\,(UB_i - LB_i)$

$LB_i \leq XN_i \leq UB_i$

enddo

Compute the cost function FN *using updated parameter* XN_i

if FN $<$ F *then*

$\mathbf{X} = \mathbf{XN}$

F = FN

endif

else

$P = exp\left(\frac{-(FN-F)}{\mathrm{T}}\right)$

call random number PP

P > PP *then*

X = XN

F=FN

endif

endif

reanneal temperature after certain iteration

enddo

enddo

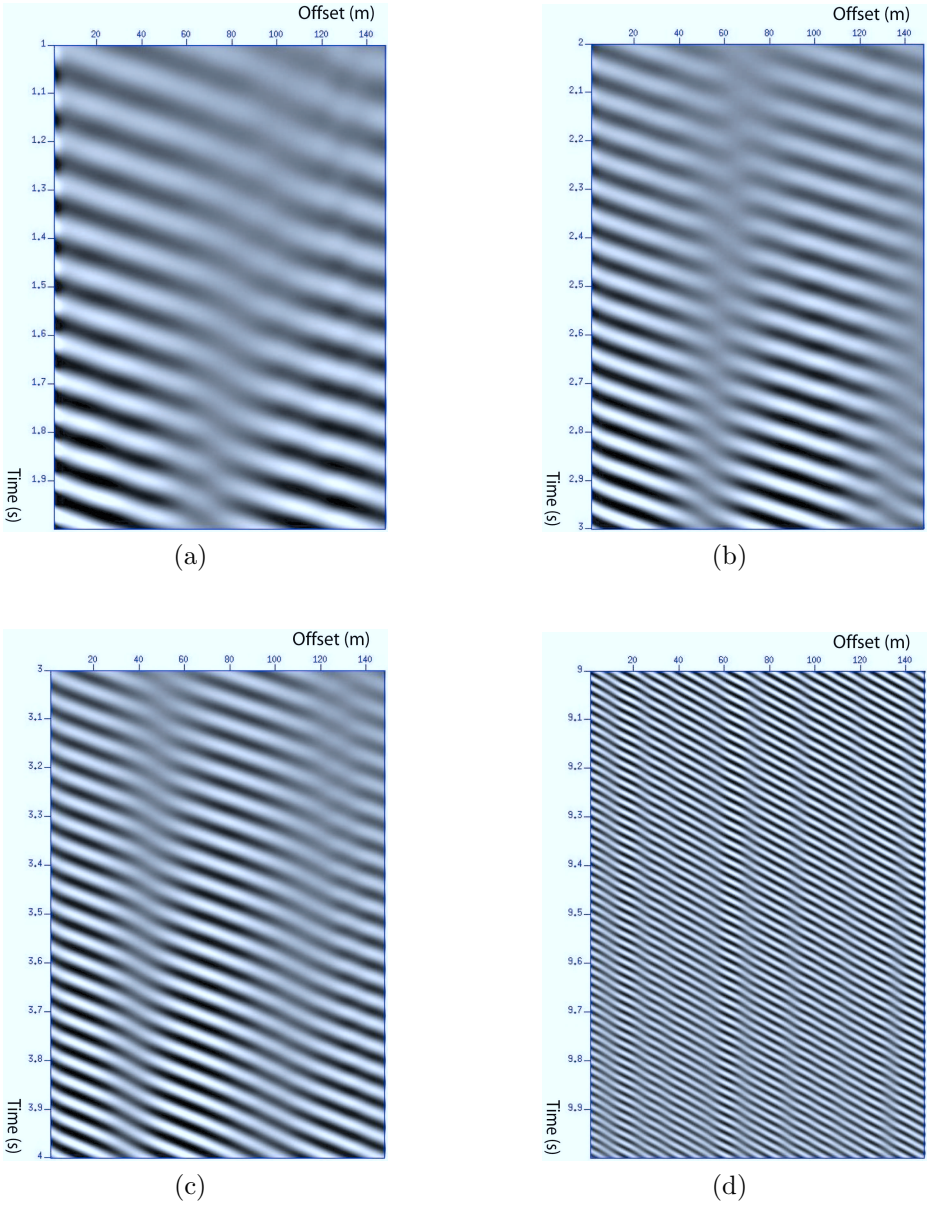

Figure 4.3: Stretched data (a) 1 - 2sec, (b) 2 - 3sec, (c) 3 - 4sec and (d) 9 - 10sec.

Chapter 5

The Influence of Layer Depth and Dip on the Propagation of Rayleigh Waves

5.1 Overview

The sensitivity analysis of different parameters on Rayleigh wave propagation is important in order to develop an inversion algorithm. These parameters may include structures of the subsurface and associated material properties, i.e., P and S wave velocities, density of the subsurface etc. Dispersion curves of Rayleigh waves may be highly sensitive to some parameters, and less sensitive to others. The number of parameters that need to be updated and fixed in the inverse process depends on the sensitivity of the parameters on Rayleigh waves dispersion curves. This chapter is devoted to the sensitivity analysis of two different structures: layer depth and dip, either of which may present in the subsurface.

5.2 Problem Formulation

A 2-D finite difference elastic wave modeling package was used to generate synthetic Rayleigh waves data for the parametric studies. Numerical formulation of elastic wave equations uses velocity-stress components in the modeling code. All derivatives of elastic wave equations are discretized by using first order central difference formulation. This leads to a unique staggered grid which allows computation of the different components of velocity and stress at different node points. The medium is considered to be at equilibrium at time $t = 0$. Hence, velocity and stress are set to zero everywhere in the medium. The stress free boundary condition was used at the top of the model, i.e. vertical stresses were considered zero. The absorbing boundary conditions were used on other three edges of the model. The detailed formulation of elastic wave equations were presented in Chapter 3.

5.3 Computation of Dispersion Curves

The dispersion curves of Rayleigh waves synthetic data were computed using the slant stack technique. Each trace of multichannel impulsive data, $x_{i,j}$, was convolved with a 10 second long linear sweep source, $S(t)$, with a frequency range from $f_1 = 5$ Hz to $f_2 = 55$ Hz. Slant stack is applied to frequency sweep data $X_{i,j}$ with a range of velocities from $v_{min} = 200$ m/s to $v_{max} = 700$ m/s at increments of 2 m/s. The slope of each velocity is then computed in each time sample and stacked the amplitudes along the offset axis. This gives an image in the time-velocity domain. Time is converted into frequency from their linear relationship, $f(t) = f_1 + (i-1)df$, where df is the sampling frequency and i is the number of time sample. The maximum coherency of the amplitude trend in the velocity, frequency domain is the required dispersion curve.

5.4 Reference Case

A homogeneous model with dimensions of 200 meters by 100 meters is considered the reference model for the parametric studies. The elastic parameters in this model are $Vp = 773$ m/s, $Vs = 413$ m/s, and $\rho = 1.5$ g/cc, where Vp, Vs and ρ represent the P wave, S wave velocity and density of the medium respectively. The number of grid points along the x and z axes are 400 and 200, respectively, with 0.5 meter grid spacing. The source is placed at 21 meters and the first receiver is placed five meters away from the source, the remaining 148 receivers are placed one meter away from each other. The time step used to compute the synthetic seismogram is 4000 with a sampling time 0.0002 second. The shot record computed from this model is shown in Figure B.17. The direct arrival of P wave and S wave are clearly seen in the shot record. P wave is traveling faster than S wave. The Rayleigh wave travels at almost the same velocity with S wave in a homogeneous medium. Therefore, Rayleigh wave cannot be distinguished from S wave in homogeneous medium. Also shown in Figure B.17 is the dispersion curve for the reference case. It is clear that all frequencies of the Rayleigh wave travel with the same velocity, showing the non-dispersive nature of Rayleigh waves in a homogeneous medium.

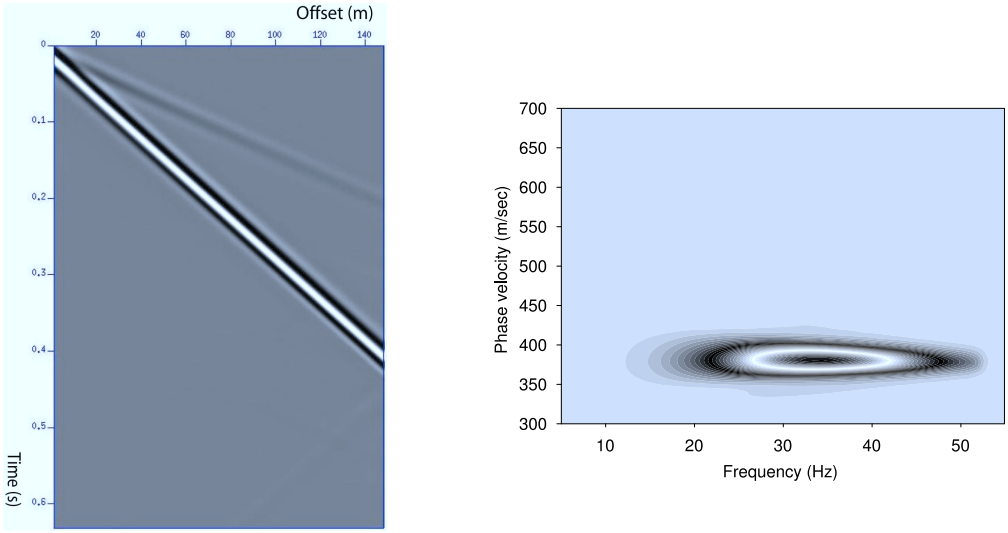

Figure 5.1: Shot record (left) and Rayleigh waves dispersion curve (right) for the reference model.

5.5 The Effect of Layer Depth on the Propagation of Rayleigh Waves

The first parametric study began with the sensitivity analysis of the effect of layer depth on the Rayleigh waves dispersion curve. There are three possible outcomes in this parametric study:

- material properties increase with depth
- material properties decrease with depth
- a soft layer is introduced in between two stiff layers

The shot records and dispersion curves are computed from the models, by placing the interface at different depths in the reference model. The depth of the interfaces are evaluated in terms of wavelengths from the equation as given below:

$$\lambda = \frac{v}{\nu}, \tag{5.1}$$

where λ is the wavelength computed for the velocity v and frequency ν of a wavefield. The minimum S wave velocity considered in each model is 413 m/s and the dominate frequency of the source wavelet is 26 Hz. Therefore, substituting $v = 413$ m/s and $\nu = 26$ Hz into Equation 5.1, yields: $\lambda = 16$ meters. Hence, $\frac{\lambda}{2} = 8$ meters, $\frac{\lambda}{3} = 5.3$

meters, and $\frac{\lambda}{8} = 2$ meters. In all three cases, interface is placed in the range between one wavelength λ to one-eight of a minimum wavelength $\frac{\lambda}{8}$ of the Rayleigh wave.

5.5.1 Case 1: Increasing Velocity with Depth

A parametric study is conducted to analyze the effect of layer depth on Rayleigh wave propagation when the velocity increases with depth. Elastic parameters for the upper and lower layers for these models are given in the Table 5.1

Layers	Vp (m/s)	Vs (m/s)	ρ (g/cc)
1	773	413	1.5
2	1200	683	1.7

Table 5.1: Elastic parameters used in the parametric study of velocity increases with depth.

5.5.1.1 Results Analysis: Increasing Velocity with Depth

In the first model, the interface is placed at λ down from the surface. This is shown in Figure 5.2a. Direct P wave and direct S wave arrival can be observed in the shot record, as shown in Figure 5.3a. The shot record shows that a very small portion of the Rayleigh wave energy travels at a lower velocity than the S wave. The dispersion curve computed from this model is shown in Figure 5.4a. The low frequencies of the Rayleigh wave which are less than 20 Hz are traveling with high velocities of lower layer. All the other frequencies greater than 20 Hz are traveling with the velocity of the low velocities of upper layer, as shown in the dispersion curve. In the second model the interface is placed at $\frac{\lambda}{2}$ down from the surface. This is shown in Figure 5.2b. The phase change of the Rayleigh wave along with direct P and S wave arrivals can be observed in the shot record shown in Figure 5.3b. Figure 5.4b shows that the phase velocities in the dispersion curve decrease with the increase of frequencies. This means that different frequencies of Rayleigh waves penetrate different depths of the medium and show the dispersive nature in a layered medium. The interface is placed at $\frac{\lambda}{3}$ down in the third model, as shown in Figure 5.2c. The phase change of Rayleigh waves along with the direct P wave arrival is clearly observed in the shot

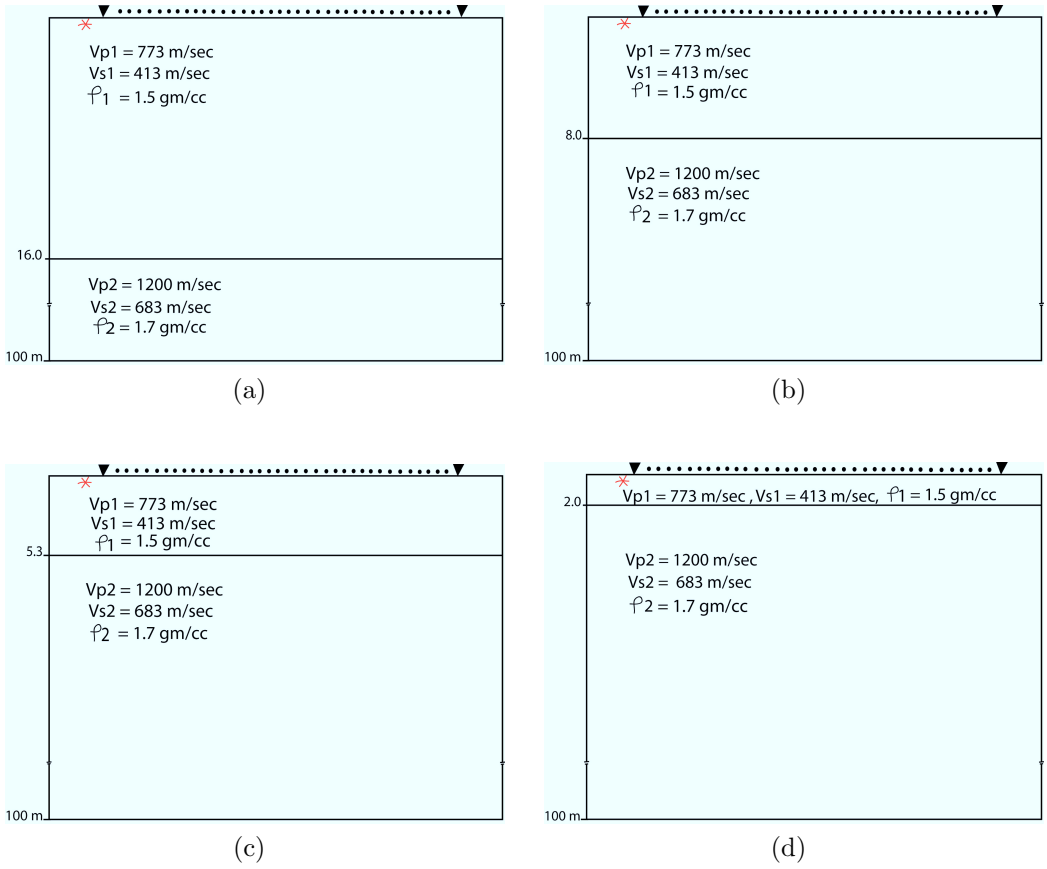

Figure 5.2: The velocity models with the interface placed at (a) λ, (b) $\frac{\lambda}{2}$, (c) $\frac{\lambda}{3}$ and (d) $\frac{\lambda}{8}$.

record of Figure 5.3c. The low frequency waves can be seen at a later time in the shot record than the high frequency waves. The dispersion curve computed from this model is shown in Figure 5.4c. It can be observed that the phase velocity of Rayleigh wave decreases almost linearly with an increase of frequency, i.e. each frequency is traveling with a different phase velocity. Finally, the interface is placed down at $\frac{\lambda}{8}$ as shown in the model of Figure 5.2d. Direct P and S wave arrivals can be observed in the shot record of Figure 5.3d. The depth of the interface is too small in comparison to the wavelength of the Rayleigh waves. Therefore, the maximum energy of Rayleigh waves traveling in the high velocity medium, i.e. in the lower layer. The shot record shows no dispersion and all frequency is traveling with the velocity of the lower layer. This can be seen from the dispersion curve in Figure 5.4d.

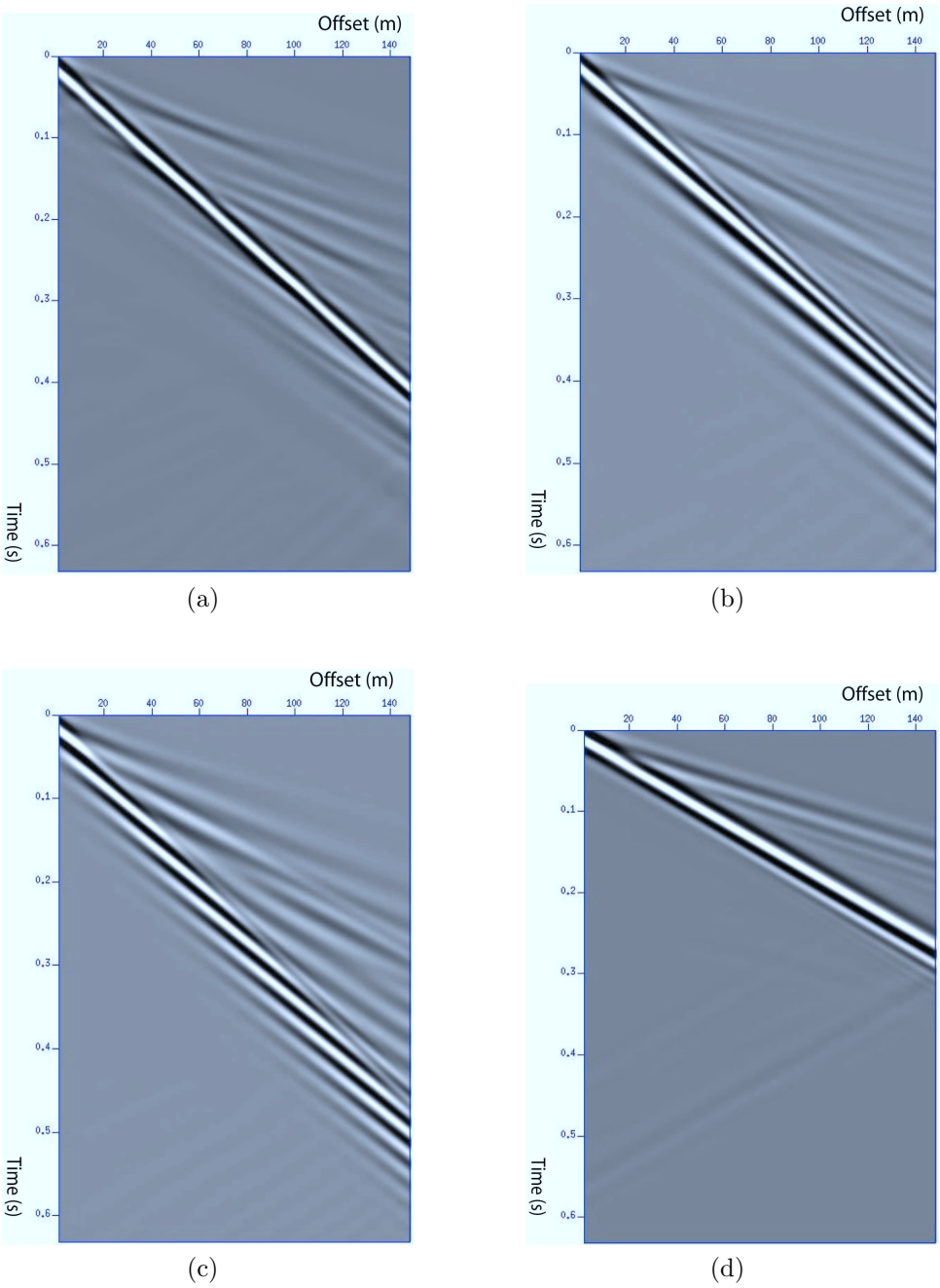

Figure 5.3: Synthetic seismograms for the interface placed at (a) λ, (b) $\frac{\lambda}{2}$, (c) $\frac{\lambda}{3}$, and (d) $\frac{\lambda}{8}$ when velocity increases with depth. Rayleigh waves are dispersed for the interface placed at $\frac{\lambda}{2}$ and $\frac{\lambda}{3}$.

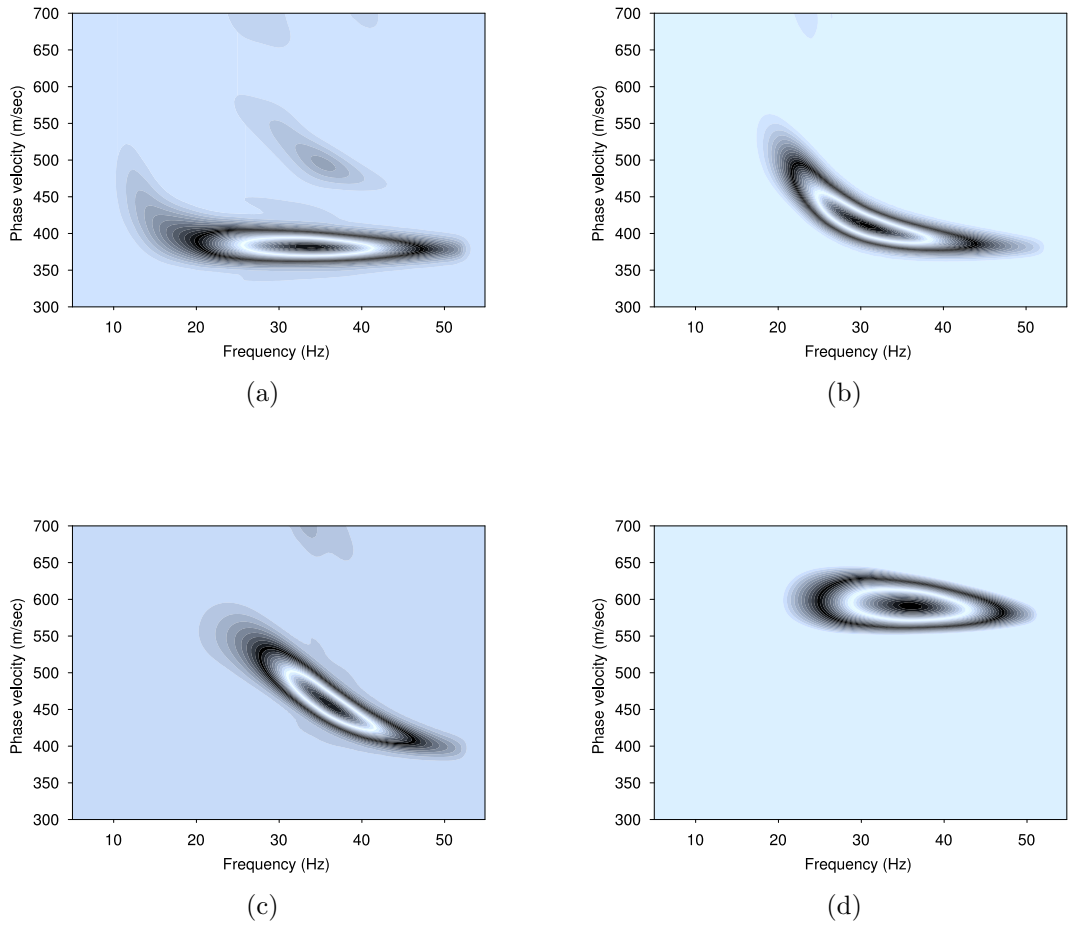

Figure 5.4: Dispersion curves for the interface placed at (a) λ, (b) $\frac{\lambda}{2}$, (c) $\frac{\lambda}{3}$, and (d) $\frac{\lambda}{8}$ when velocity increases with depth. The dispersion curves are more sensitive when the interface is placed at depths of $\frac{\lambda}{2}$ and $\frac{\lambda}{3}$.

5.5.2 Case 2: Decreasing Velocity with Depth

The next parametric study of effect of layer depth are carried out by inverting the velocity fields in the previous models. The elastic parameters used for this parametric study are given in Table 5.2:

Layers	Vp (m/s)	Vs (m/s)	ρ (g/cc)
1	1200	683	1.7
2	773	413	1.5

Table 5.2: Elastic parameters used in the parametric study when velocity decreases with depth.

5.5.2.1 Result Analysis: Decreasing Velocity with Depth

The shot record showed in Figure 5.5a is computed by placing the interface at λ down from the surface. A direct P and S waves arrival can be observed in the shot record. The Rayleigh wave arrives just below the S wave with a slower velocity than S wave. The shot record also shows that the Rayleigh wave changes phase with time. The dispersion curve computed from this model is shown in Figure 5.6a. It can be observed that most of the frequencies of the Rayleigh wave travel with high phase velocity, i.e. travel with the velocity of the upper layer in the dispersion curve. In the second model, the interface is placed at $\frac{\lambda}{2}$ down from the surface. The Rayleigh waves phase change is observed along with the direct arrival of the P wave in the shot record of Figure 5.5b. Figure 5.6b represents the dispersion curve. The phase velocities of the Rayleigh wave increase with the increase of frequencies in the dispersion curve, i.e. there is low frequency travel with a low phase velocity, which is the velocity of the dipper layer, there is high frequency travel with a high phase velocity, which is the velocity of the shallow layer. The Rayleigh waves are more dispersed in the shot record of Figure 5.5c, which is computed by moving the interface up to $\frac{\lambda}{3}$. The phase velocity of the Rayleigh wave increases almost linearly with an increase of frequency in the dispersion curve, as represented in Figure 5.6c. In this case each frequency of the Rayleigh wave travels with a different phase velocity. For the last model, the interface is placed at $\frac{\lambda}{8}$ down from the surface. The direct P and S waves arrivals

are seen in the shot record of Figure 5.5d. Since the depth of the interface is too small in comparison to the wavelength of the Rayleigh wave, most of the energy is traveling with a low phase velocity, i.e. with the velocity of the lower layer, as shown in Figure 5.6d.

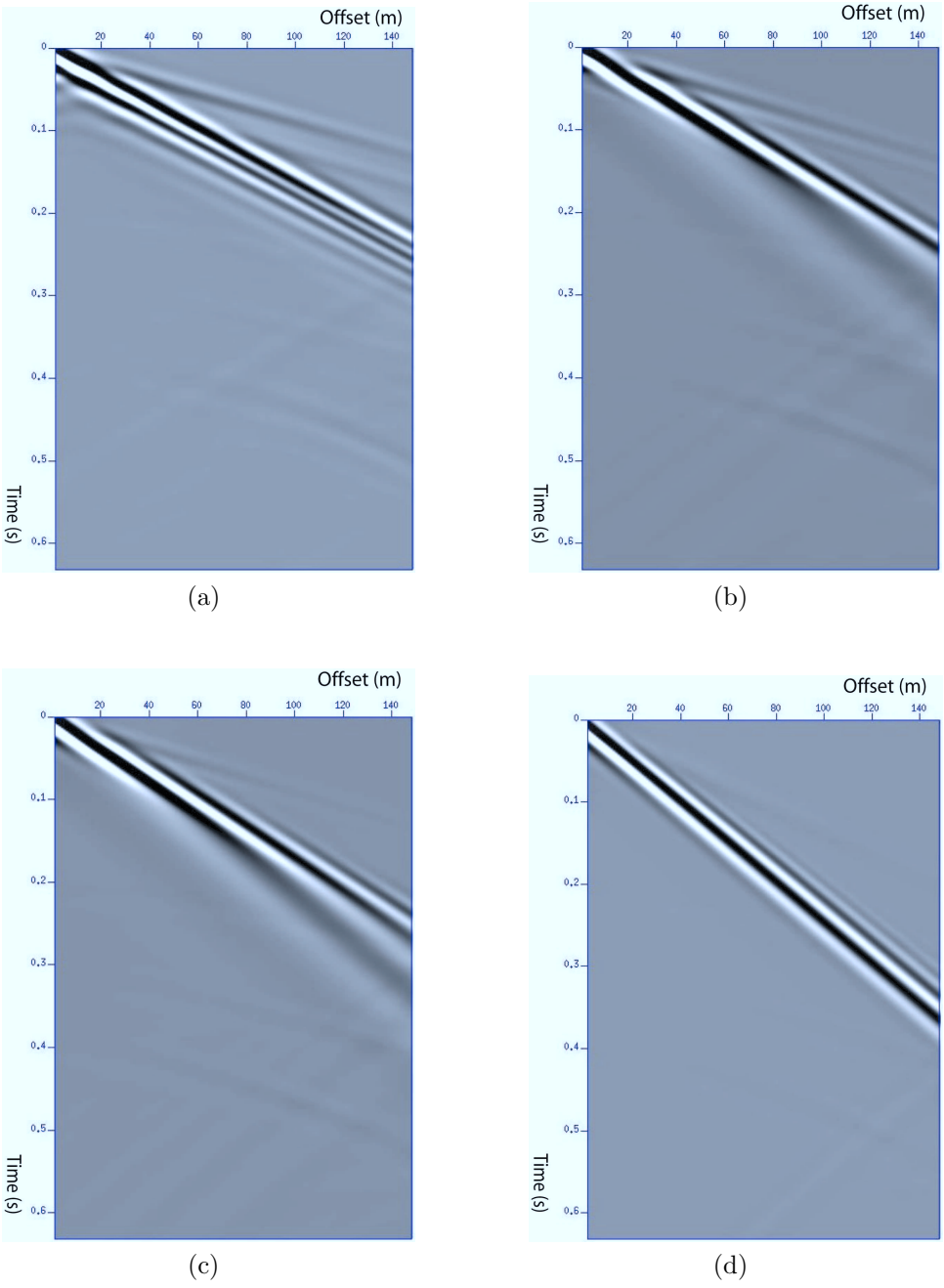

Figure 5.5: Synthetic seismograms for the interface placed at (a) λ, (b) $\frac{\lambda}{2}$, (c) $\frac{\lambda}{3}$ and (d) $\frac{\lambda}{8}$ when velocity decreases with depth. The Rayleigh waves are dispersed when the interface is placed at $\frac{\lambda}{2}$ and $\frac{\lambda}{3}$.

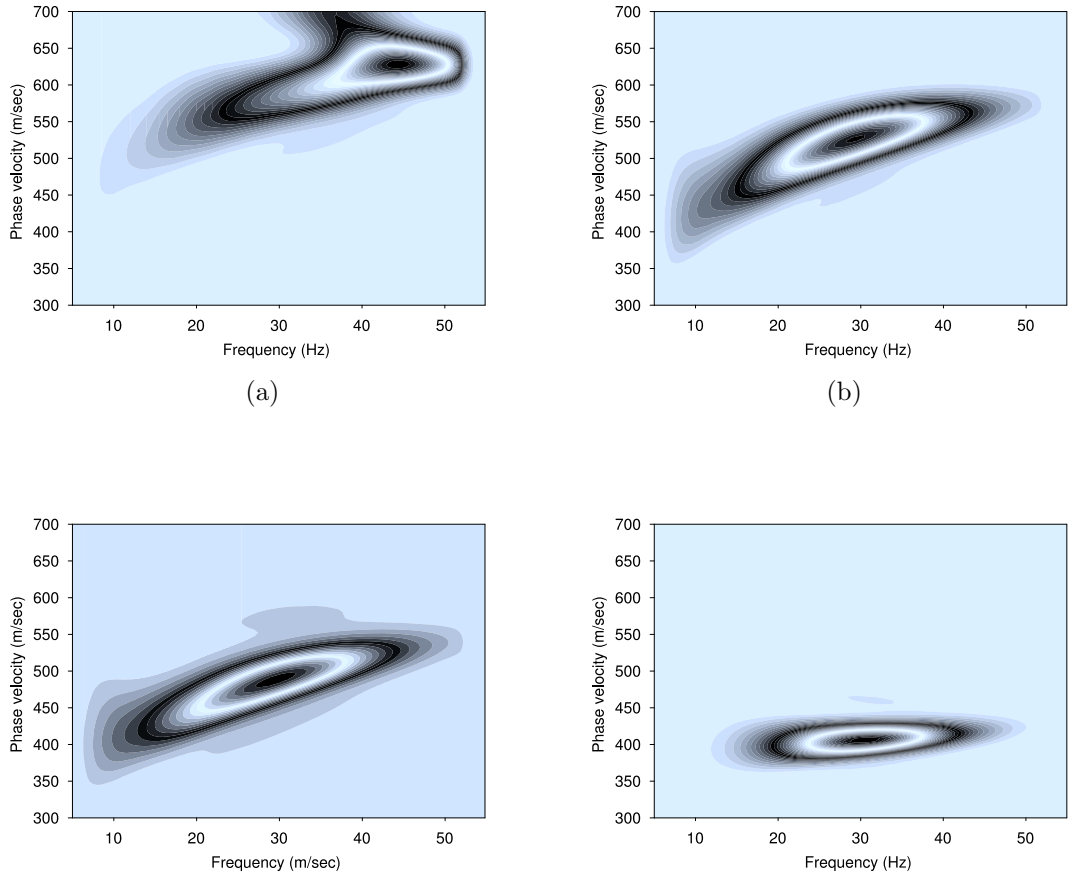

Figure 5.6: Dispersion curves for the interface placed at (a) λ, (b) $\frac{\lambda}{2}$, (c) $\frac{\lambda}{3}$, and (d) $\frac{\lambda}{8}$ when velocity decreases with depth. The dispersion curves are more sensitive when the interface is placed at depths of $\frac{\lambda}{2}$ and $\frac{\lambda}{3}$.

5.5.3 Case 3: Alternate Velocity

The effect of layer depth on Rayleigh wave propagation is also sensitive to an alternate velocity profile. In this parametric study, a soft layer of 6 meter width is introduced in between two stiff velocity layers. The elastic parameters used for this parametric study are given in Table 5.3:

Layers	Vp (m/s)	Vs (m/s)	ρ (g/cc)
1	773	413	1.5
2	450	230	1.2
3	1200	683	1.7

Table 5.3: Elastic parameters used in the parametric study with an alternate velocity layer.

5.5.3.1 Results Analysis: Alternate Velocity Layer

In the first model, the interface is placed at λ down from the surface, as shown in Figure 5.7a. Direct P and S wave arrivals can be observed in the shot record shown in Figure 5.8a. The shot record also shows some trapped energy in between the two layers. The dispersion curve represented in Figure 5.9a shows that most of the Rayleigh waves with a frequency greater than 20 Hz are traveling with the same phase velocity, i.e. with the velocity of the upper layer. The frequencies less than 20 Hz are traveling with a greater phase velocity, i.e. with the velocity of the dipper layer. Due to the presence of the soft layer, the amplitude decay in a particular frequency band is also observed in the dispersion curve. In the second model, the interface is placed at $\frac{\lambda}{2}$ down from the surface as shown in Figure 5.7b. In this case, a direct P wave can be observed in the shot record. The phase change of the Rayleigh wave and the energy trapped in between the two layers are also seen in the shot record of Figure 5.8b. The mode conversion of the Rayleigh wave to a higher mode can be seen in the dispersion curve of Figure 5.9b. The phase velocities of the Rayleigh wave both decreases and increases with the increase of frequencies due the presence of the soft layer in between the two stiff layers. The amplitude attenuation is observed in a particular frequency band in the dispersion curve. Figure 5.7c shows the interface is placed at $\frac{\lambda}{3}$. The direct P wave and the phase change of the Rayleigh waves are observed in the the

shot record of Figure 5.8c. More energy is trapped in the soft layer as the interface is moved closer the surface. The dispersion curve represented in Figure 5.9c shows the higher mode of the Rayleigh waves energy. The phase velocities of Rayleigh wave both decrease and increase with the increase of frequency. In the last model, the interface is placed at $\frac{\lambda}{8}$ down from the surface, as shown in Figure 5.7d. The direct P and S wave arrivals can be observed in the shot record of Figure 5.8d. The Rayleigh wave does not change the phase in this case, and most of the energy is traveling in the dipper layer of the medium. The phase velocities are almost constant with the increase of frequencies in the dispersion curve, of Figure 5.9d. The frequencies in the dispersion curve travel with the velocity of the dipper layer i.e. with the velocity of the softer layer.

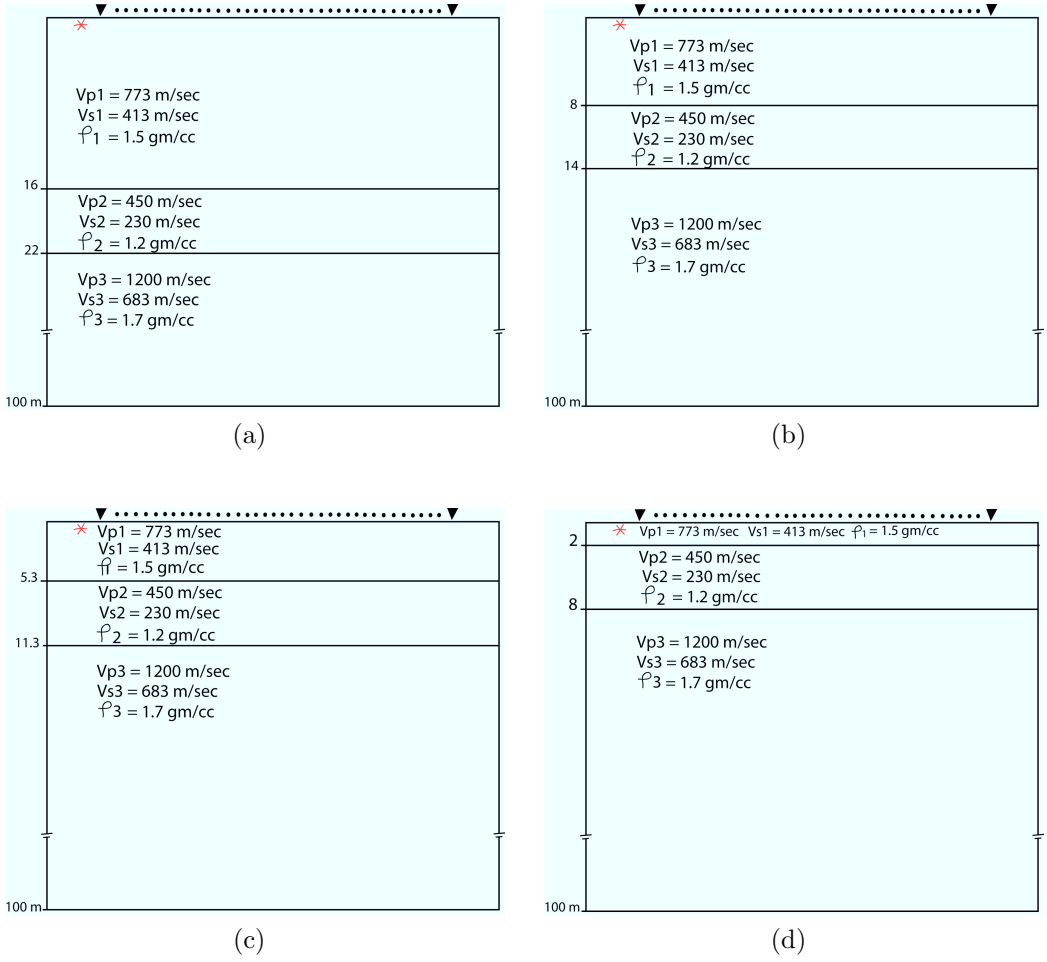

Figure 5.7: The velocity models for the interface placed at (a) λ, (b) $\frac{\lambda}{2}$, (c) $\frac{\lambda}{3}$, and (d) $\frac{\lambda}{8}$ for the alternate velocity layer.

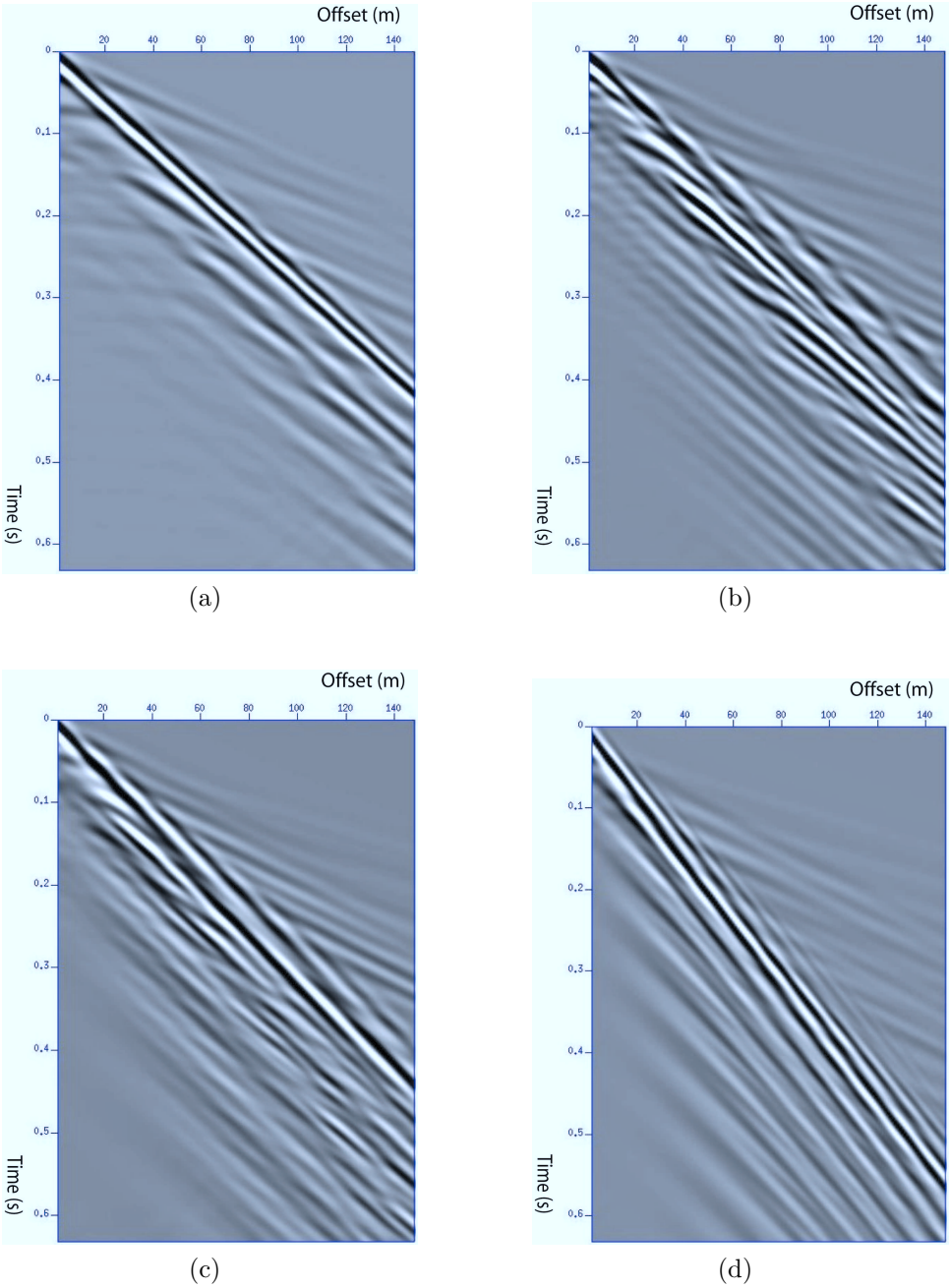

Figure 5.8: Synthetic seismograms for the interface placed at (a) λ, (b) $\frac{\lambda}{2}$, (c) $\frac{\lambda}{3}$, and (d) $\frac{\lambda}{8}$ for the alternate velocity layer. More trapped energies are observed in the seismograms when the interface is placed in between $\frac{\lambda}{2}$ and $\frac{\lambda}{3}$.

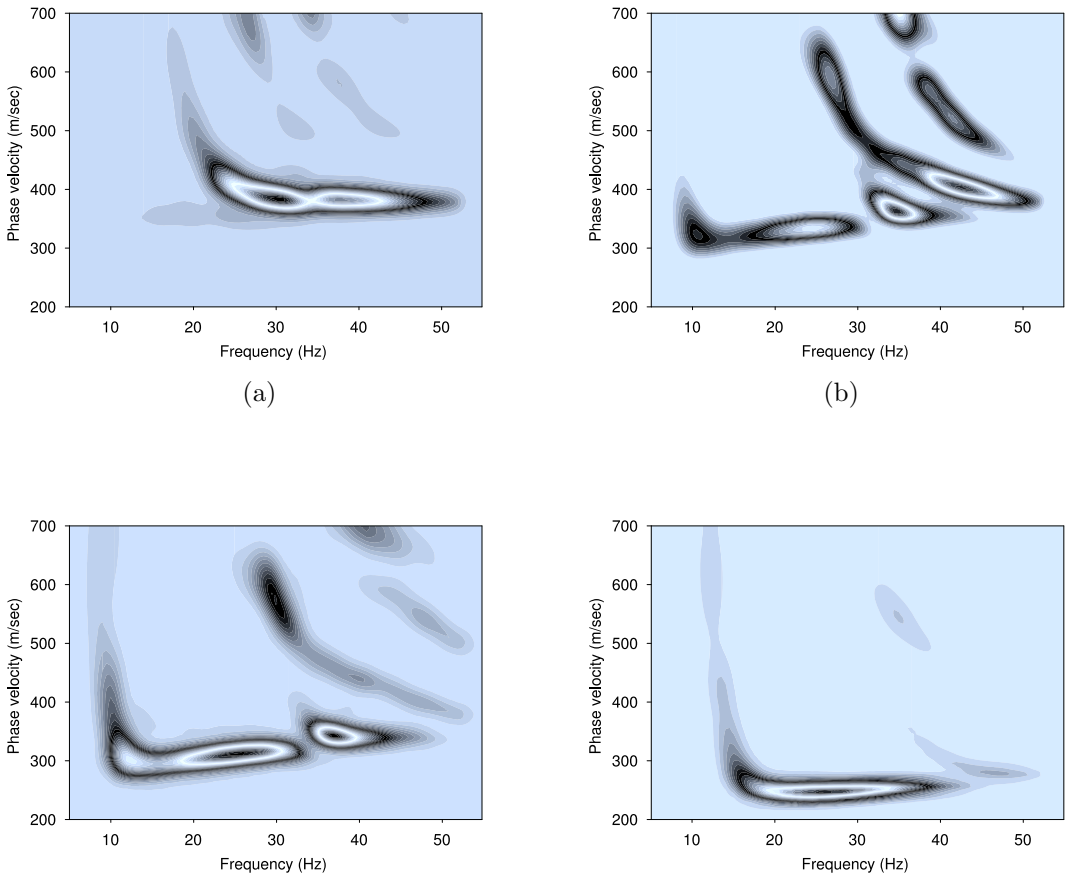

Figure 5.9: Dispersion curves for the interface placed at (a) λ, (b) $\frac{\lambda}{2}$, (c) $\frac{\lambda}{3}$, and (d) $\frac{\lambda}{8}$ for the alternate velocity layer. Missing amplitudes are observed at certain frequency band in the dispersion curves depending on the depth of the low velocity layer.

5.6 The Effect of Layer Dip on Rayleigh Wave Propagation

The presence of a dipping layer in the subsurface can invalidate the assumption of flat layer while calculating the S wave velocity profile through inversion of Rayleigh wave dispersion curves. In order to avoid the difficulty of the flat layers assumption, multichannel synthetic data are divided into 2^n levels, where $n = 0, ..., N$. Each level consists of 2^n panels with sequences of traces in each panel. A dispersion curve for each panel is computed using the slant stack technique. This new and innovative panelizing idea is used to conduct a parametric study to evaluate the reliability of the flat layer assumption in calculating dispersion curves for steeply dipping layered media. There are four cases to be studied:

- model with no dip
- model with 5° dip
- model with 10° dip
- model with 20° dip

There are one, four, and eight levels in each case. The first level consists of all 148 traces in each panel. The fourth level has 37 traces in each panel, and the eighth level has 18 traces in each panel.

5.6.1 Reference Model

A flat layer model, of size 200 meters by 100 meters, is considered as a reference model, and is shown in Figure 5.10. The number of grid points along the x and z axes are 400 and 200, respectively, with a 0.5 meter grid spacing. The source is placed at 21 meters along the x axis direction for the front shot. The first receiver is placed 5 meters away from the source, and the remaining 148 receivers are placed 1 meter away from each other. Similarly, the source is placed at 179 meters in the model for the back shot, keeping the receivers in the same locations. The time step used to compute the synthetic seismogram is 4000 with a sampling time of 0.0002 seconds. The interface is placed 5.3 meters down from the surface, which is one-third of the

minimum wavelength of the Rayleigh wave. Two synthetic seismograms computed using front and back shots in the above model are shown in Figure 5.11. The Rayleigh waves dispersion is clearly visible in both shot records along with the P and S wave arrivals. Both seismograms have a similar appearance.

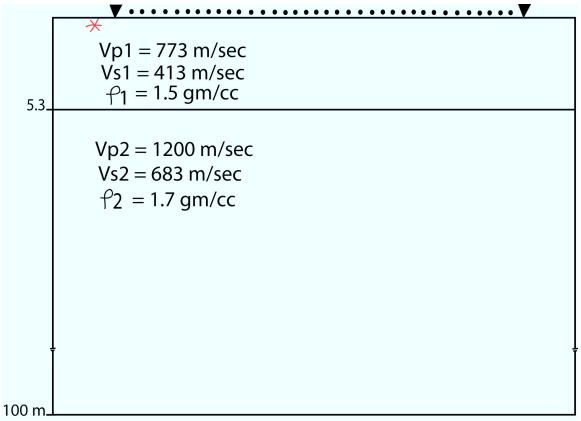

Figure 5.10: 2-D finite difference model for the flat layer.

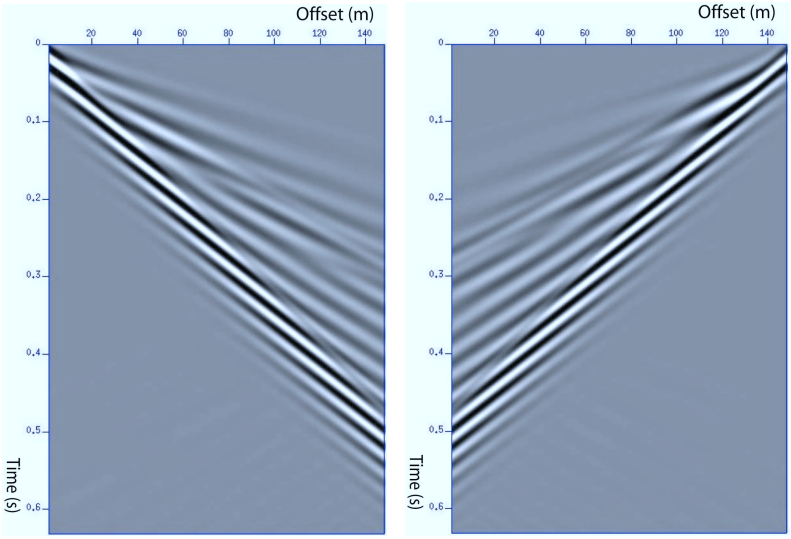

Figure 5.11: Front shot record (left) and back shot record (right) for the flat layer model. The Rayleigh waves dispersion is clearly seen in both shot records.

Figure 5.12 shows the dispersion curves of the flat layer model for the front and back shots in level one. It can be observed that these two dispersion curves match each other. Dispersion curves for the fourth level for the front and back shots are given in Figure 5.13. The amplitudes in the corresponding panels map in same location in the phase-velocity frequency domain. Figure 5.14 and Figure 5.15 show eight levels

of the front and back shots, respectively. Comparing the corresponding panels for the both shots, it can be seen that the energy allocation in the frequency velocity domain remains almost the same. In the flat layer model, Rayleigh waves propagate horizontally in equal amounts in both media, from the first to the last receiver, in the front and back shots.

5.6.2 Case 1: Synthetic Model with 5° Dip

The model with 5° dip is shown in Figure 5.28. Two synthetic seismograms from the front and back shots are given in Figure 5.29. Rayleigh waves dispersion is observed in near offsets for down dip for the front shot, and is evident in far offsets for the up dip for the back shot. Dispersion curves are computed for the front and back shots for the first, fourth, and eighth levels. The dispersion curve in the first level is shown in Figure 5.18. The phase velocity versus the frequency in the dispersion curves is not resolved very well in this level. The dispersion curve for the front and back shots in level four is represented in Figure 5.19. It can be observed that the Rayleigh waves travel more in the high velocity region in extreme up dip, and gradually travel to the low velocity region in the down dip. The phase velocity axis is resolved well after panelizing the first level into sequences of traces. Figure 5.20 and Figure 5.21 are dispersion curves for level eight for the front and back shots respectively. The lateral resolution has been reduced in this level because there are fewer traces in each panel. The phase velocity of the Rayleigh waves traveling in the the different regions, from up dip to down dip is more evident.

5.6.3 Case 2: Synthetic Model with 10° Dip

The dip is increased to 10° as shown in Figure 5.22. The front and back shot computed from this model are shown in Figure 5.23. The direct P and S wave arrivals can be seen in the front and back shot records. The Rayleigh wave dispersion is reduced as the dip in the layers is increased. A very small amount of Rayleigh waves phase change is observed in extreme up dip in the front shot record and in the down dip in the back shot record. Dispersion curves for level one, four and eight levels were also computed for a 10° dip. As shown in Figure 5.24, the phase velocity is not

resolved well in the dispersion curve for level one. In Figure 5.25, it can be observed that the change in phase velocity in the different regions are resolved well in level four. The dispersion curves computed from the front and back shot records for the level four show that the phase velocity of the Rayleigh waves decrease from panel one to panel four, i.e. most of the frequencies of Rayleigh waves travel in the high velocity region in the up dip, and in the low velocity region in the down dip. The level eight dispersion curves for the front and back shots are shown in Figure 5.26 and Figure 5.27, respectively. Lateral resolution is reduced in this level because there are fewer traces, but the phase velocity in the front and back shots is more resolved than it is in level four.

5.6.4 Case 3: Synthetic Model with 20° Dip

The dispersion curves for levels one, four and eight were also computed for a 20° dip. For a 20° dip model, dispersion is not evident until the panel width is reduced to 18 meters. This results from the fact that most of the Rayleigh wave energy is propagated in the upper low velocity layer, within the region where the lower layer is within one-third of the wavelength of the Rayleigh wave.

5.7 Results Summary for the Influence of Layer Depth and Dip on Rayleigh Wave Propagation

- The phase velocity of Rayleigh wave decrease or increase with increase of frequency when velocity increases or decrease with depth. High dispersion is observed when interface is placed in between $\frac{\lambda}{2}$ to $\frac{\lambda}{3}$ of minimum wavelength of Rayleigh wave.

- The phase velocity of Rayleigh wave remain constant with increase of frequency when interface depth is more than a wavelength or less than $\frac{\lambda}{8}$ of minimum Rayeligh wave wavelength. Rayleigh wave travels with the velocity of upper layer when interface is at a minimum Rayleigh wave wavelength and travels at velocity of deeper layer when interface is at $\frac{\lambda}{8}$ of minimum wavelength of Rayleigh wave.

- The synthetic seismograms computed from the front and back shots are different from each other when the subsurface contains dipping layers.
- Dispersion is observed in the near offset for down dip and in the far offset for up-dip, computed from the front and back shots, respectively.
- Computing dispersion curves in panels helps to resolve velocity distributions in the lateral direction.

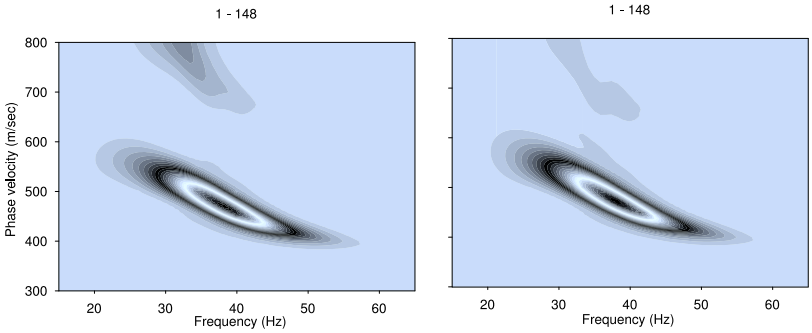

Figure 5.12: Dispersion curves for the front shot (left) and the back shot (right) for level one.

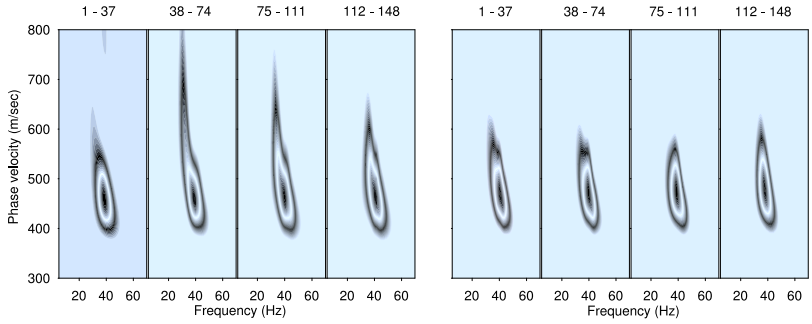

Figure 5.13: Dispersion curves for the front shot (left) and the back shot (right) for level four.

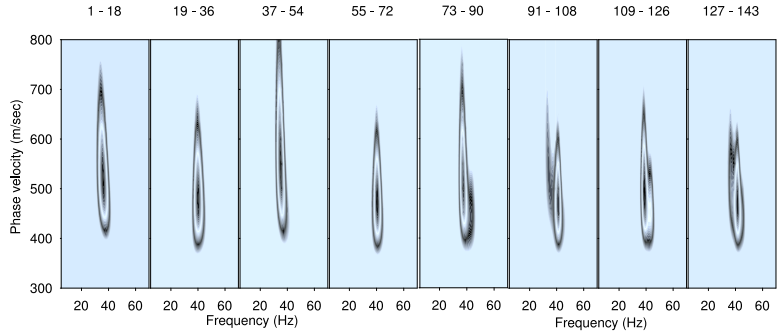

Figure 5.14: Dispersion curves for the front shot for level eight.

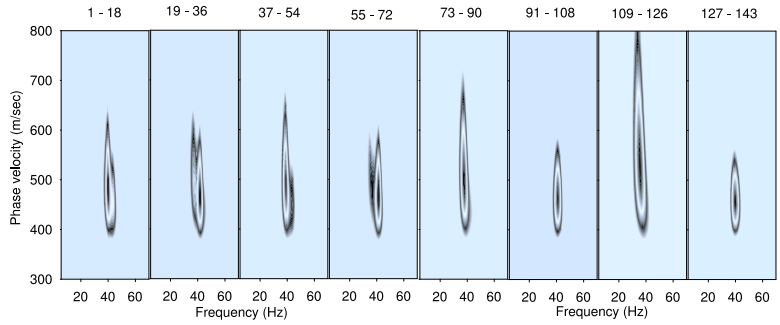

Figure 5.15: Dispersion curves for the back shot for level eight.

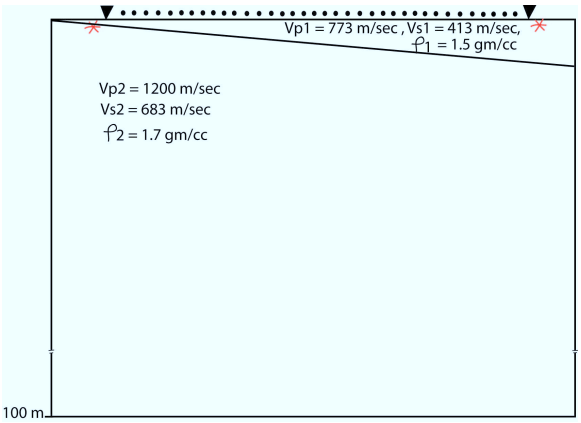

Figure 5.16: 2-D finite difference model for 5° dip.

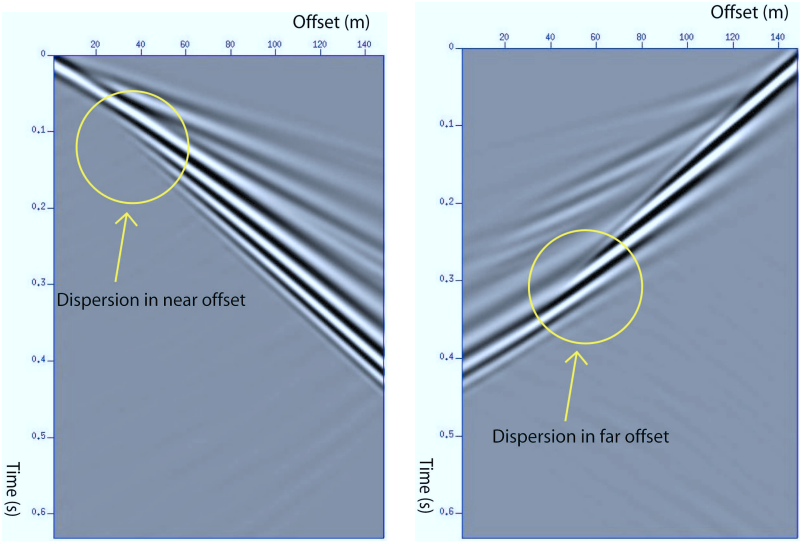

Figure 5.17: The Front shot record (left) and the back shot record (right) for the 5° dipping layer model. Rayleigh waves dispersion is seen in near offsets for the front shot and in far offsets for the back shot record.

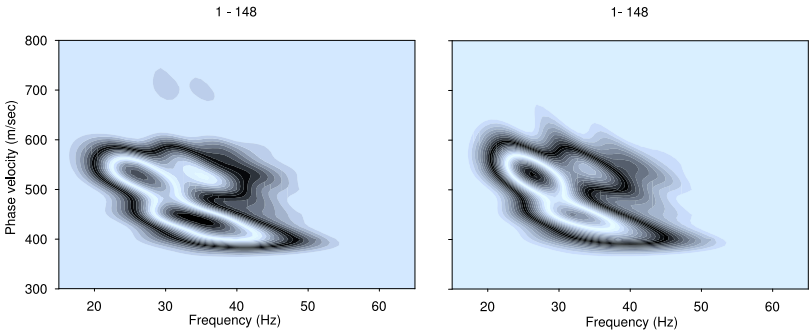

Figure 5.18: Dispersion curves for the front shot (left) and the back shot (right) for level one in the 5° dipping layer model.

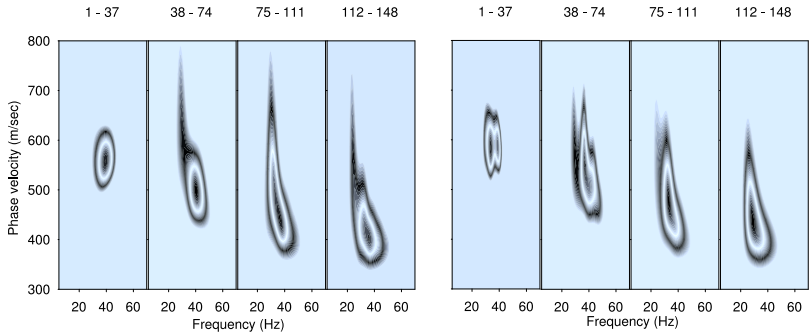

Figure 5.19: Dispersion curves for front shot (left) and the back shot (right) for level four in the 5° dipping layer model.

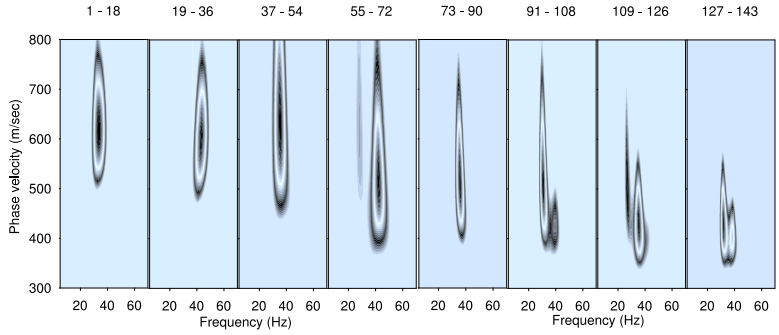

Figure 5.20: Dispersion curves for the front shot in level eight in the 5° dipping layer model.

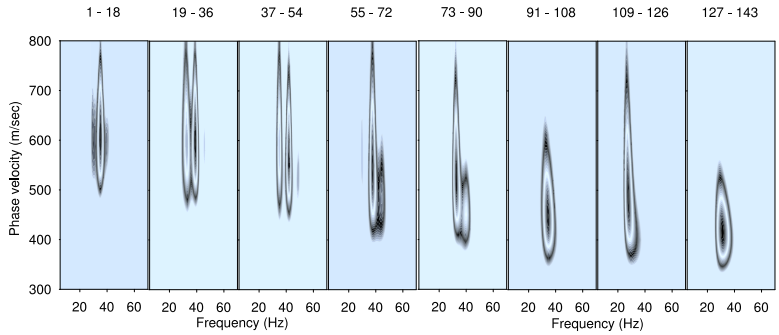

Figure 5.21: Dispersion curves for the back shot in level eight in the 5° dipping layer model.

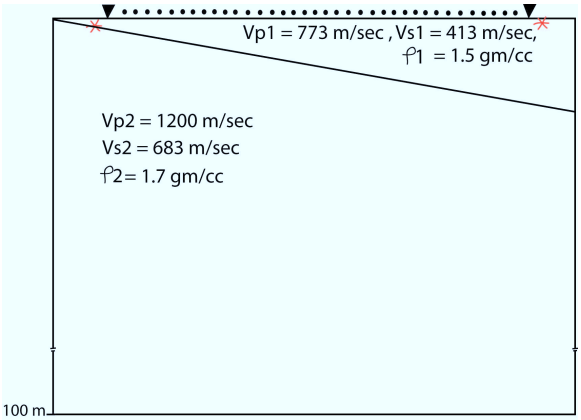

Figure 5.22: 2-D finite difference model for 10° dip.

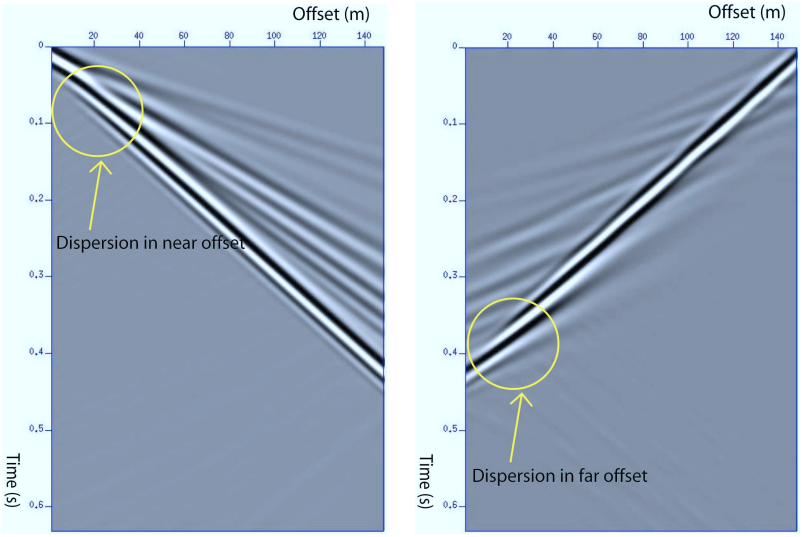

Figure 5.23: Front shot record (left) and the back shot record (right) for the 10° dipping layer model.

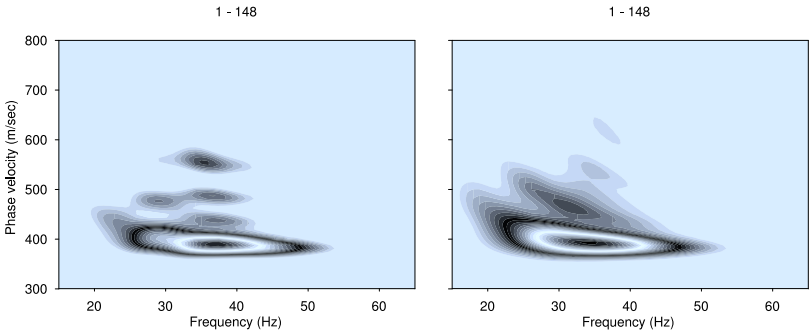

Figure 5.24: Dispersion curves for the front shot (left) and the back shot (right) for level one in the 10° dipping layer model.

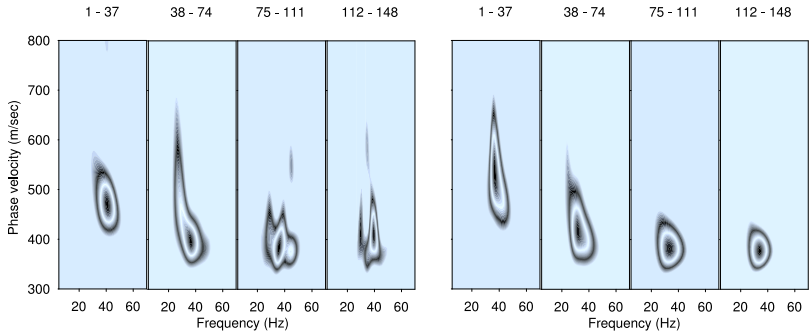

Figure 5.25: Dispersion curves for the front shot (left) and the back shot (right) for level four in the 10° dipping layer model.

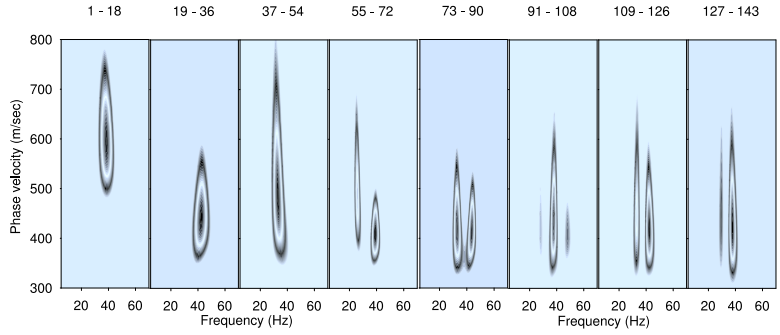

Figure 5.26: Dispersion curves for the front shot in level eight in the 10° dipping layer model.

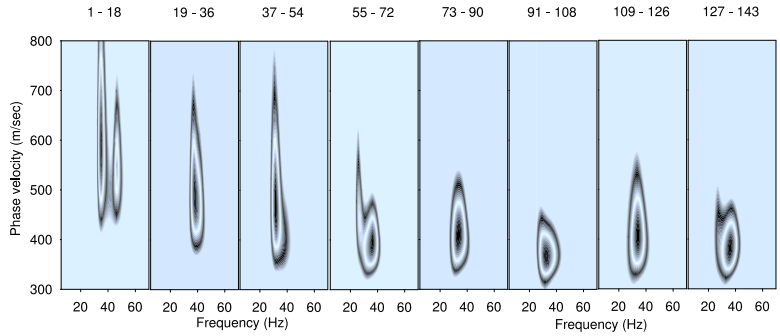

Figure 5.27: Dispersion curves for the front shot in level eight in the 10° dipping layer model.

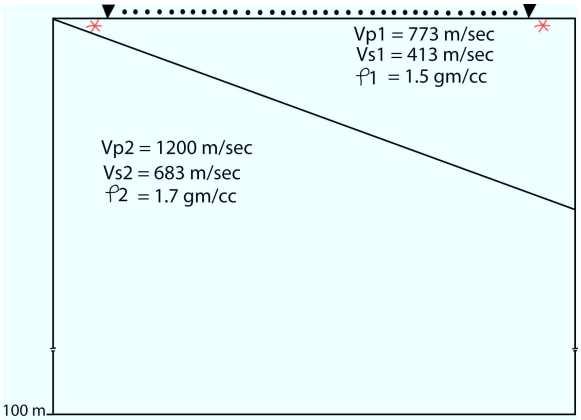

Figure 5.28: 2-D finite difference model for the 20° dip.

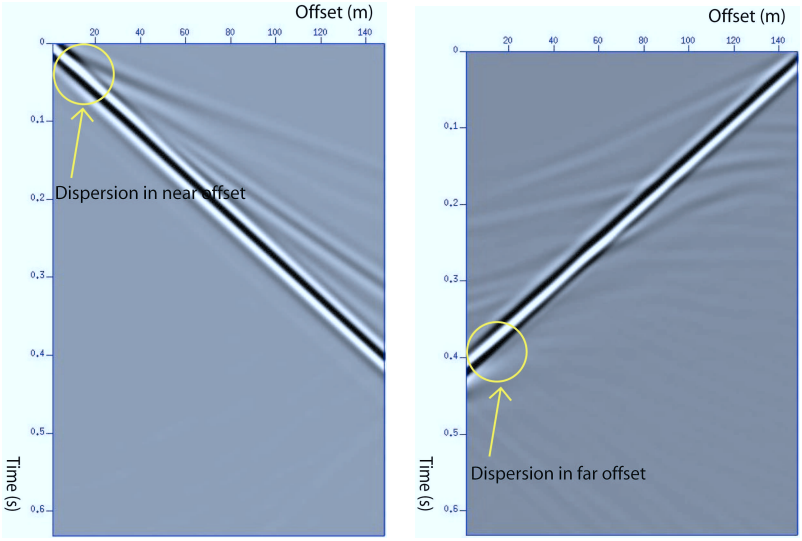

Figure 5.29: The Front shot record (left) and the back shot record (right) for the 20° dipping layer model.

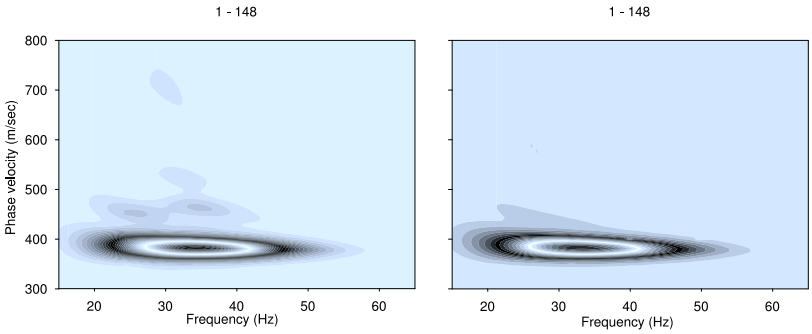

Figure 5.30: Dispersion curves for the front shot (left) and the back shot (right) for level one in the 20° dipping layer model.

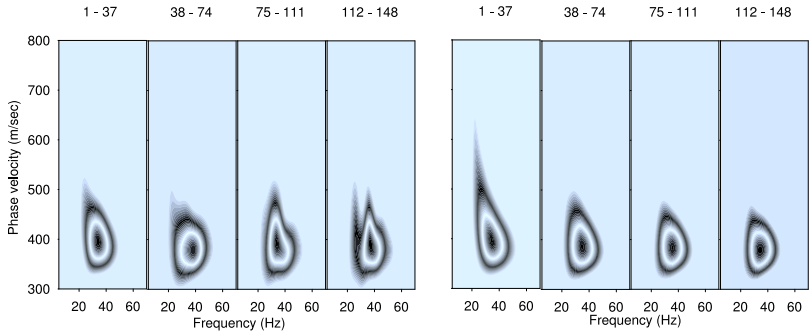

Figure 5.31: Dispersion curves for the front shot (left) and the back shot (right) for level four in the 20° dipping layer model.

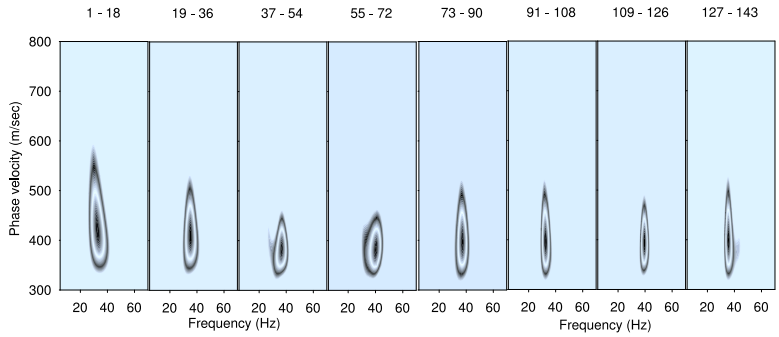

Figure 5.32: Dispersion curves for front the shot in level eight in the 20° dipping layer model.

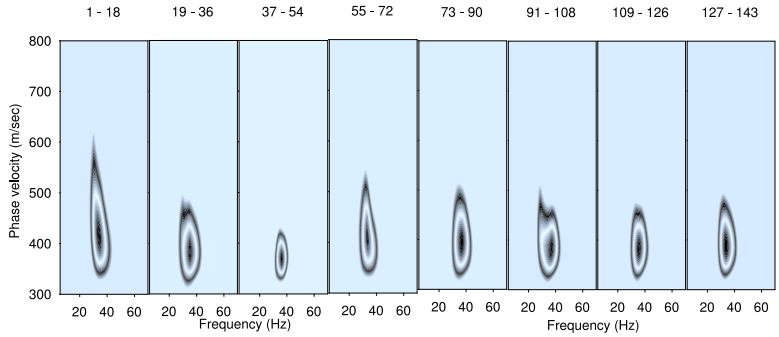

Figure 5.33: Dispersion curves for the back shot in level eight in the 20° dipping layer model.

Chapter 6

Influence of a Localized Anomaly on the Propagation of Rayleigh Waves

6.1 Overview

The presence of a near surface anomaly introduces lateral heterogeneity in a sub-surface. Rayleigh wave propagation is sensitive to the various parameters associated with a near surface anomaly, specifically size, shape and the material properties of the anomaly. A parametric study has been conducted in order to investigate the effect of each parameter associated with an anomaly on the Rayleigh waves dispersion curves. A 2-D finite difference staggered grid modeling code, as discussed in Chapter 3, is adapted for this parametric study. Dispersion curves are computed using the slant stack technique.

6.2 The Effect of Material Contrast of a Rectangular Anomaly from Its Surrounding Medium on Rayleigh Waves Dispersion Curves

The presence of a near surface anomaly disrupts the Rayleigh wave propagation which can be studied in changes to Rayleigh wave dispersion curves. This effect varies with the material contrast of the anomaly from its surroundings. In order to investigate the effect of material contrast, a parametric study is carried out by decreasing the material contrast of the anomaly from +75% to -75% of the reference case. Two types of anomalies are considered in this study, rectangular and circular. Both of the anomalies are 98 square meters in area, and are 5 meters or $\frac{\lambda}{3}$ below the surface. The numerical models and source receiver geometry for this parametric study are same as described in chapter 3. The elastic parameters used in this parametric study are given in Table 6.1.

Percentage(%)	E(GPa)	Poission Ratio	ρ(g/cc)	Vp(m/s)	Vs(m/s)
+75	52.5	0.15	3.1	4115.0	2640.0
+50	45.0	0.20	2.9	3939.0	2412.0
+25	37.5	0.25	2.7	3727.0	2152.0
+0	30.0	0.30	2.5	3464.0	1851.0
-25	22.5	0.35	2.3	3128.0	1503.0
-50	15.0	0.40	2.1	2673.0	1091.0
-75	7.5	0.45	1.9	1987.0	599.0

Table 6.1: The elastic parameters used to investigate the effect of material contrast of a near surface anomaly.

6.2.1 Anomaly with Increasing Material Contrast

The shot record for the reference model is shown in Figure 6.1d. The shot records for the models with the rectangular anomaly and +75%, +50% and +25% material contrast from the surrounding medium are represented in Figure 6.1a, Figure 6.1b and Figure 6.1c, respectively. The direct P wave travels faster than S wave. The converted S wave from P wave can also be seen in each shot record. Since the surrounding medium is homogeneous, the S wave and Rayleigh wave travel with the same speed until they hit the anomaly. Both S and the Rayleigh waves are reflected back as soon as they hit the anomaly. It can be observed that as the material contrast of the anomaly increases from +25% to +75% of its surrounding medium, the reflection of the P wave, S wave and the Rayleigh waves become stronger from the side of the anomaly. The slant stack method is used to compute the Rayleigh waves dispersion curves. Since there are positive and negative slopes of velocity due to the direct waves and reflected waves in each shot record, the dispersion curves are computed by stacking the velocity for both slopes in the slant stack. The positive and negative dispersion curves for the reference case are shown in Figure 6.2g and Figure 6.2h respectively. Since a Rayleigh wave is not dispersive in a homogeneous medium, phase velocity in the positive dispersion curve remains constant with an increase of frequency in the reference case. The negative dispersion curve has almost no energy along the phase velocity frequency axis. When the material contrast of the anomaly

increases from its surroundings from +25% to +75%, the positive dispersion curves remain the same in all cases. All frequencies travel with same phase velocity, as shown in Figure 6.2e, Figure 6.2c and Figure 6.2a, respectively. It can be observed that the reflected energy from the side of the anomaly is evident in the negative dispersion curve. The amplitudes of the energy in the negative dispersion curves increase when the material contrast of the anomaly increases from +25% to +75%. This is shown in Figure 6.2f, Figure 6.2d, and Figure 6.2b, respectively.

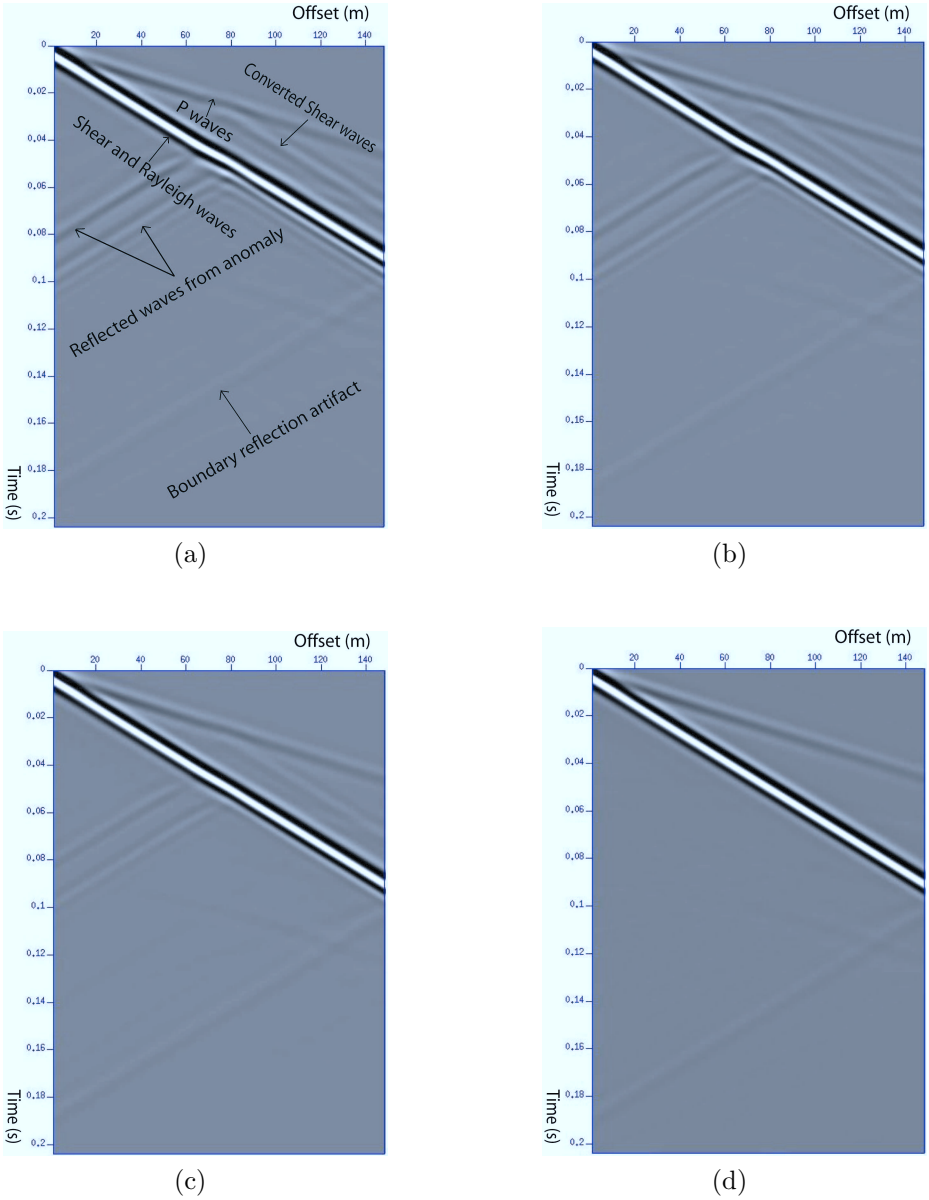

Figure 6.1: The shot records of the material contrast at (a)+75%, (b)+50%, (c)+25%, and (d)+0% for the rectangular anomaly. Reflected energy increases when the material contrast increases from +0% to +75%.

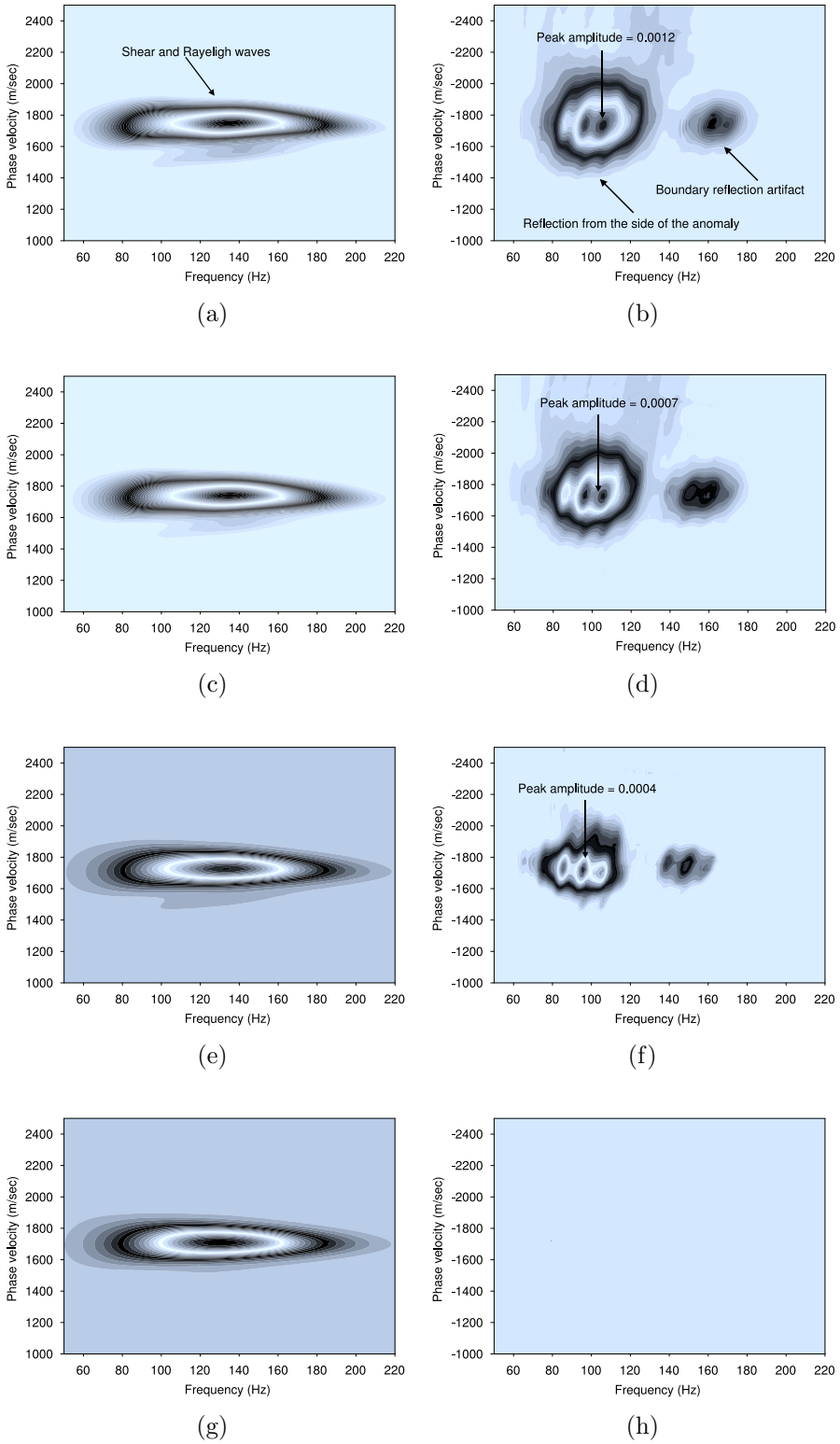

Figure 6.2: Positive dispersion curves represented in (a), (c), (e), and (g) and the negative dispersion curves are shown in (b), (d), (f), and (h). Phase velocity is constant in the positive dispersion curves, whereas, in the negative dispersion curves, amplitudes increase with the increase of material contrast from +25% to +75%.

6.2.2 Anomaly with Decreasing Material Contrast

The parametric study of the material contrast of the rectangular anomaly is continued by decreasing the material contrast of the anomaly from the surrounding medium -25% to -75%. The shot record of the reference case is shown in Figure 6.3a, and the shot records of the -25%, -50% and -75% material contrast are given in Figure 6.3b, Figure 6.3c and Figure 6.3d, respectively. Direct P and S waves and Rayleigh waves can be seen in each shot record. All these direct waves reflect back after they hit the anomaly. The converted S wave also can be seen in each shot record after hit the anomaly. It can be observed that as the material contrast decreases from -25% to -75%, the energy trapped inside the anomaly and causes reverberation. The trapped energy can be clearly seen in the shot record of Figure 6.3d. The dispersion curves for the shot records of the decreasing material contrast are computed for both positive and negative slopes. The positive and negative dispersion curves for the reference case are shown in Figure 6.4a and Figure 6.4b, respectively. As the material contrast decreases from -25% to -75%, the amplitudes in the positive dispersion curves attenuate at a particular frequency band. This is shown in Figure 6.4g. It is also observed that the higher mode of Rayleigh waves becomes stronger with the decreasing material contrast of the anomaly. The absence of Rayleigh wave energy in particular regions of the frequency band is an indication of the depth of an anomaly. The strong presence of reflected energy from the front and rear faces of the anomaly is observed in the negative dispersion curves of Figure 6.4d, Figure 6.4f, and Figure 6.4h.

6.3 The Effect of Material Contrast of a Circular Anomaly from Its Surrounding Medium on the Rayleigh Waves Dispersion Curve

The parametric study of material contrast of the circular anomaly from the surrounding medium is conducted using exactly the same parameters which were used

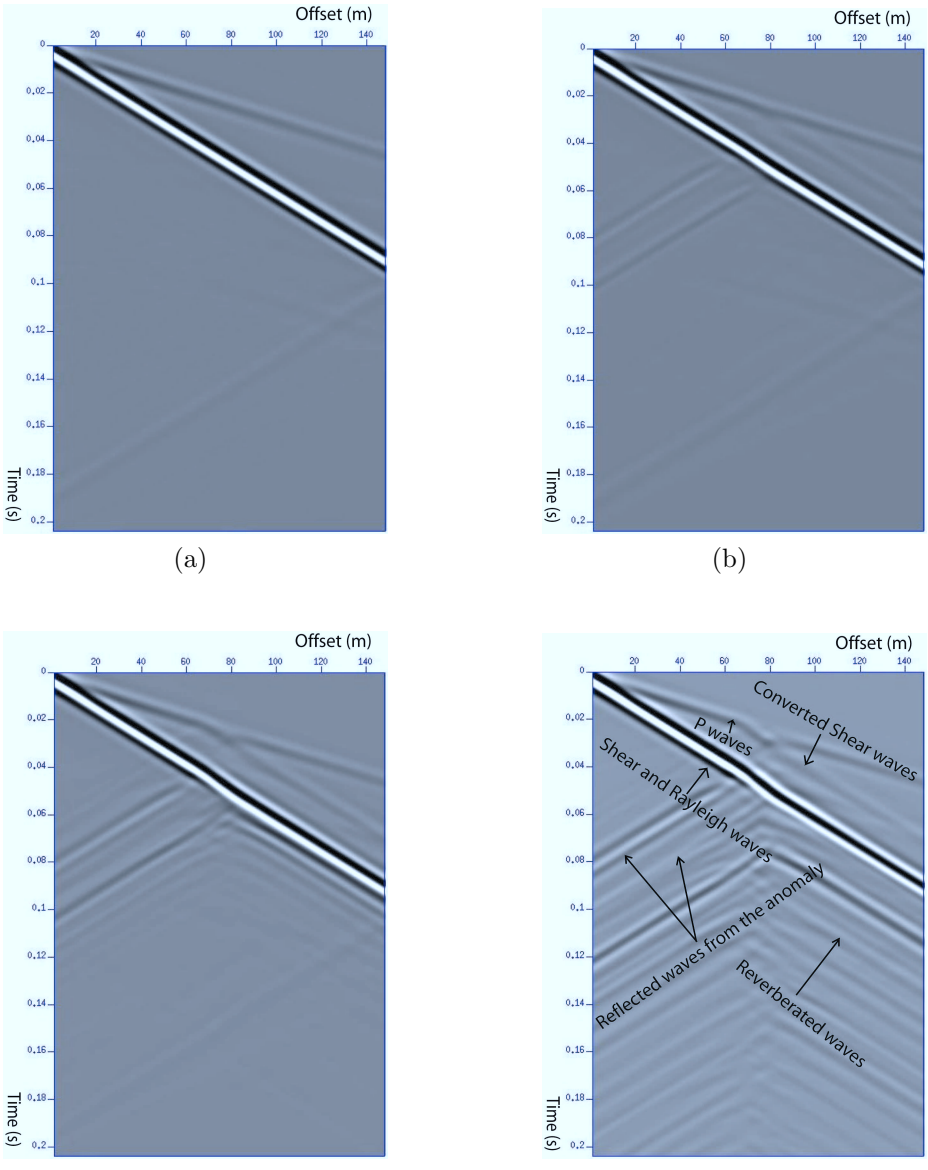

Figure 6.3: The shot records of the material contrast at (a)0%, (b)-25%, (c)-50% and (d)-75% for the rectangular anomaly. Trapped energy inside the anomaly increases as the material contrast of the anomaly from its surroundings decreases.

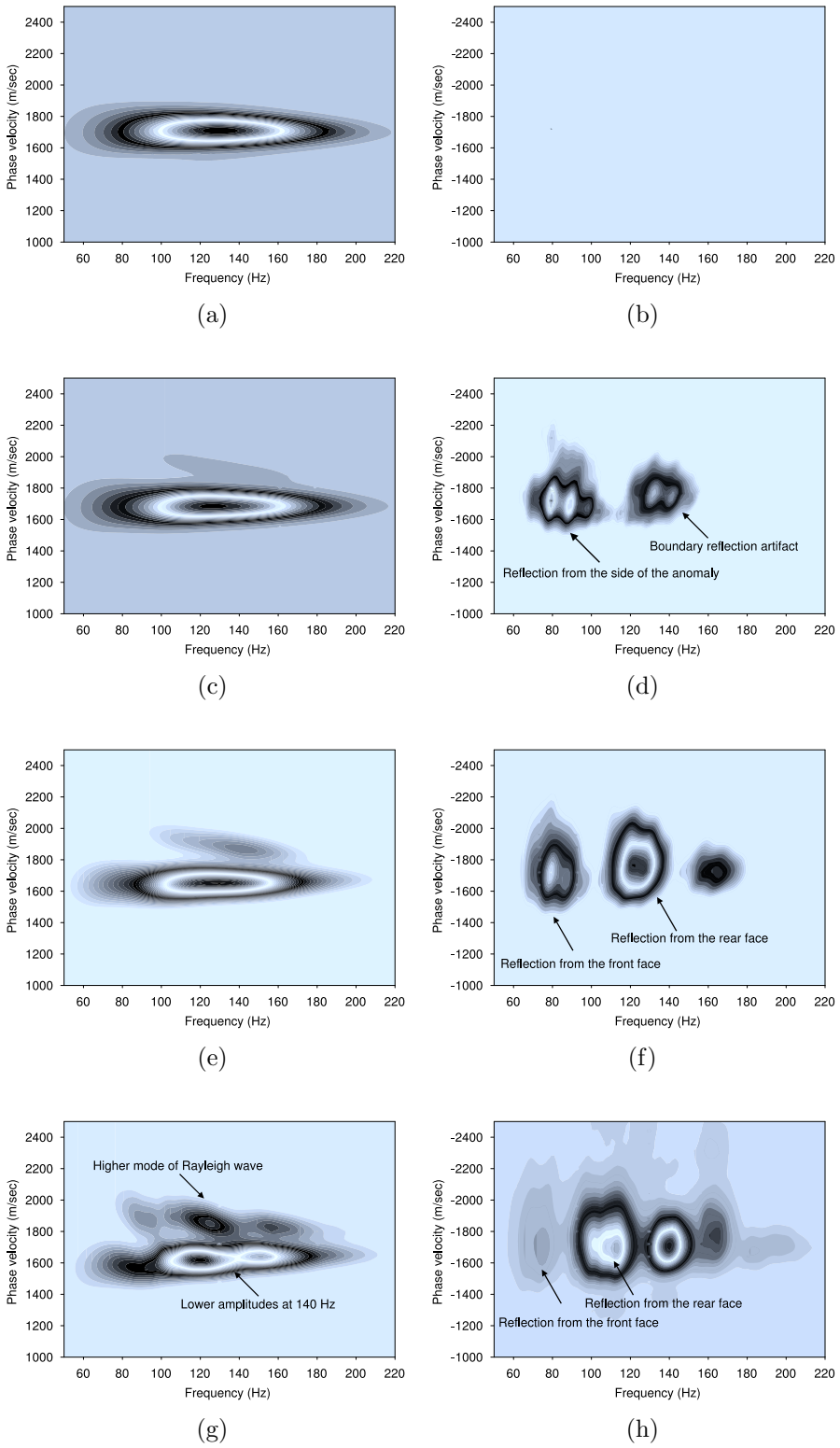

Figure 6.4: The positive dispersion curves are represented in (a), (c), (e), and (g). The negative dispersion curves are shown in (b), (d), (f), and (h). The Rayleigh wave energy attenuated at a particular frequency, as shown in the positive dispersion curve of -75% material contrast.

to study the material contrast of the rectangular anomaly. When the corresponding shot records and dispersion curves of the rectangular and circular anomalies are compared the only difference observed is that, the reflected wave from the circular anomaly is more curved and less linear. This is because the circular anomaly does not have sharp corners as does the rectangular anomaly. The shot records of the material contrast at +75% is shown in Figure 6.5a. Direct arrival of P wave, S wave and Rayleigh waves is seen in the shot record as well as the converted S wave. Smooth reflection from the anomaly is also seen. Figure 6.5b represents the shot record of the circular anomaly at -75% material contrast. Direct arrival of P, S and Rayleigh waves are observed, and reverberated trapped energy inside the anomaly is also seen in the shot record. The positive and negative dispersion curves for +75% material contrast is given in Figure 6.6a and Figure 6.6b, respectively. Phase velocity in the positive dispersion curve remains constant with the increase in frequency. Strong reflected energy is seen in the negative dispersion curve at +75% material contrast. The positive dispersion curve for -75% material contrast is given in Figure 6.6c. Energy attenuated at a particular frequency in the dispersion curve is related to the depth of the anomaly. Refection from the outer and inner circle is observed in the negative dispersion curve of Figure 6.6d for -75% material contrast.

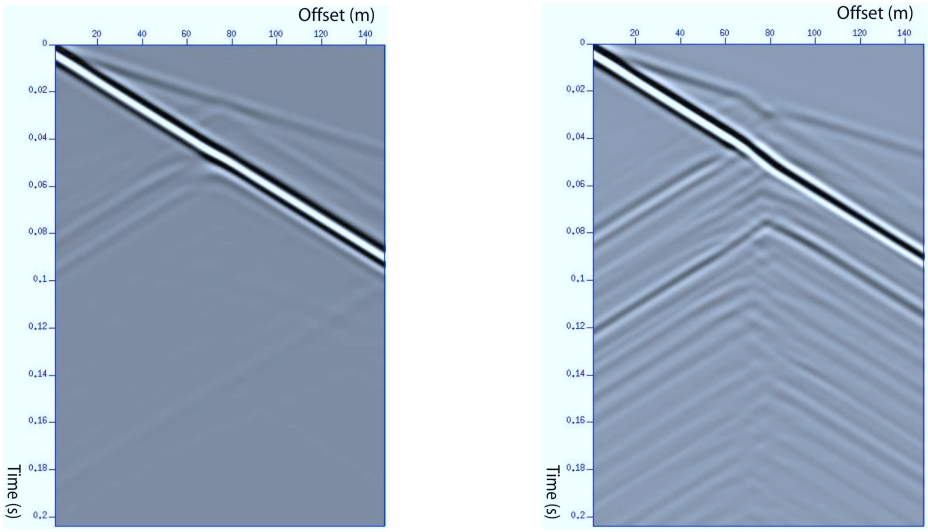

(a) (b)

Figure 6.5: The shot records of material contrast (a)+75%, (b)-75% for the circular anomaly

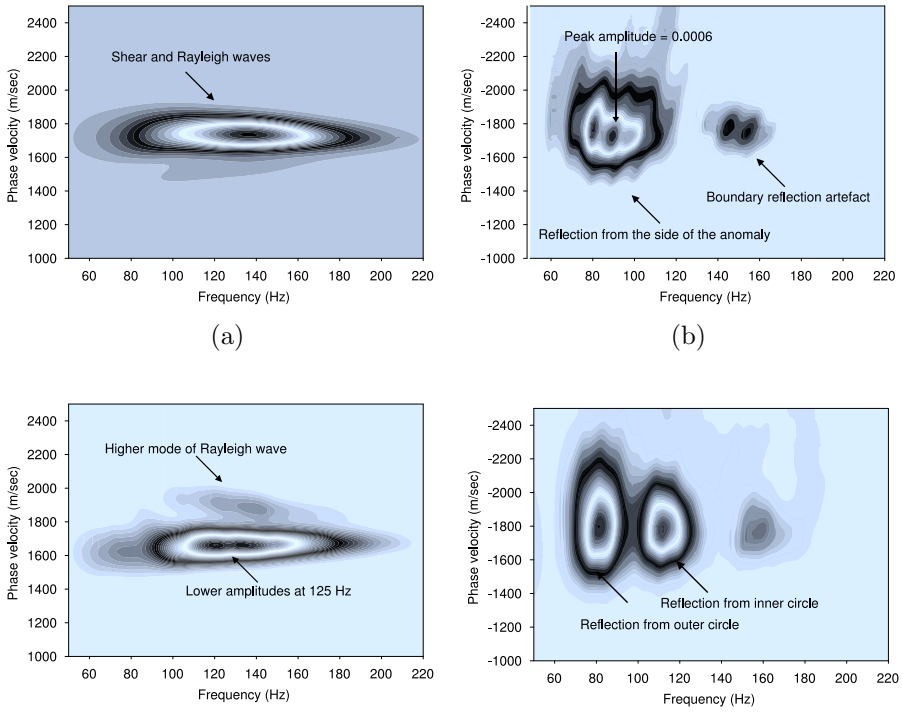

(a) (b)

(c) (d)

Figure 6.6: The positive dispersion curves are represented in (a), (c), (e), (g). The negative dispersion curves are shown in (b), (d), (f), (h). Reflection from the circular anomaly is smoother than that from the rectangular anomaly.

6.4 Results Summary of the Effect of Material Contrast of an Anomaly on Rayleigh Waves

- Reflection of P, S and Rayleigh waves from the side of an anomaly increases when the material contrast of the anomaly increases from +25% to +75% from the surrounding medium. This may be seen in Figure 6.1c, Figure 6.1b and Figure 6.1a

- Positive dispersion curves of Rayleigh waves remain constant with increase of frequency, when the material contrast of the anomaly increases. This is shown in Figure 6.2e, Figure 6.2c and Figure 6.2a. The amplitudes of the reflected energy in the negative dispersion curves increase with the increase of material contrast. This is seen in Figure 6.2f, Figure 6.2d and Figure 6.2b.

- The anomaly traps energy and causes reverberation when its material contrast decreases from the surrounding medium. Reverberation of the trapped energy can be seen in the shot record of Figure 6.3d, which is computed from the model with an anomaly of -25% material contrast.

- As the material contrast of an anomaly decreases from -25% to -75% of the surrounding medium, energy attenuated at a particular frequency band in the positive dispersion curves is related to the depth of the anomaly. Figure 6.4g represents the positive dispersion curve computed from the model with an anomaly at -75% material contrast. Energy is attenuated at 140 Hz with a velocity of 1600 m/s. Hence, the wavelength, λ =11.4 meters. This approximates the depth of the anomaly as 5 meters which matches the original depth of the anomaly from the surface. Reflection from the front and rear faces is seen in the negative dispersion curves of Figure 6.4f and Figure 6.4h. The width or radius of an anomaly can be determined by computing the wavelengths of the reflected waves from the front and rear faces. From the dispersion curve of Figure 6.4f, the wavelength, λ_1 of reflected waves from front face at frequency 80 Hz with velocity 1700 m/s is 21.25 meter. The wavelength, λ_2, of the reflected wave from the rear face, at a frequency of 125 Hz and a velocity of 1770 m/s, is 14.2

meters. Hence, the width of the rectangular anomaly at -50% material contrast is given by $\lambda_1 - \lambda_2 \approx 7$ meters. This matches the original width of the anomaly. Similarly, the width or radius of the anomaly at -25% material contrast can be computed.

- A Rayleigh wave is more sensitive to the anomaly when the material contrast is at +75% and -75%.

6.5 Effect of the Depth of a Rectangular Versus a Circular Anomaly on the Rayleigh Waves Dispersion Curves

The parametric study of the effect of material contrast of a rectangular versus a circular anomaly from their surrounding media on the Rayleigh wave dispersion curves was discussed in the previous section. It was observed that a Rayleigh wave dispersion curve is more sensitive to +75% and -75% of the material contrast from the surrounding medium. Therefore, +75% and -75% of the material contrast were selected to study the effect of depth of a rectangular versus a circular anomaly on Rayleigh waves dispersion curves. Each of the anomalies is placed incrementally at the depth between 4 ($\approx \frac{\lambda}{5}$) and 19 ($\approx \lambda$) meters from the surface, at 3 meters increment, and dispersion curves were computed at each depth. The remaining parameters were kept constant.

6.5.1 Effect of the Depth of a Rectangular Anomaly at +75% Material Contrast

The shot records computed for the models with a rectangular anomaly at +75% material contrast from their surroundings, at depths of 4 ($\approx \frac{\lambda}{5}$), 7 ($\approx \frac{\lambda}{4}$), 10 ($\approx \frac{\lambda}{2}$), and 19 ($\approx \lambda$) meters from the surface, are represented in Figure 6.7a, Figure 6.7b, Figure 6.7c, and Figure 6.7d, respectively. The direct P and S waves can be observed in each shot record. The reflection from the side of the rectangular anomaly decreases as the the depth of the anomaly increases. The strong reflection of P, S and Rayleigh waves are observed in the shot record of Figure 6.7a where the anomaly is placed 4 meters from the surface. In Figure 6.7d, where the anomaly is placed 19 meters from

the surface, there is almost no reflection in the shot record. The positive dispersion curves computed for the above shot records, in which the anomalies are placed at $\approx \frac{\lambda}{5}$, $\approx \frac{\lambda}{4}$, $\approx \frac{\lambda}{2}$, and $\approx \lambda$ meters depth, are shown in Figure 6.8a, Figure 6.8c, Figure 6.8e, and Figure 6.8g, respectively. The phase velocity in the positive dispersion curves are constant in each plot. Similarly the negative dispersion curves are shown in Figure 6.8b, Figure 6.8d, Figure 6.8f, and Figure 6.8h, respectively. The reflected energy from the side of the anomaly mapped in the negative dispersion curves and with higher amplitudes, when the anomaly is close to the surface, as shown in Figure 6.8b. It is also observed that reflected events mapped in low frequencies in the negative phase velocity dispersion curve, as depth of the anomaly increases from the surface. This confirms that as the depth of the anomaly increases from the surface, low frequencies or long wavelengths are increasingly reflected from the side of the anomaly.

6.5.2 Effect of the Depth of a Rectangular Anomaly at -75% Material Contrast

The parametric study of depth is conducted for a rectangular anomaly at -75% material contrast from its surrounding medium. The shot records computed from the models, introducing a rectangular anomaly at -75% material contrast from its surroundings at a depth of 4 ($\approx \frac{\lambda}{5}$), 7 ($\approx \frac{\lambda}{4}$), 10 ($\approx \frac{\lambda}{2}$), and 19 ($\approx \lambda$) meters are represented in Figure 6.9a, Figure 6.9b, Figure 6.9c, and Figure 6.9d, respectively. The direct P and S waves can be seen in each shot record. The trapped energy which causes reverberation inside the anomaly is also observed. The reflected energy from the side of the anomaly and trapped energy inside the anomaly increase as the anomaly is moved closer to the surface. Therefore, the reflection and trapped energy in the shot record, computed for the model where the anomaly is placed 4 meters from the surface, shown in Figure 6.9a, is greater than the energy where the anomaly is placed 19 meters below the surface, as shown in Figure 6.9d. The positive dispersion curves computed for the above shot records, in which the anomaly is placed at $\approx \frac{\lambda}{5}$, $\approx \frac{\lambda}{4}$, $\approx \frac{\lambda}{2}$, and $\approx \lambda$ meters depth, are shown Figure 6.10a, Figure 6.10c, Figure 6.10e, and Figure 6.10g, respectively. The phase velocity in the positive dispersion

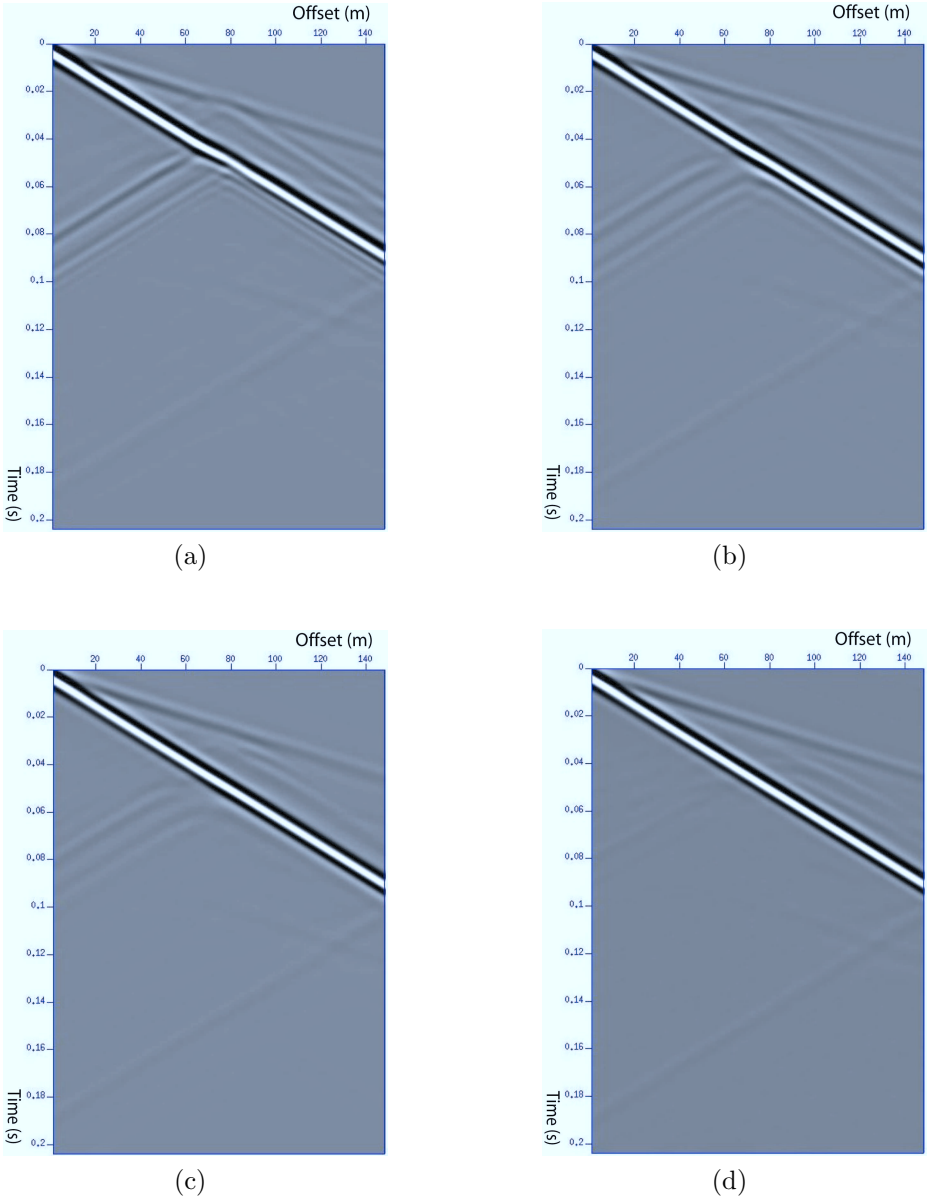

Figure 6.7: The shot records for the rectangular anomaly at +75% material contrast, at (a) 4, (b) 7, (c) 10, and (d) 19 meters from the surface. The reflection from the side of the anomaly becomes weaker as the anomaly is moved deeper below from the surface.

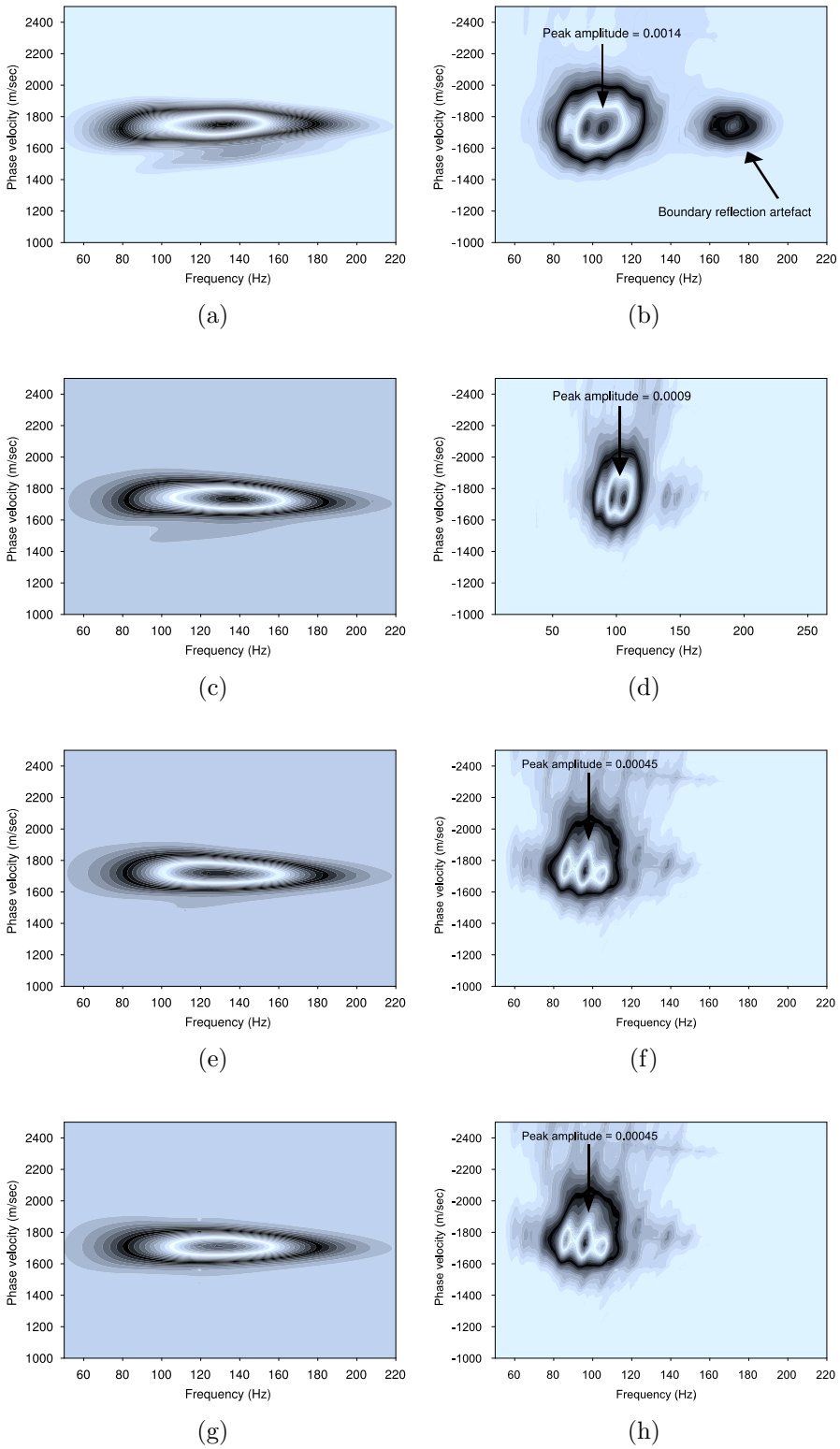

Figure 6.8: The positive dispersion curves are represented in (a), (c), (e), and (g), and the negative dispersion curves are shown in (b), (d), (f), and (h). As the depth of the anomaly from the surface increases, low frequency, which reflects from the side of the anomaly, increases in the negative dispersion curves for the anomalies of +75% material contrast.

curves has amplitude attenuation in a particular frequency band due to the depth of the anomaly. Similarly the negative dispersion curves computed for the above shot records are shown Figure 6.10b, Figure 6.10d, Figure 6.10f, and Figure 6.10h, respectively. The reflected energy from the front and rear faces of the anomaly is mapped in the negative dispersion curve, and the amplitude of the reflected energy is higher when the anomaly is close to the surface. This is shown in Figure 6.10b.

6.6 Results Summary of the Effect of Depth of an Anomaly on Rayleigh Waves

- Reflection from the side of the anomaly at +75% material contrast decreases as the depth of the anomaly increases from the surface. This is shown in the shot records given in Figure 6.7a, Figure 6.7b, Figure 6.7c, and Figure 6.7d.

- The positive dispersion curves remain constant with an increase of frequency as shown in Figure 6.8a, Figure 6.8c, Figure 6.8e, and Figure 6.8g, when the depth of the anomaly at +75% material contrast increases. The amplitudes of reflection in the negative dispersion curves decrease with an increase of depth of the anomaly from the surface. This is shown in Figure 6.8b, Figure 6.8d, Figure 6.8f, and Figure 6.8h.

- The anomaly at -75% material contrast traps energy and causes reverberation when it is introduced close to the surface. Reverberation of trapped energy can be seen in the shot record of Figure 6.9a, which is computed from the model with an anomaly 4 meters below the surface and with -75% material contrast.

- Positive dispersion curves computed for the anomaly with -75% material contrast from the surrounding medium remain constant at depths of 4, 7, 10, and 19 meters, as shown in Figure 6.10a, Figure 6.10c, Figure 6.10e, and Figure 6.10g respectively. In Figure 6.10c, the lower amplitudes of Rayleigh waves at 128 Hz with a corresponding velocity of 1675 m/s are found in the positive dispersion curves where the depth of the anomaly is 7 meters from the surface. The wavelength computed by using the velocity and frequency relationship, in the region of missing energy was found to be λ =13. Using the half wavelength criteria,

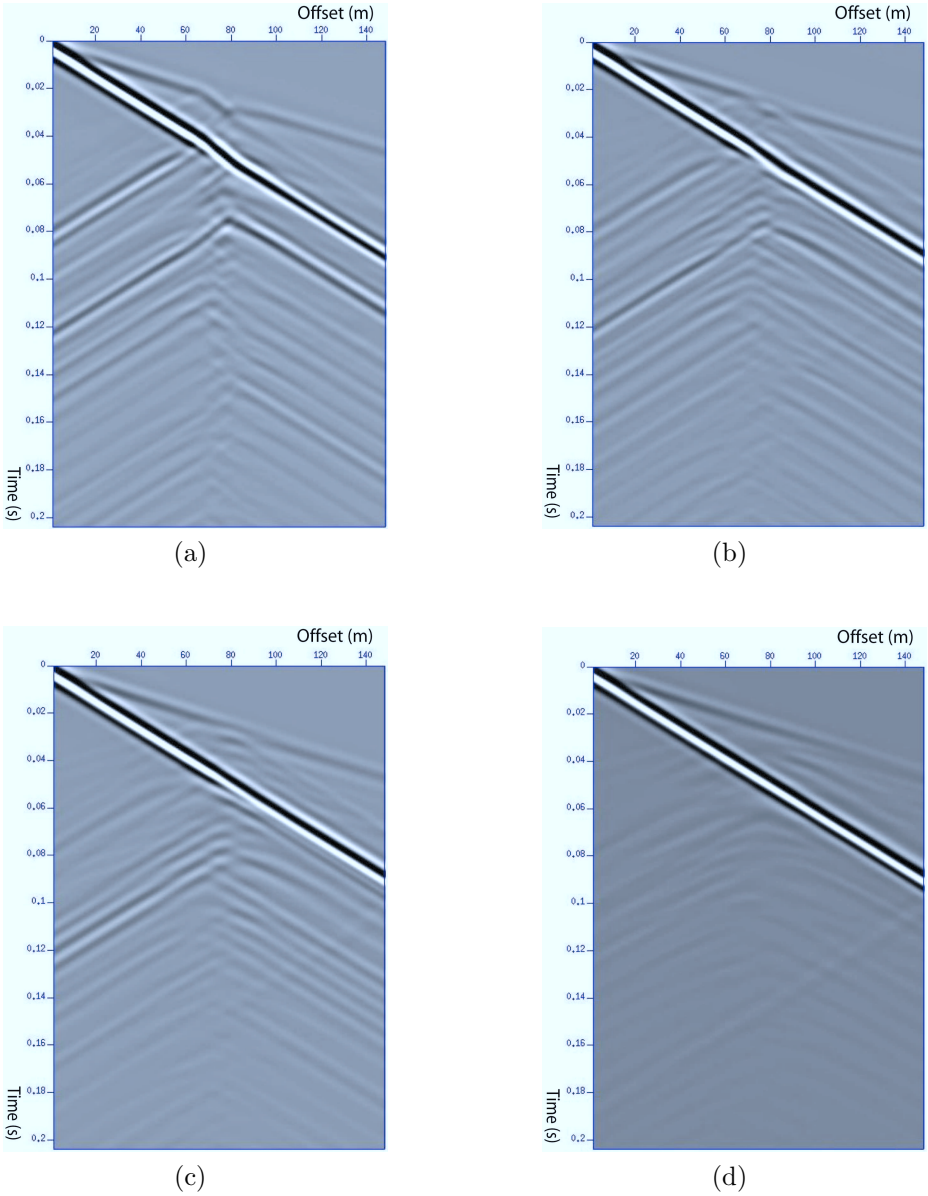

Figure 6.9: The shot records for the rectangular anomaly at -75% material contrast, at (a) 4, (b) 7, (c) 10, and (d) 19 meters below the surface. Trapped energy causing reverberation is seen in each shot record.

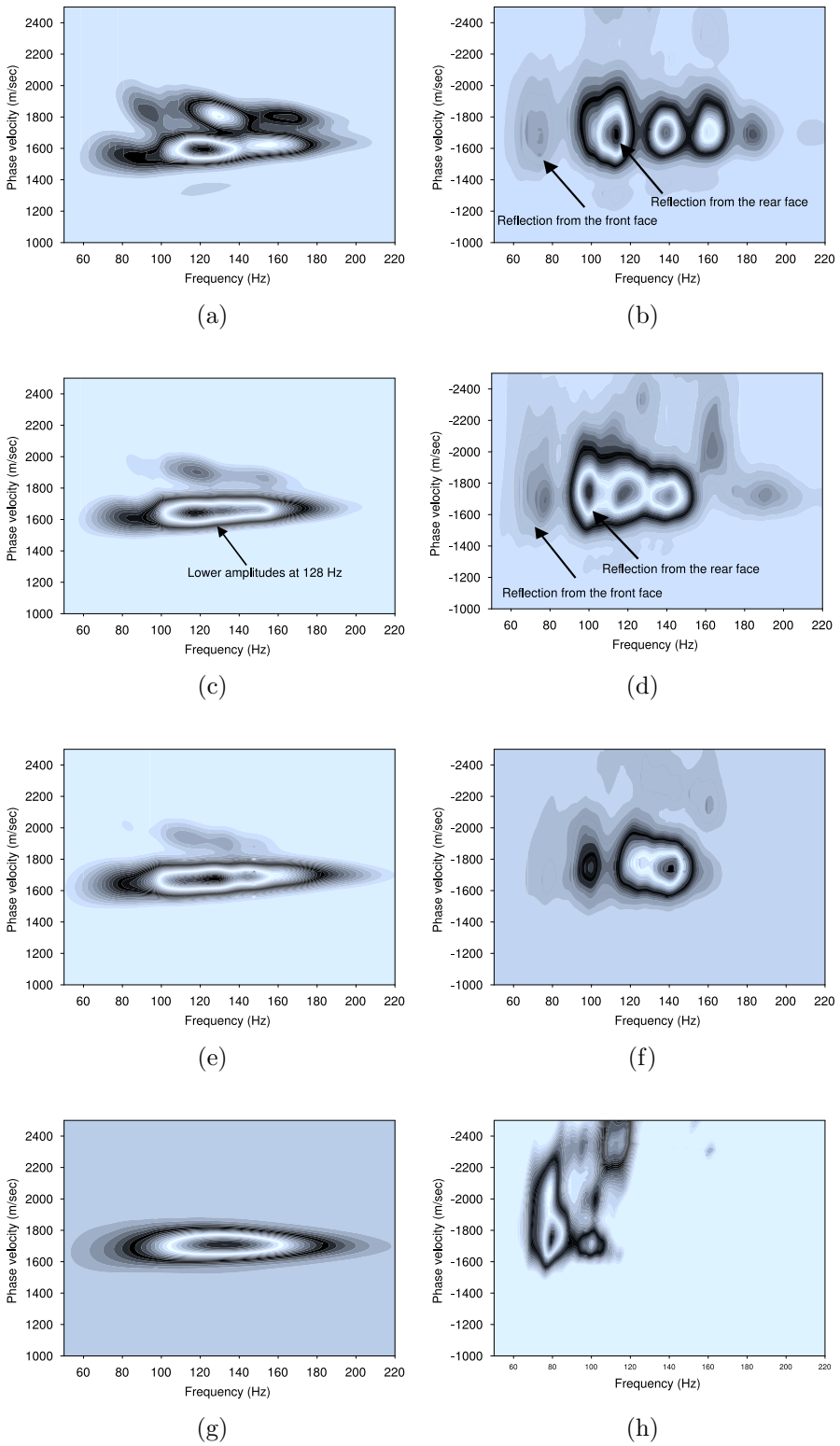

Figure 6.10: The positive dispersion curves are represented in (a), (c), (e), and (g), and the negative dispersion curves are shown in (b), (d), (f), and (h) for the rectangular anomaly at -75% material contrast. The Rayleigh waves are more sensitive to the anomaly close to the surface.

the approximate depth of the anomaly as being 7 meters. This matches the original depth of the anomaly. Reflections from the front and rear faces are seen in the negative dispersion curves shown in the Figure 6.10b, Figure 6.10d, Figure 6.10f, and Figure 6.10h. The width or radius of an anomaly can be computed by computing the wavelengths of the reflected waves from the front and rear faces. From the dispersion curve of Figure 6.10b, the wavelength, λ_1, of the reflected wave from the front face, at frequency 75 Hz and a velocity of 1700 m/s, is 22.6 meters. The wavelength λ_2 of reflected wave from rear face at frequency 115 Hz with the velocity 1700 m/s is approximately 15 meter. Hence the width of the rectangular anomaly of -75% material contrast is given by $\lambda_1 - \lambda_2 \approx 7$ meter. This matches the original width of the anomaly. However it does not always give meaningful results.

6.7 Parametric Study of the Effect of the Shape of a Circular Anomaly on the Rayleigh Wave Dispersion Curve for +75% Material Contrast

It was found that the Rayleigh wave dispersion curve is more sensitive when an anomaly is placed closer to the surface. Therefore, in order to study the effect of the shape of the circular anomaly, the anomaly is placed 4 ($\approx \frac{\lambda}{5}$) meters below the surface. Shot records were computed from models where the radius of the circular anomaly is increased gradually from 4 ($\approx \frac{\lambda}{5}$) meters to 9 ($\approx \frac{\lambda}{2}$) meters with the material contrast of +75 % of the surrounding medium. Direct P and S wave arrivals are clear in each seismogram of Figure 6.11a, Figure 6.11b, Figure 6.11c, and Figure 6.11d. It is observed that the reflected wave in the seismogram became broader as the radius of the anomaly is increased. As shown in the Figure 6.11a, the reflected wave is compressed in the shot record where the anomaly of 4 meter radius and is broadened for the anomaly of 9 meter radius, as shown in Figure 6.11d. The positive dispersion curves computed for the above shot records are shown in Figure 6.12a, Figure 6.12c, Figure 6.12e, and Figure 6.12g, respectively. The phase velocity remains constant with an increase of frequency when the radius of the anomaly increases in positive dispersion curves. The negative dispersion curves are given in Figure 6.12b, Figure 6.12d, Figure 6.12f, and Figure 6.12h. A strong reflection is observed in the

negative dispersion curve when the radius increases.

6.8 Parametric Study of the Effect of the Shape of a Circular Anomaly on the Rayleigh Wave Dispersion Curve for -75% Material Contrast

The effect of the shape of a circular anomaly is studied for a material contrast of -75% from the surrounding medium. The shot records for this study are given in Figure 6.13a, Figure 6.11b, Figure 6.11c and Figure 6.11d. Direct P and S waves along with reverberated trapped energy inside the anomaly are seen in each shot record. As the radius of an anomaly increases, the distance between the two reflected energies from outer and inner faces of the circle increases as well, as seen in the shot records. The positive dispersion curves in this case are shown in Figure 6.14a, Figure 6.14c, Figure 6.14e and Figure 6.14g. Lower amplitudes of Rayleigh waves in different frequencies are observed in the positive dispersion curves when the radius of the anomaly increases. However, the depth of the circular anomaly can not be computed from the frequency and the velocity where amplitudes of the Rayleigh waves are attenuated. Reflection energy from the outer and inner edges of the circle is seen in the negative dispersion curves of Figure 6.14b, Figure 6.14d, Figure 6.14f, and Figure 6.14h. The energy in the negative dispersion curves spread out due to reverberation.

6.9 Results Summary of the Effect of the Shape of a Circular Anomaly on Rayleigh Waves for +75% and -75% Material Contrast

- The distance between the reflected waves from outer and inner faces of the circle for +75% material contrast increases as radius of the circular anomaly increases. This is shown in Figure 6.11a, Figure 6.11b, Figure 6.11c and Figure 6.11d.

- When the radius of the anomaly of +75% material contrast increases, the positive dispersion curves remain constant with an increase of frequency. This is shown in Figure 6.12a, Figure 6.12c, Figure 6.12e, and Figure 6.12g when radius of the anomaly of +75% material contrast increases. Reflected energy from the anomaly is observed in the negative dispersion curves as shown of Figure 6.12b,

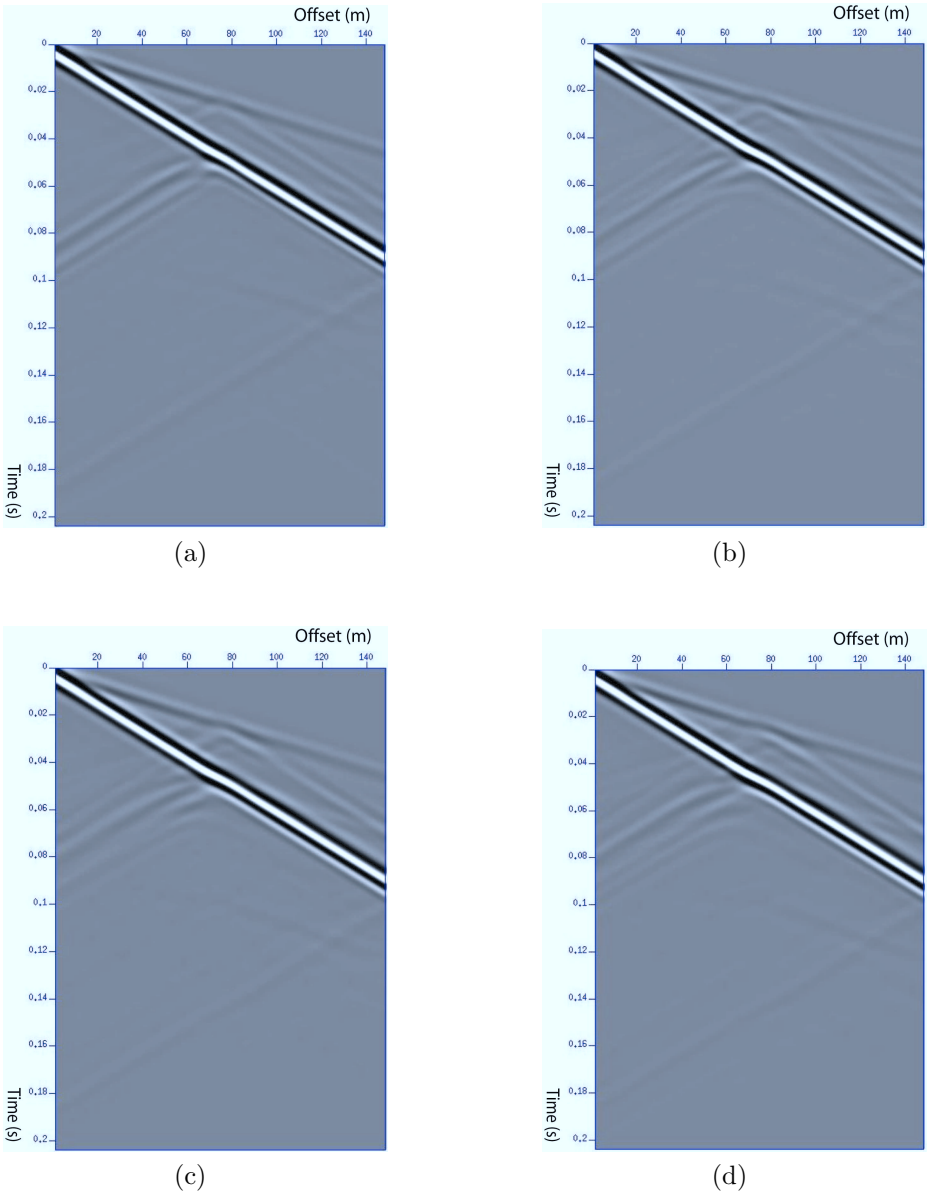

Figure 6.11: The shot records for circular anomaly of +75 % material contrast with a radius of (a) 4, (b) 6, (c) 7, and (d) 9 meters which are placed 4 meters below the surface.

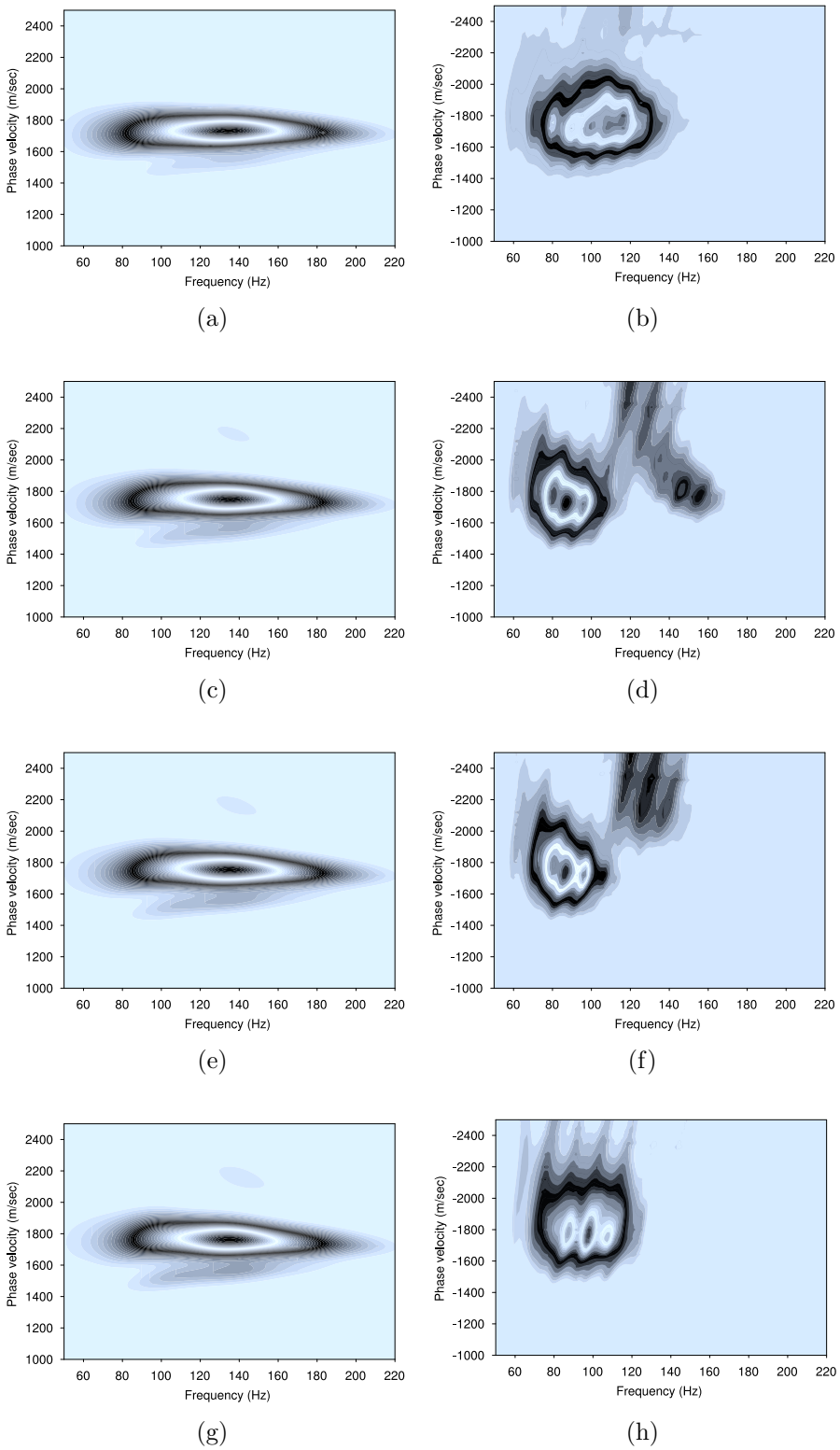

Figure 6.12: The positive dispersion curves are represented in (a), (c), (e), and (g), and the negative dispersion curves are shown in (b), (d), (f), and (h) for the circular anomaly with 4, 6, 7 and 9 meters radius and at +75% of material contrast.

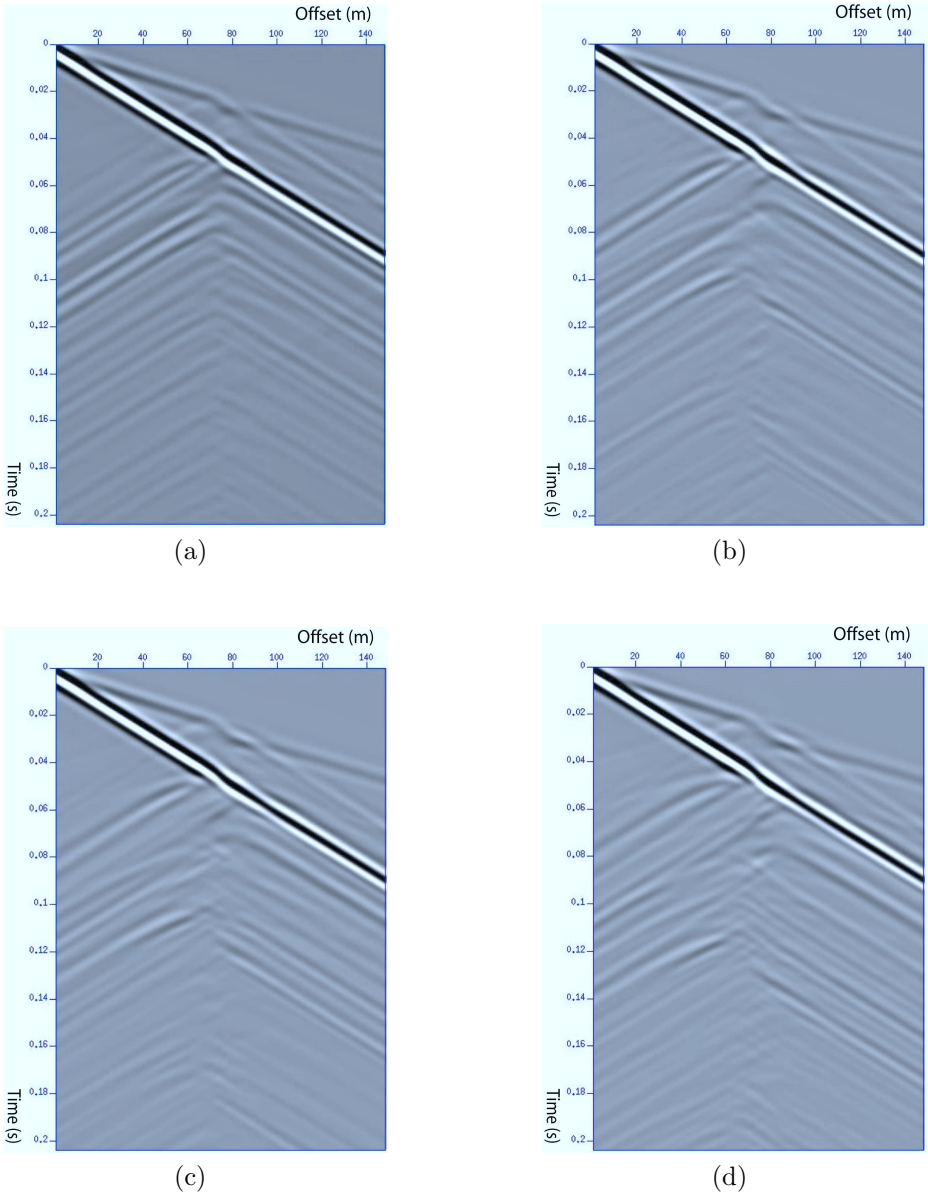

Figure 6.13: The shot records for the circular anomaly at -75% material contrast with a radius of (a) 4, (b) 6, (c) 7, and (d) 9 meters which were placed at 4 meters below the surface.

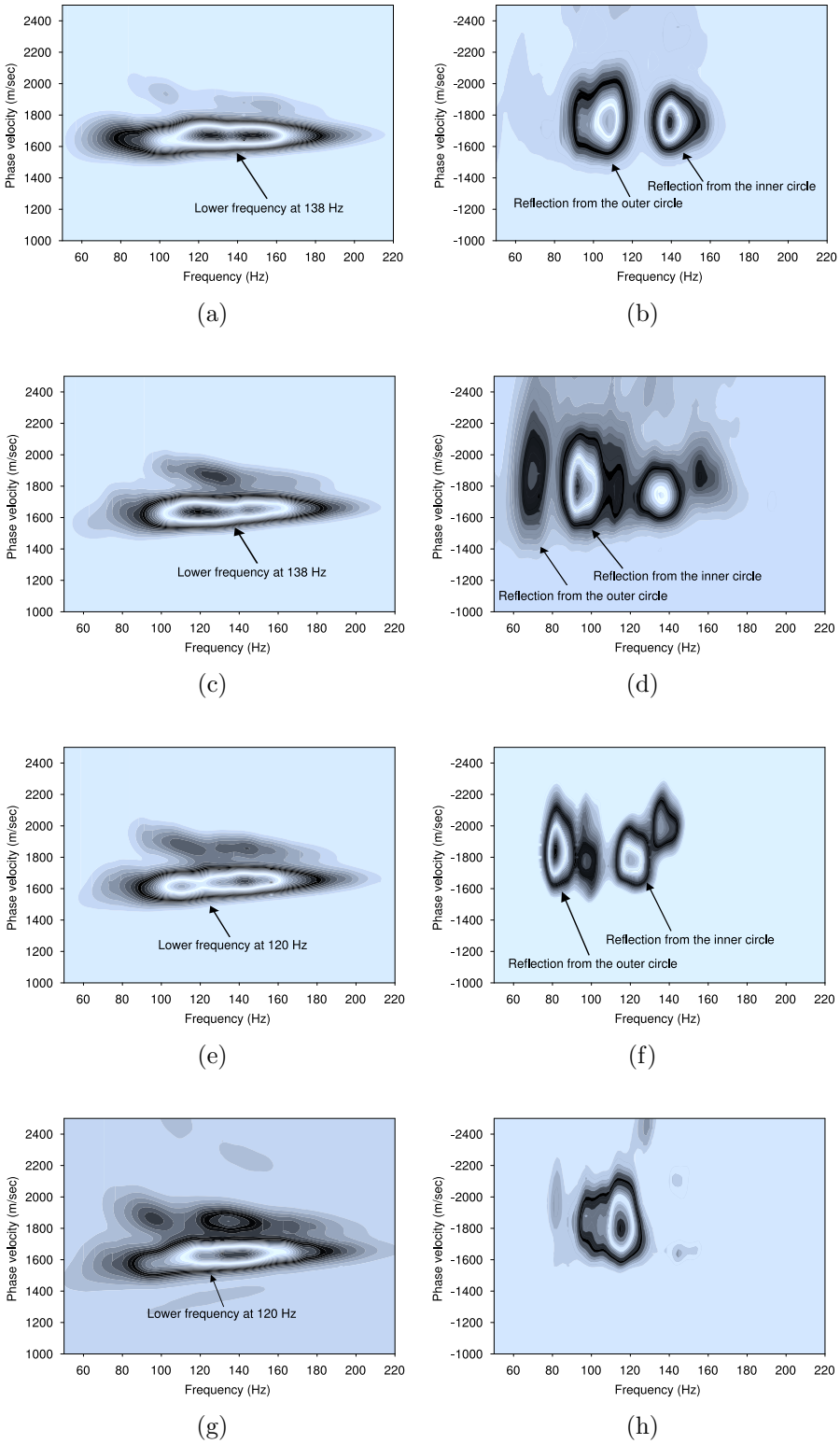

Figure 6.14: The positive dispersion curves are represented in (a), (c), (e), and (g) and the negative dispersion curves are shown in (b), (d), (f), and (h) for the circular anomaly with 4, 6, 7 and 9 meters radius and at -75% of material contrast.

Figure 6.12d, Figure 6.12f, and Figure 6.12h.

- An anomaly of -75% material contrast traps energy and causes reverberation. Reverberation of the trapped energy can be seen in the shot records of Figure 6.13a, Figure 6.11b, Figure 6.11c, and Figure 6.11d.

- Lower amplitudes at different frequency bands were observed in the positive dispersion curves when radius of the circular anomaly with -75% material contrast increases. However, the frequency and the velocity where the amplitudes are attenuated, cannot be used to compute the depth of the anomaly due to its circular shape.

6.10 Parametric Study of the Effect of the Shape of a Rectangular Anomaly on the Rayleigh Wave Dispersion Curve

The affect of the shape of a rectangular anomaly on the Rayleigh wave dispersion curve is studied by changing the height and width of an anomaly for +75% and -75% the material contrast. In this study, the anomaly is placed 4 meters below the surface. First, the effect of height of an anomaly is studied by changing the height of the anomaly from 4 meters to 19 meters i.e. from $\approx \frac{\lambda}{5}$ to $\approx \lambda$ meters at 3 meters increment for +75% material contrast. The resulting models of 4 ($\approx \frac{\lambda}{5}$),7 ($\approx \frac{\lambda}{3}$),10 ($\approx \frac{\lambda}{2}$),13 ($\approx \frac{\lambda}{1.4}$),16 ($\approx \frac{\lambda}{1.2}$) and 19 ($\approx \lambda$) meters were studied. The results for 13 and 16 are not interesting enough to display and to save space they are not shown. The Figure 6.15a, Figure 6.15b, Figure 6.15c, and Figure 6.15d represent the shot records computed from the models with an anomaly of 4, 7, 10 and 19 meters height. The arrival of the direct P and S waves can be observed in the shot records as well as reflections from the side of the anomaly. The positive dispersion curves computed for the above shot records are given in Figure 6.16a, Figure 6.16c, Figure 6.16e, and Figure 6.16g. The phase velocity of the Rayleigh waves remains constant with increase of frequencies in the positive dispersion curves when the height of the anomaly increases. As shown in the negative dispersion curves of Figure 6.16b, Figure 6.16d, Figure 6.16f, and Figure 6.16h, the amplitudes of reflected wave increases as the height of the anomaly increases in the negative dispersion curves.

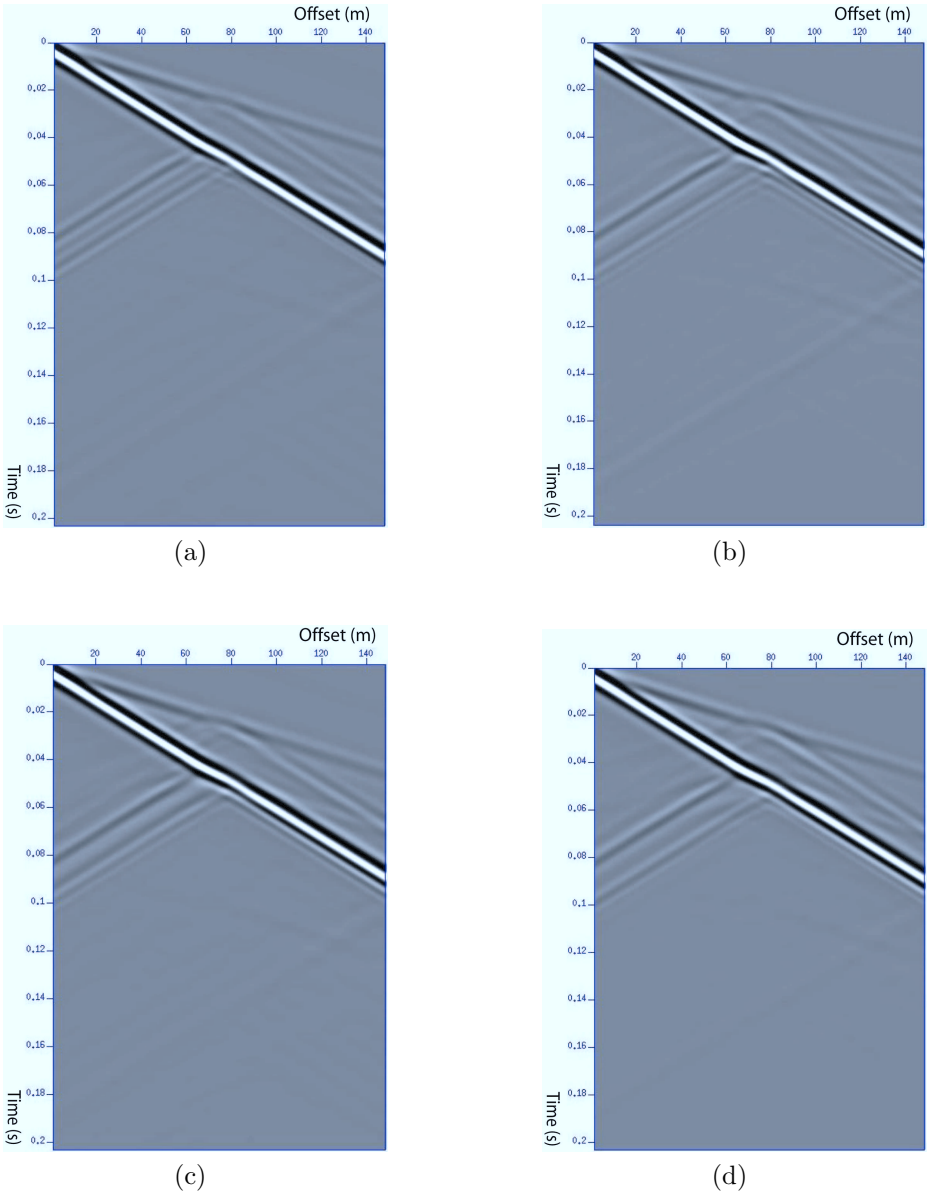

Figure 6.15: The shot records for +75% material contrast of a rectangular anomaly with a height of (a) 4, (b) 7, (c) 10, and (d) 19 meters.

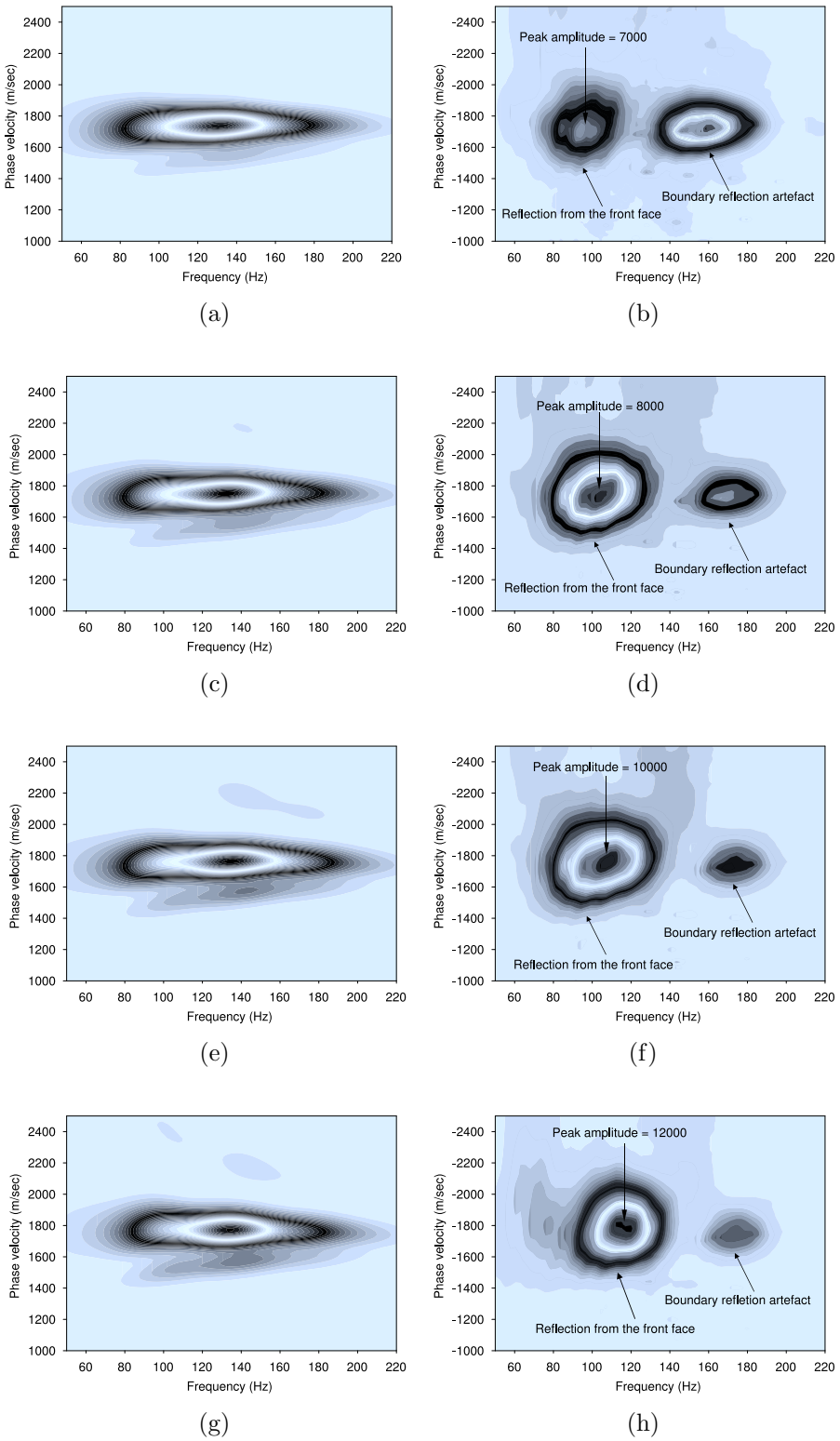

Figure 6.16: The positive dispersion curves are represented in (a), (c), (e), and (g) and the negative dispersion curves are shown in (b), (d), (f), and (h) for the rectangular anomaly of height 4, 7, 10 and 19 meters at +75% of material contrast.

A parametric study of the height of a rectangular anomaly is also conducted for the anomaly at -75% material contrast from the surrounding medium. The shot records computed from the models with an anomaly of 4, 7, 10 and 19 meters height are represented in the Figure 6.17a, Figure 6.17b, Figure 6.17c, and Figure 6.17d, respectively. The direct P, S waves are seen in each shot record. Reverberation due to the trapped energy inside the anomaly is also observed in the shot records. The positive and negative dispersion curves for the above shot record are computed. Lower amplitudes in a particular frequency band are seen in each of the positive dispersion curves. As the height of the anomaly increases, the low amplitudes zone moves to a lower frequency along the frequency axis, as shown in Figure 6.18a, Figure 6.18c, Figure 6.18e, and Figure 6.18g. This is because low frequencies are affected as the height of the anomaly increases. Reflected energy from the side of the anomaly is seen in the negative dispersion curves in a diffused form as shown in Figure 6.18b, Figure 6.18d Figure 6.18f, and Figure 6.18h. Therefore, any information about the geometry of the anomaly cannot be obtained from the negative dispersion curves.

6.11 Results Summary of the Effect of Height of a Rectangular Anomaly on Rayleigh Waves for +75% and -75% Material Contrast

- The direct P, S waves and reflected waves from the side of the anomaly can be seen in each shot record, computed from the models with an anomaly with increasing height and of +75% material contrast, as shown in Figure 6.15a, Figure 6.15b, Figure 6.15c, and Figure 6.15d.

- The positive dispersion curves remain constant with an increase of frequency when the height of the anomaly at +75% material contrast increases, as shown in Figure 6.16a, Figure 6.16c, Figure 6.16e, and Figure 6.16g. The reflected energy from the anomaly is observed in the negative dispersion curves as shown in. The amplitudes of the reflected energy from the side of the anomaly increases when the height of the anomaly increases. This is shown in Figure 6.16b, Figure 6.16d, Figure 6.16f and Figure 6.16h.

- An anomaly at -75% material contrast traps energy and causes reverberation.

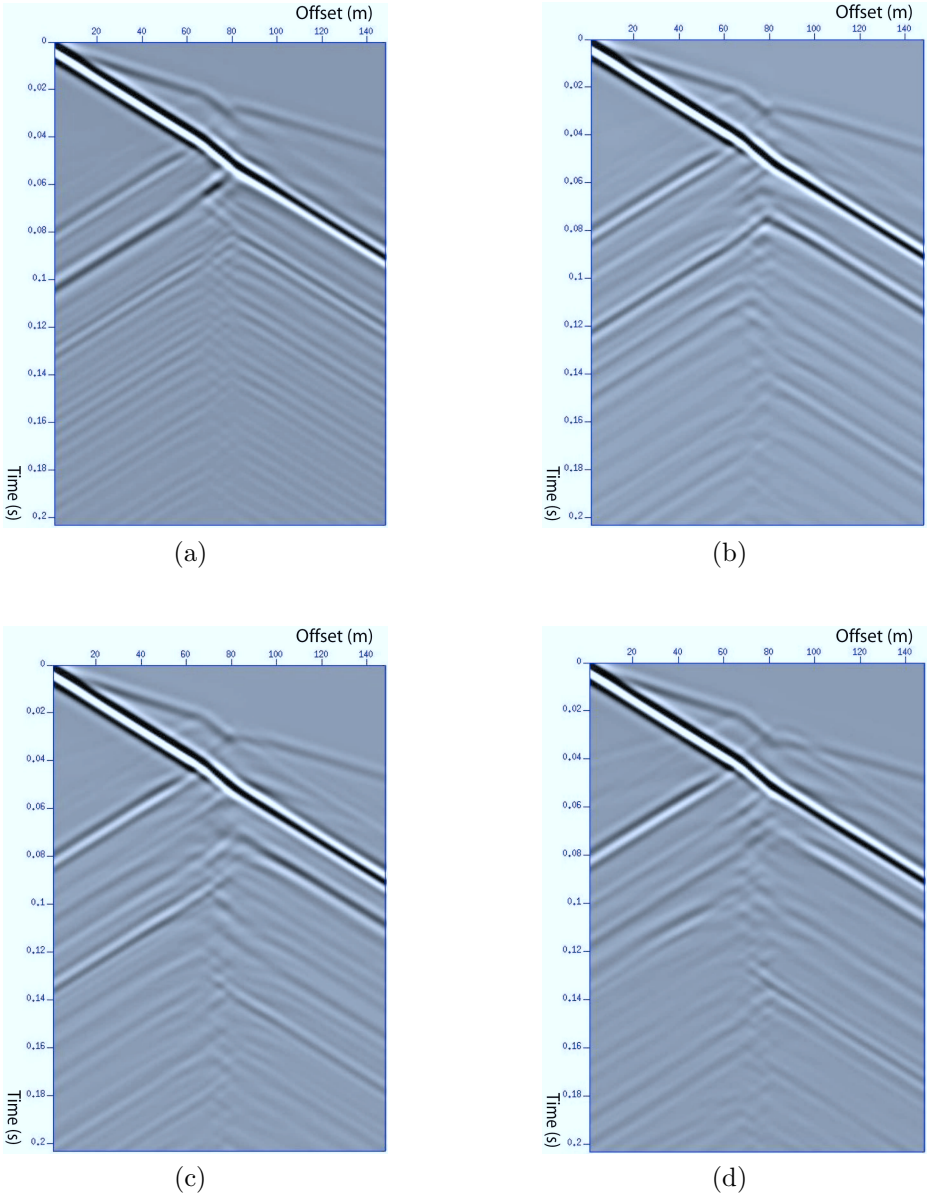

Figure 6.17: The shot records at -75% material contrast of a circular anomaly with a radius of (a) 4, (b) 7, (c) 10, and (d) 19 meters.

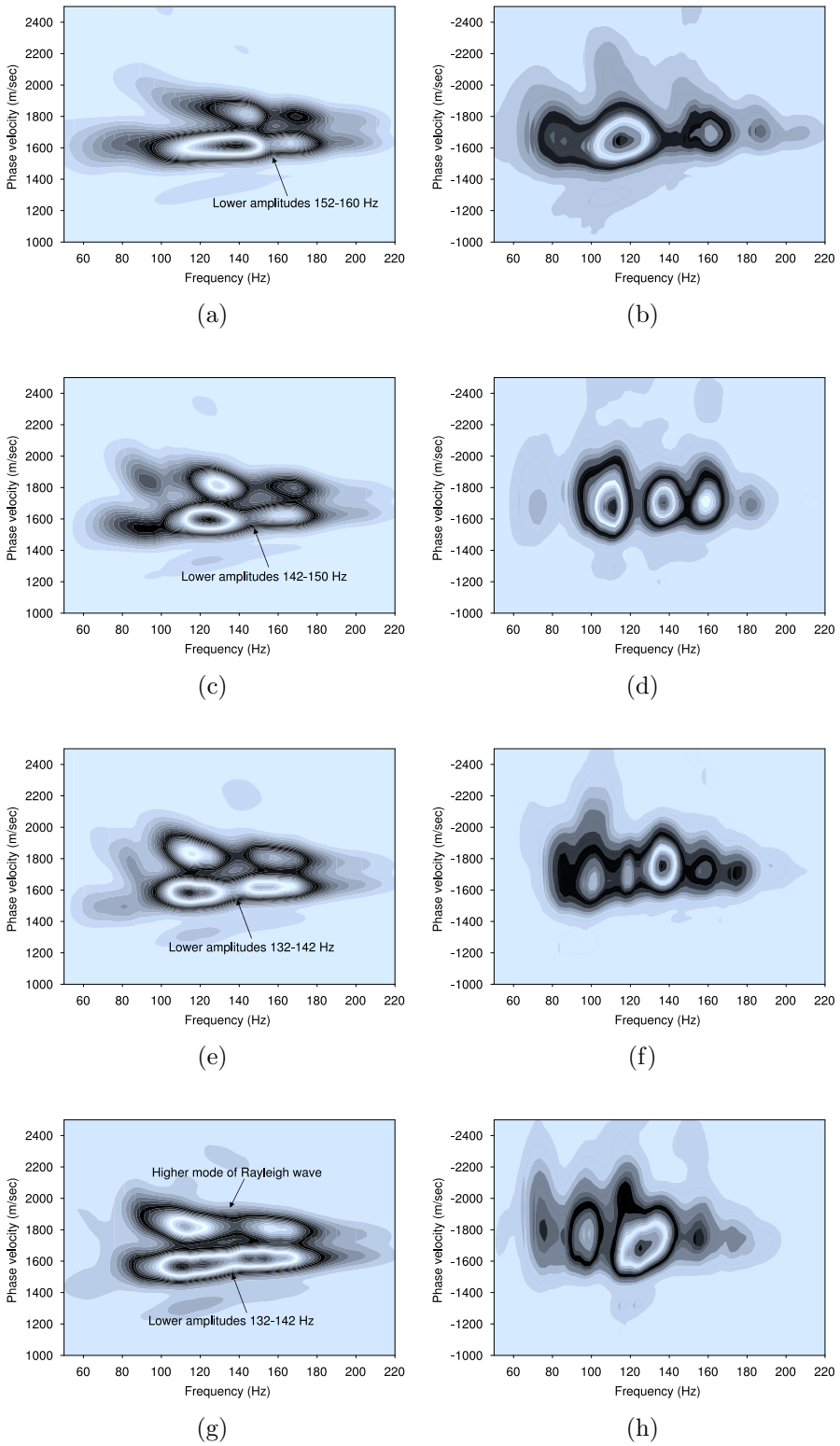

Figure 6.18: The positive dispersion curves are represented in (a), (c), (e), (g) and the the negative dispersion curves are shown in (b), (d), (f), and (h) for the rectangular anomaly of height 4, 7, 10 and 19 meters at -75% of material contrast.

Reverberation of trapped energy can be seen in the shot records of Figure 6.17a, Figure 6.17b, Figure 6.17c, and Figure 6.17d, when the height of the anomaly increases.

- As the height of the anomaly increase the low amplitudes zone moves to a lower frequency along the frequency axis, as shown in Figure 6.18a, Figure 6.18c, Figure 6.18e, and Figure 6.18g. This is because low frequencies are affected when height of the anomaly increases. The energy reflected from the side of the anomaly is seen in the negative dispersion curves in a diffused form, as shown in Figure 6.18b, Figure 6.18d Figure 6.18f, and Figure 6.18h.

The effect of the width of the rectangular anomaly at +75% material contrast on the Rayleigh waves dispersion curve is studied by changing the width of the anomaly to 4 ($\approx \frac{\lambda}{5}$), 7 ($\approx \frac{\lambda}{3}$), 10 ($\approx \frac{\lambda}{2}$), and 19 ($\approx \lambda$) meters, keeping the constant height of 4 meters. The shot records computed from this model is represented in Figure 6.19a, Figure 6.19b, Figure 6.19c, and Figure 6.19d, respectively. It is observed that, as the width of the anomaly increases. the distance between the two reflected waves from the two faces of the anomaly increases. The phase velocity in the positive dispersion curve remains constant with the increase of frequencies, as shown in Figure 6.20a, Figure 6.20c, Figure 6.20e, and Figure 6.20g. Reflection from the sides of the anomaly is observed in the negative dispersion curves of Figure 6.20b, Figure 6.20d, Figure 6.20f, and Figure 6.20h. No significant trend is observed in the negative dispersion curves when the width of the anomaly increases, and the height is kept constant for +75% material contrast of the surrounding.

The shot records were computed from the models with an anomaly of -75% material contrast and varying widths of 4 ($\approx \frac{\lambda}{5}$), 7 ($\approx \frac{\lambda}{3}$), 10 ($\approx \frac{\lambda}{2}$), and 19 ($\approx \lambda$) meters, keeping the height constant, are represented in Figure 6.21a, Figure 6.21b, Figure 6.21c, and Figure 6.21d. As the width of the anomaly increases, reverberated energy inside the anomaly also increases. The positive dispersion curves computed for these shot records are given in Figure 6.22a, Figure 6.22c, Figure 6.22e and Figure 6.22g. As the width of the anomaly increases, amplitudes of the Rayleigh waves attenuated in a particular frequency band are related to the depth of the anomaly. Since the depth of the anomaly is the same for all cases, their lower amplitudes in a

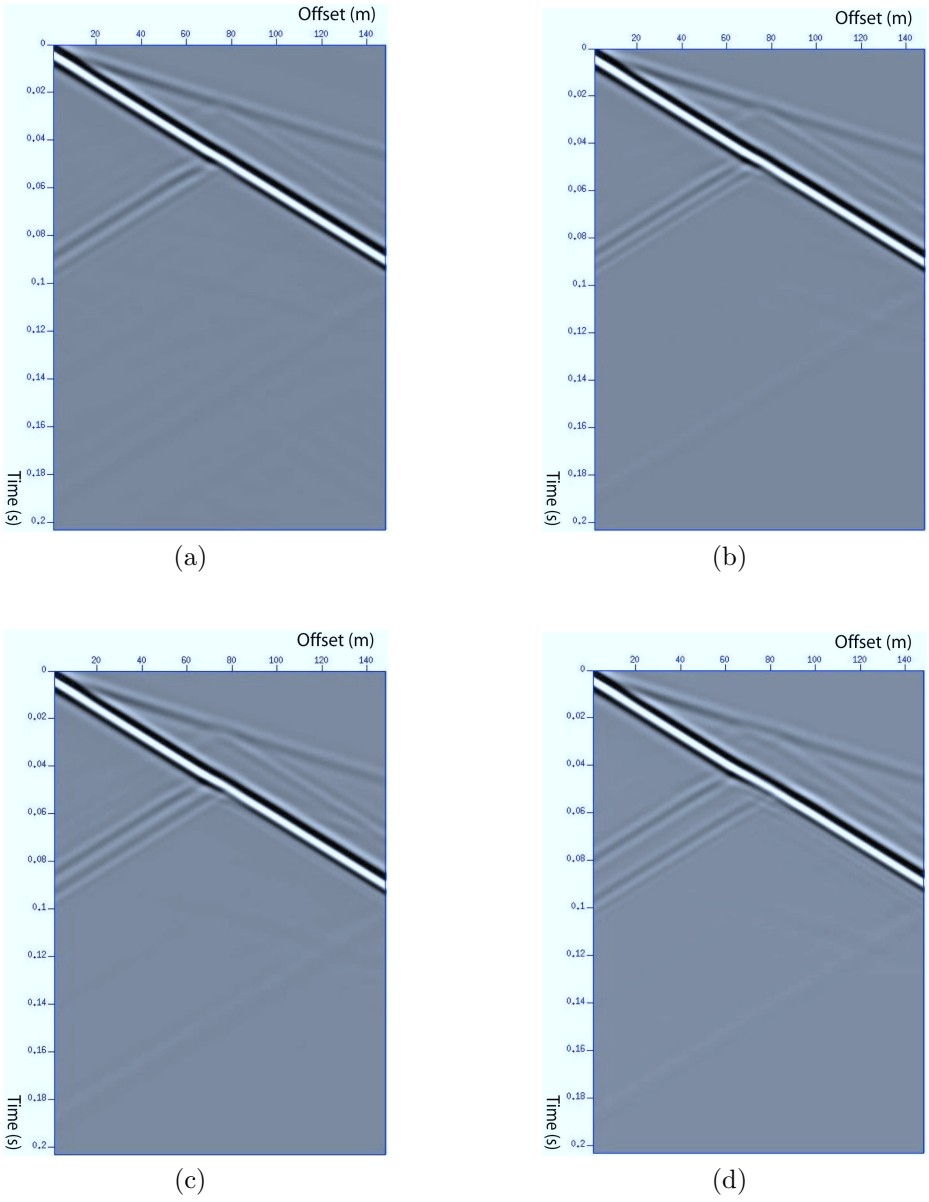

Figure 6.19: The shot records for +75% material contrast of a rectangular anomaly with a width of (a) 4, (b) 7, (c) 10, and (d) 19 meters, with a height of 4 meters.

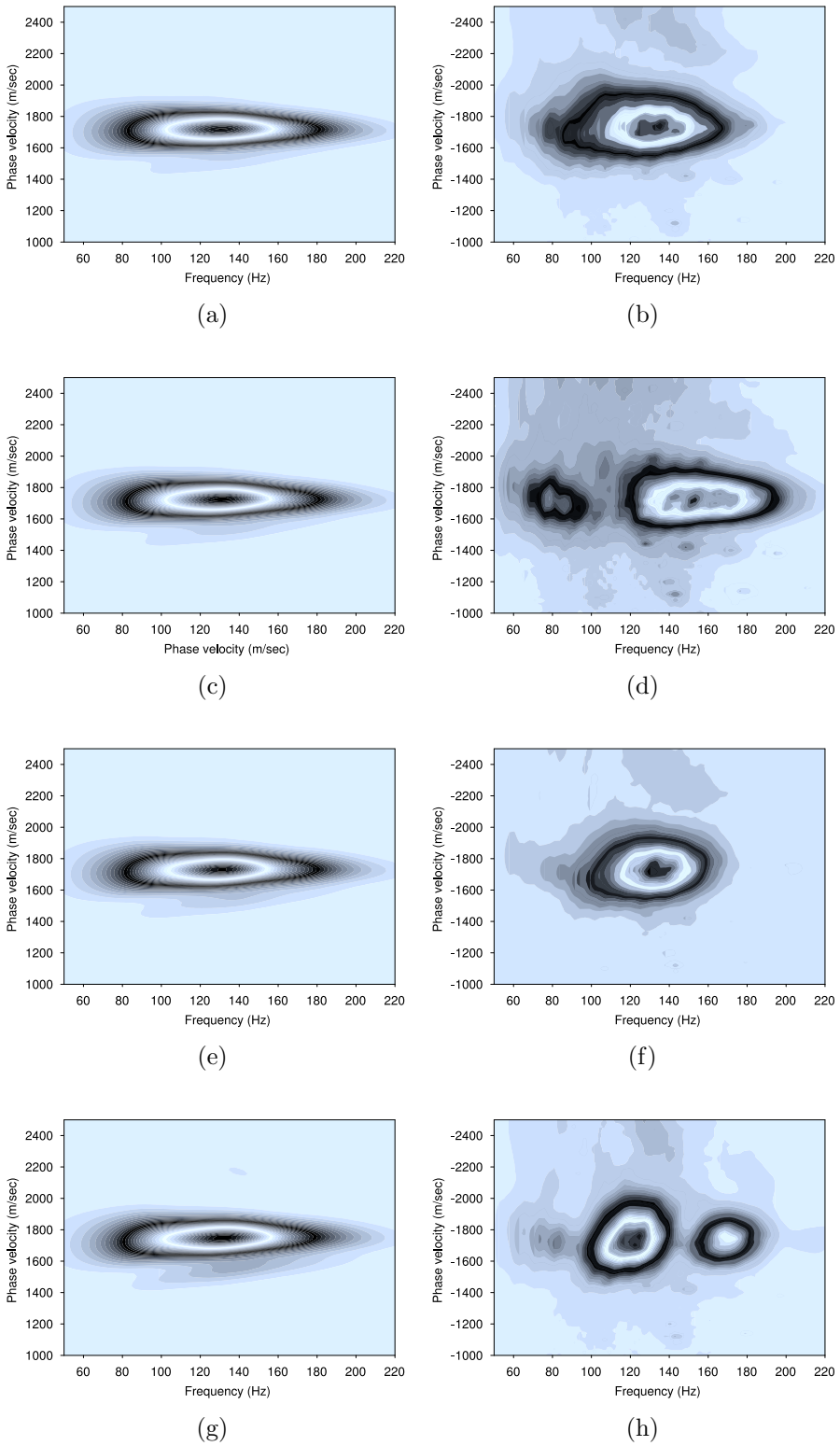

Figure 6.20: The positive dispersion curves are represented in (a), (c), (e), and (g) and the negative dispersion curves are shown in (b), (d), (f), and (h) of the rectangular anomaly widths of 4, 7, 10, and 19 meters at +75% of material contrast with a height of 4 meters.

particular frequency band remain the same as well. The negative dispersion curves shown in Figure 6.22b, Figure 6.22d, Figure 6.22f and Figure 6.22h show the reflected energy from the front and rear faces of the anomaly.

The effect of the width of a rectangular anomaly is studied again for a height of 19 meters. The shot records computed for this study for +75% material contrast is represented in Figure 6.23a, Figure 6.23b, Figure 6.23c and Figure 6.23d. strong reflection is observed in the shot record of Figure 6.23a, which is computed from the model with an anomaly height of 19 meters and a width of 4 meters. As the width of the anomaly increases, the distance between the reflected waves also increases. The positive dispersion curves computed for the above shot records are given in Figure 6.24a, Figure 6.24c, Figure 6.24e, and Figure 6.24g. The positive dispersion curves show that phase velocity remains constant with increases of frequency, and reflected energy is observed in the negative dispersion curves. Strong reflection is seen in negative dispersion curve of Figure 6.26a which is computed from the shot record, where the anomaly, 19 meters high and 4 meters wide is introduced in the model. As the width of the anomaly increases, the reflection from the boundary also increases.

The shot records computed from the models with an anomaly of -75% material contrast and of height 19 meters, in order to see the effect of the width of the anomaly on Rayleigh wave propagation. The shot records are shown in Figure 6.25a, Figure 6.25b, Figure 6.25c and Figure 6.25d for anomaly widths of 4 ($\approx \frac{\lambda}{5}$), 7 ($\approx \frac{\lambda}{3}$), 10 ($\approx \frac{\lambda}{2}$), and 19 ($\approx \lambda$) meters, respectively. Direct P, S waves and reverberated waves are seen in all shot records. Lower amplitudes in a certain frequency band is observed in the positive dispersion curves. The frequency at which amplitudes attenuated is related to the depth of the anomaly. The positive dispersion curves are shown in Figure 6.26a, Figure 6.26c, Figure 6.26e and Figure 6.26g. In the negative dispersion curves, the reflected energy from front and rare face is observed.

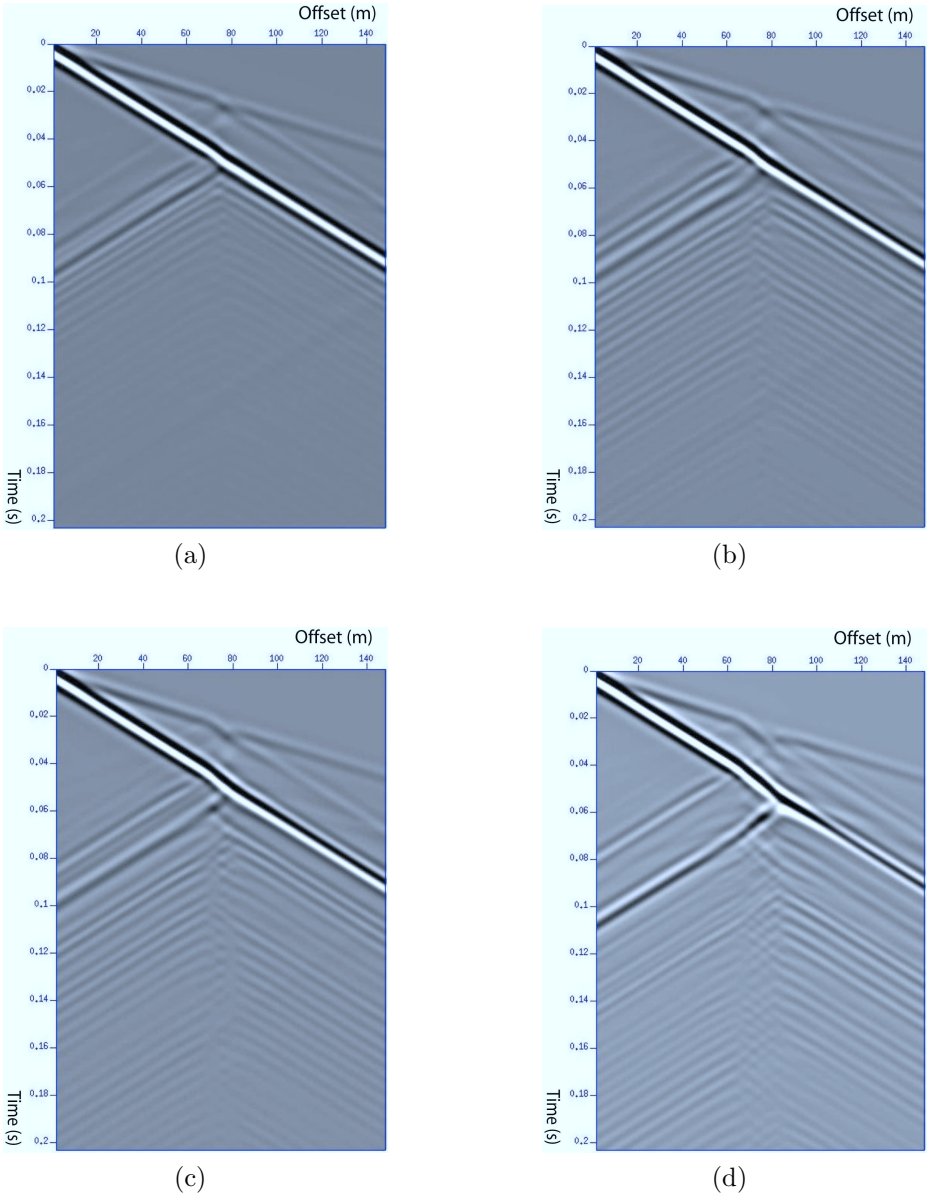

Figure 6.21: The shot records for -75% material contrast of rectangular anomaly with width of (a) 4, (b) 7, (c) 10, and (d) 19 meters at a height of 4 meters.

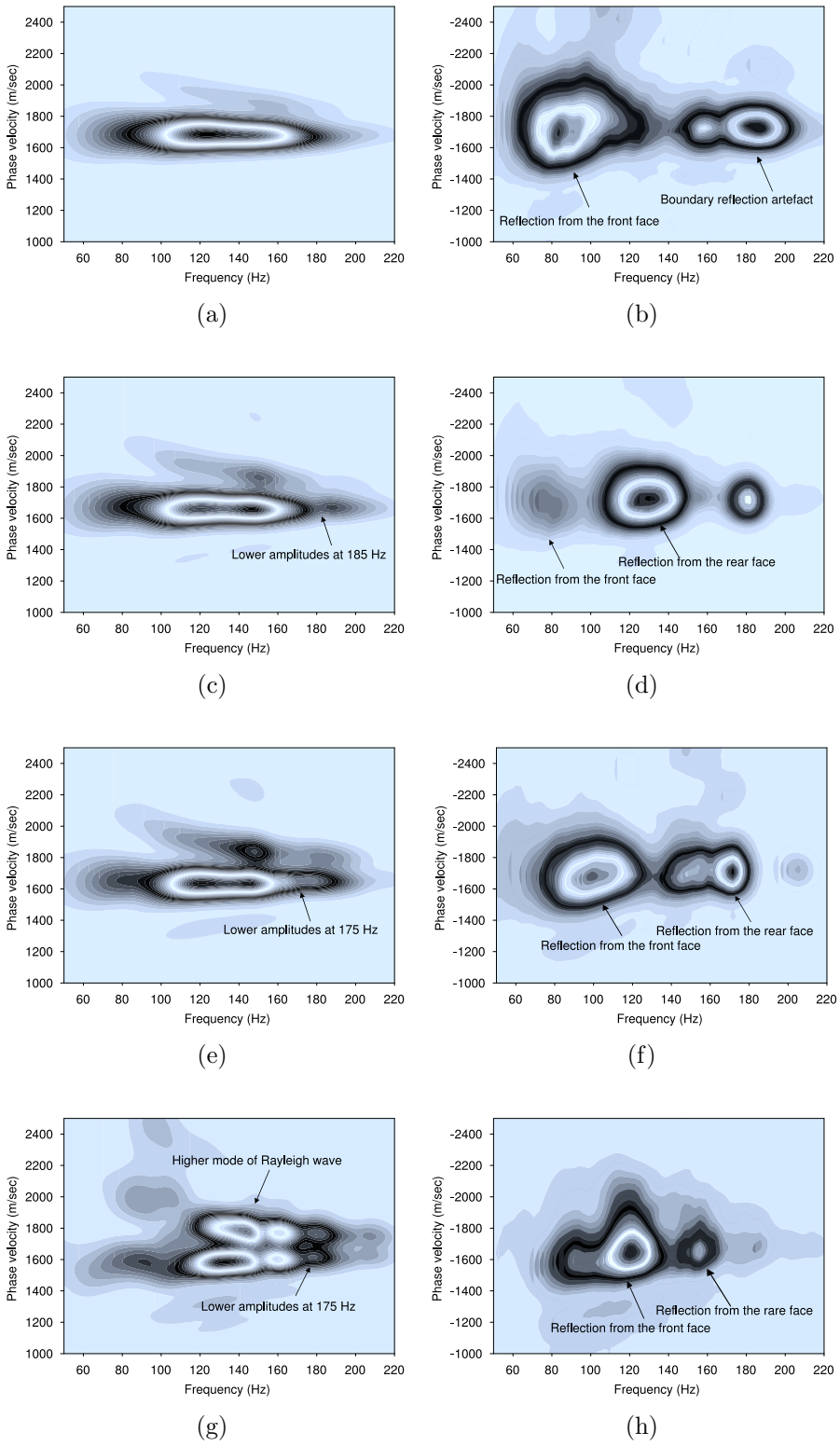

Figure 6.22: The positive dispersion curves are represented in (a), (c), (e), (g) and the negative dispersion curves are shown in (b), (d), (f),and (h) of the rectangular anomaly of widths 4, 7, 10 and 19 meters at -75% of material contrast at a height of 4 meters.

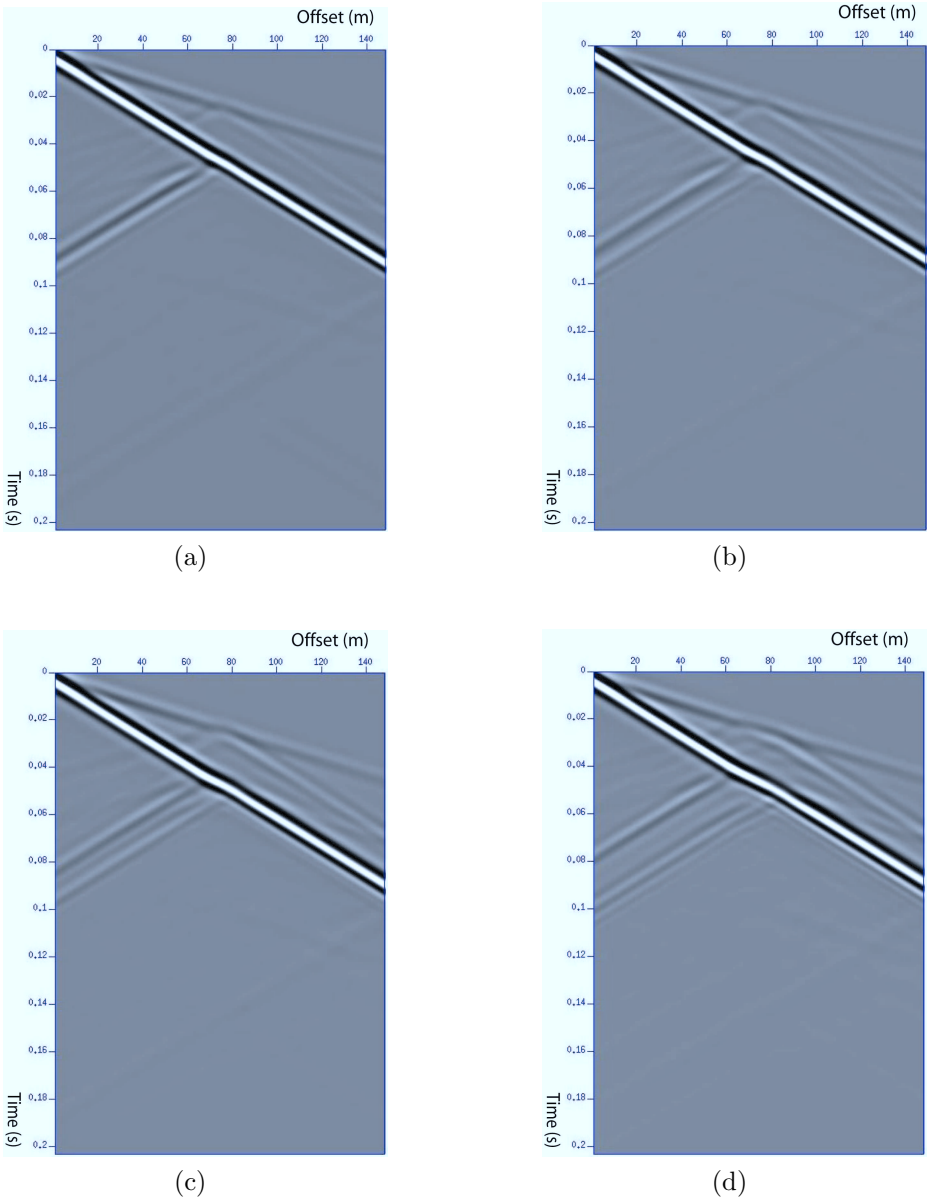

Figure 6.23: The shot records for a rectangular anomaly of +75% material contrast of rectangular anomaly with a width of (a) 4, (b) 7, (c) 10, and (d) 19 meters with a constant height of 19 meters.

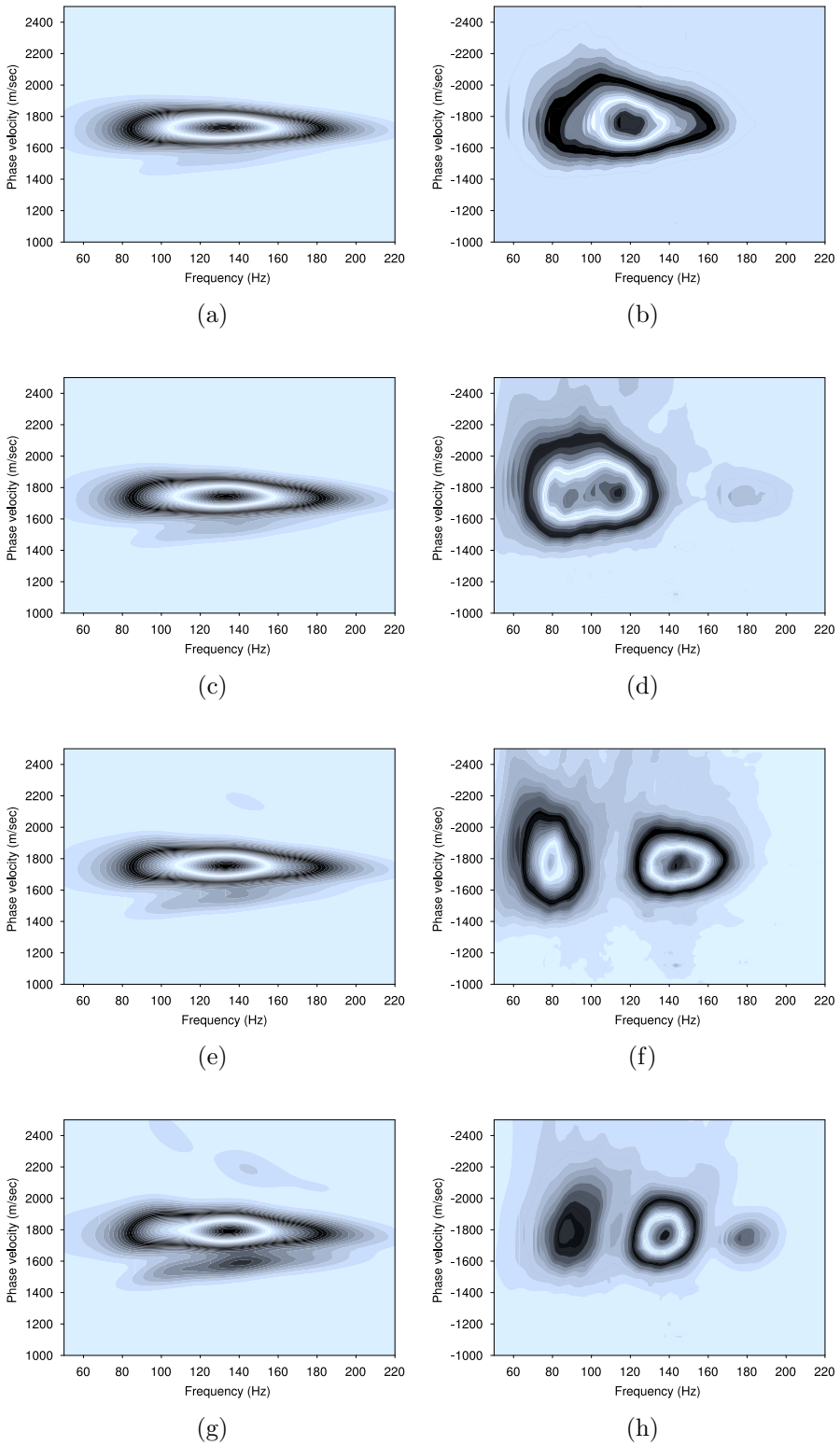

Figure 6.24: The positive dispersion curves are represented in (a), (c), (e), (g) and the negative dispersion curves are shown in (b), (d), (f), and (h) for a rectangular anomaly with a width of 4, 7, 10 and 19 meters at +75% of material contrast at a height of 19 meters.

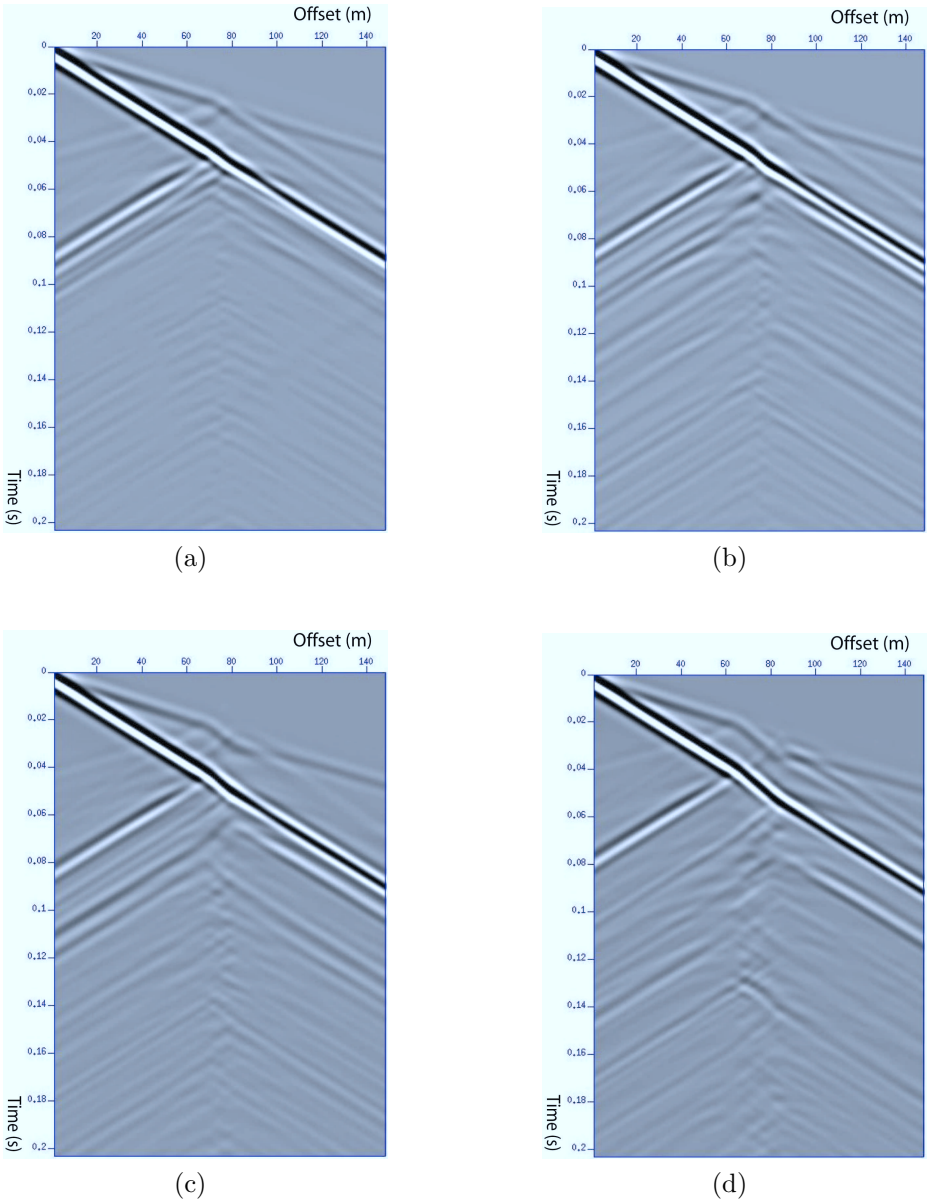

Figure 6.25: The shot records for -75% material contrast of rectangular anomaly with width of (a) 4, (b) 7, (c) 10 (d) 19 meters with a constant height of 19 meters.

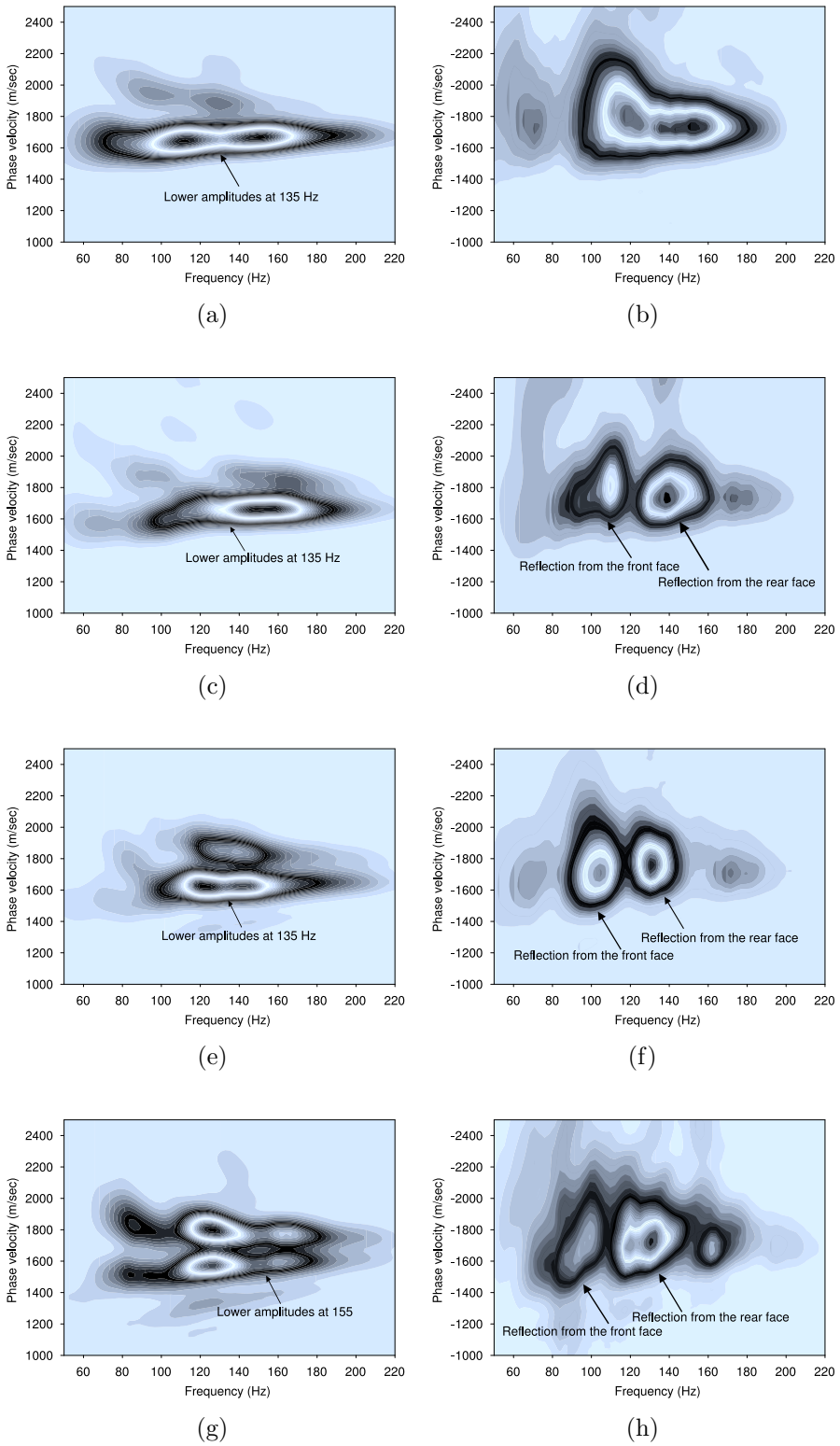

Figure 6.26: The positive dispersion curves are represented in (a), (c), (e), and (g) and the negative dispersion curves are shown in (b), (d), (f), and (h) for the rectangular anomaly with widths of 4, 7, 10 and 19 meters at -75% of material contrast with a height of 19 meters.

6.12 Results Summary of the Effect of the Width of a Rectangular Anomaly on Rayleigh Waves for +75% and -75% Material Contrast

- Direct P, S waves and reflected waves from the side of the anomaly at +75% material contrast can be seen in each shot record computed from the models with a 4 meters high anomaly and incrementing widths of 4 ($\approx \frac{\lambda}{5}$), 7 ($\approx \frac{\lambda}{3}$), 10 ($\approx \frac{\lambda}{2}$), and 19 ($\approx \lambda$) meters as shown in Figure 6.15a, Figure 6.15b, Figure 6.15c, and Figure 6.15d. When the height of the anomaly is increased to 19 meters to see the effect of the width on Rayleigh waves, the results were no different when height of the anomaly was 4 meters.

- The positive dispersion curves remain constant with an increase of frequency when the width of the anomaly at +75% material contrast, increases for the heights of 4 ($\approx \frac{\lambda}{5}$) and 19 ($\approx \lambda$) meters. Reflected energy from the anomaly is observed in the negative dispersion curves. As the width of the anomaly increases, the reflection from the boundary also increases.

- An anomaly at -75% material contrast traps energy and causes reverberation. Reverberation of trapped energy can be seen in the shot records computed from the models with increasing width at heights of 4 ($\approx \frac{\lambda}{5}$) and 19 ($\approx \lambda$) meters.

- Lower amplitudes zone is observed with the increase of width of an anomaly in certain frequency band in positive dispersion curve when the anomaly introduced in the models of -75% material contrast. The effect of the width of an anomaly on the negative dispersion curves were same, even when the height of the anomaly is changed.

Chapter 7

Inversion of Rayleigh Waves Data for near Surface Imaging

7.1 Overview

The S wave velocity profile versus depth is the desired subsurface image, in which, potential anomalies can be detected and located. This can be achieved through the inversion of Rayleigh wave dispersion curves. There are many numerical optimization methods which can be used to minimize a real value function. Even though they do converge, there is no assurance that they have found the global, rather than some local minimum, because conventional algorithms can not distinguish between the two. In order to avoid local optimum, VFSR optimization method was used for the Stellarton field data (Xu et al., 2008). The big advantage of this method is that, it samples the entire surface of the function randomly and tries to optimize the function while moving both uphill and downhill. In this chapter, the inversion of the Sterllarton field data will be presented.

7.2 Geology of Stellarton Field

The Stellarton Basin is situated in the north-central part of Nova Scotia, Canada. This coalfield measures just 18 km east-west by 6 km north-south. There are fifteen major coal seams in the Stellarton basin ranging from 1 to 14 meters in thickness. Twelve seams have previously been mined out. Out of these fifteen coal seams, the Foord seam was found to be the thickest seam in North America at 13.4 meters thick. Stellarton is one the of most productive coal fields in Nova Scotia, Canada, approximately 60 million tonnes of coal have been taken from this field over the last 170 years. Coal used to be accessed by a series of shafts along Foord seams and was hoisted by horse gins. These old, deep, open shafts and tunnels are now causing ground instability. They are considered to be dangerous because their depths are

unknown and because of their locations in the Stellarton area. The coal seams in the Stellarton area have a strike almost east west and dip at 26 degrees towards north. Currently, a large scale mining operation is on going in the Stellarton basin to recover near surface coal resources. Pioneer Coal Ltd. started a mining operation from the Foord seam in 1996 and from the Cage seam in 2001. The company expanded eastward in 2004 for another 1.1 million tonnes from the Cage, Third, McGregor and New seams. Recent and existing mining activities in the Stellarton have found several inclined shafts and tunnels. Figure 7.1 shows the east boundary of the Stellarton pit where four tunnels approximately 5 to 10 meters apart, are observed. All of these tunnels ran approximately in the directions of the coal seams.

Figure 7.1: Old mine tunnels (red lines) and collapse (dashed lines) in the east boundary of the Stellarton pit (from Xu 2008).

7.3 Data Acquisition

A colleague, Chaoqiang Xu from Dalhousie University, led the Subsurface Imaging Group (SIG) to collect data from Stellarton coal field in July 2006. The east boundary of the Stellarton open pit was ideal site for setting up seismic survey lines for data

acquisition, but there was berm and a wire fence along the east boundary. As it was not safe to setup equipment top of or on the inner side of the berm, a survey line was selected on the outside of the berm, which is 15 meters east from the edge of the open pit as shown in Figure 7.2. A one-hundred meter long survey line was used to cover all four tunnels. This is shown in Figure 7.3.

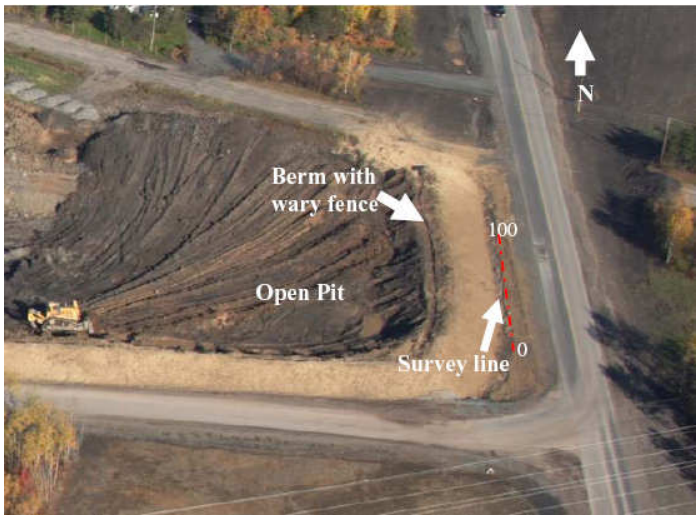

Figure 7.2: One-hundred meters long survey line (red dashed) (from Xu 2008).

Figure 7.3: An one-hundred meters long survey line which cover all four discovered tunnels (from Xu 2008).

The data acquisition system consisted of a Seistronix RAS-24 seismograph, a loptop computer, a 60 meter long geophones string with 12x4.5 HZ geophones, and

a 12 pound sledge hammer source. The 100 meters long survey line was divided into two segments. The first segment ran from stations 0 to 65. The source was at station 0 for the front shot and at station 65 for the back shot. The second segment ran from station 40 to 105. The source was at station 40 for front shot and at station 105 for the back shot. For each of the two segments, five geophone positions were presented in Table 7.1 and were used to form a 56 channel record. Twelve geophones were used in each position. In position 1, the first geophone was five meters away from the source. The Second geophone was one meter away from the first, and rest of the geophones were located five meters apart from each other. As the geophones were moved from position 1 to position 5, geophones from station 2 to station 12 were moved from one to four meters keeping the first position constant, as shown in Figure 7.4. Superposition of all formed a 56 channel array of seismic data with 1 meter geophone spacing between stations 5 and 60, represented in Figure 7.5. The same geometric arrangement for the source and geophones was also used for the second segment to form another 56 channel record from station 45 to 100. Front and back shots were recorded for each segment by stacking ten shots in each position. Sampling frequency was set to 500 Hz and the record length was 1.6 seconds.

Geophone	pos.1	pos.2	pos.3	pos.4	pos.5
1	5	5	5	5	5
2	6	7	8	9	10
3	11	12	13	14	15
4	16	17	18	19	20
5	21	22	23	24	25
6	26	27	28	29	30
7	31	32	33	34	35
8	36	37	38	39	40
9	41	42	43	44	45
10	46	47	48	49	50
11	51	52	53	54	55
12	56	57	58	59	60

Table 7.1: Geophone positions for the 56 channel record of line 1.

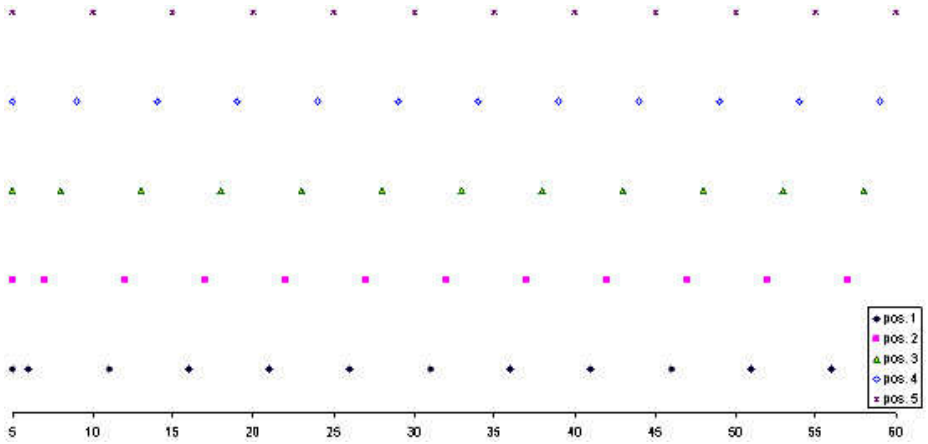

Figure 7.4: The five geophone positions.

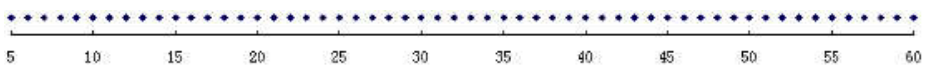

Figure 7.5: 56 channel array obtained from the superposition of the five geophone positions.

7.4 Reference and Model Data Preparation for Inversion

Multichannel data was collected using two survey lines. Each survey line had two front and two back shots and each shot contained 56 channels. Both of the survey lines were combined together to form 96 channel array. Each shot record is then divided into six panels of sequences of traces. This gave a total of 24 panels from all four shot records.

The dispersion curve was computed for all 24 panels using the slant stack technique, which is an amplitude plot for each frequency for all velocities. In order to generate a smooth image, the amplitudes for the time samples were summed till zero-crossing. The frequency samples were computed in each zero-crossing. The frequency samples, therefore, were not evenly spaced in the reference and the model dispersion curves. In order to subtract the amplitude of the corresponding dispersion curve of the model data from the reference data, the frequency samples of the model and reference data were interpolated and extrapolated and made same number of samples. The required fitness function for the minimization was the sum of the square of the differences of the corresponding reference and model dispersion curves. The steps

used to compute the fitness function are given below.

7.5 The Fitness Function Developed for Rayleigh Wave Inversion

- Computed the dispersion curves for the front and back shots of the two survey lines for the reference data of the Stellarton field. A numerical model was then developed on the basis of the range of S wave velocities of reference data, which was obtained from the reference dispersion curves. This numerical model tried to mimic the reference data and was the starting guess for the inversion process. Synthetic shot records were generated and the dispersion curves were computed for all four shots of the numerical model.

- Sorted the combined frequency samples of both reference and model dispersion curves in increasing order.

- Interpolated or extrapolated the amplitudes for all velocities in both reference and model dispersion curves for missing frequencies. This constructed the reference and model dispersion curves with identical velocity and frequency samples.

- Computed the fitness function by integrating the square of the difference of the corresponding amplitudes of the reference and the model dispersion curves along the velocity and frequency axes.

$$F = \iint (A_{ref} - A_{mod})^2 \; dv \; df$$

where dv and df are, respectively, velocity and frequency sample. A_{ref} and A_{mod} are, respectively, the amplitude arrays of the reference and model the dispersion curves.

- Summed all the fitness functions obtained from the corresponding panels of the model and reference dispersion curves. The total value of the fitness function was then divided by the number of panels.

7.6 Inversion of Rayleigh Waves Data from Stellarton Site

The detailed review of the VFSR technique for minimization problem is given in Chapter 2 and the pseudo code of the VFSR technique is given in Chapter 3, and will not be repeated here. In this research my new idea is to use the inversion algorithm based on VFSR to invert the Rayleigh waves field data from the Stellarton field by minimizing the fitness function as described in section 7.5.

7.6.1 First Guess Model

A numerical model was developed for minimizing the fitness function contains dipping layers, with mine tunnels going along the strike direction. The model contained 70 parameters, which include structures of the subsurface as well as the material properties of the medium. All the parameters in the first guess model were chosen after a series of experiments on the dipping layered structure with mine tunnels and the material properties of the medium. Six dipping layers were considered in the first guess model with 3 interior points in each layer, each point having two degrees of freedom along the x and z directions. Each layer has a S wave velocity, a P wave velocity, and a density. Four circular anomalies were introduced in the model. Each anomaly had three degrees of freedom along the x, z directions and along the radius. The approximate lateral position of the anomalies in the numerical model were determined from the cross-section of the east boundary of open pit mine. The background structure of the model was kept fixed, and all the material properties, as well as position and size of the anomalies, were updated in each iteration in the inversion until the sum of the square of the difference between the reference and model dispersion curves reached a minimum value. For the first guess, the material properties of the dipping layers, with their upper and lower bounds, are given in Table 7.2. The P wave velocity in each layer was computed from the product of the S wave velocity and the ratio of Vp/Vs where Vp and Vs are, respectively, the P and S wave velocities in m/sec. The material properties of all the anomalies were computed by multiplying the background properties with the factors shown in the second column of Table 7.3.

Layer	Vp/Vs	Up	Lp	Vs	Us	Ls	ρ	U_ρ	L_ρ
1	2.33	1.6	2.5	172	50	400	1.55	0.5	1.9
2	2.40	1.6	2.5	260	50	400	1.60	0.5	1.9
3	1.91	1.6	2.5	227	50	400	1.58	0.5	1.9
4	1.67	1.6	2.5	349	50	400	1.65	0.5	1.9
5	2.12	1.6	2.5	184	50	400	1.29	0.5	1.9
6	2.36	1.6	2.5	255	50	400	1.56	0.5	1.9

Table 7.2: Material properties with the upper and lower bounds for the first guess dipping layer model.

Circle	Vp/Vs/ρ	U	L	x	Ux	Lx	z	Uz	Lz	r	Ur	Lr
1	0.8	0.5	1.0	32.01	28	46	5.53	1	13	4.21	1	8.5
2	0.8	0.5	1.0	56.40	47	72	6.89	1	14	5.16	1	8.5
3	0.8	0.5	1.0	77.25	72	88	9.17	1	16	4.65	1	8.5
4	0.8	0.5	1.0	97.26	87	106	6.40	1	14	5.05	1	9.5

Table 7.3: Material properties of circular anomalies with upper and lower bound which were introduced in the dipping layer model for inversion.

7.7 Results and Analysis of VFSR

The dispersion curves of Rayleigh waves data from Stellarton field were inverted using VFSR as explained in the previous sections. The dispersion curves of reference Rayleigh waves data and the dispersion curves obtained from numerical data, after inversion are respectively given in the Figure 7.6 and Figure 7.7. The vertical axes represents the negative to positive velocity including zero. Horizontal axes represents the frequencies. In order to generate smooth plots of dispersion curves frequencies were averaged to every zero crossings. Hence they are not evenly spaced. Therefore, actual values of velocities and frequencies were not able to provide in the both plots. Six dispersion curves which were computed for each of the four shot for reference and numerical data are seen in both figures. The phase velocity decrease with increase of frequency from down dip to up dip can be observed in the penalized dispersion curves for all four shots of reference and numerical Rayleigh waves data. The optimum cost function 0.61 was obtained after 19843 iterations using VFSR. The plot of the cost function versus number of iterations is given in Figure 7.8. The high value of cost functions with increase number of iterations as shown in Figure 7.8, were accepted

in a probabilistic manner in order to avoid local minimum. The VFSR technique increases the search space of insensitive parameters by increasing the temperature for these parameters. The reference and inverted image of the Stellarton site are given in the Figure 7.9 and Figure 7.10 respectively. The horizontal scale of inverted image is same as the reference one. The vertical scale or depth in the numerical model was considered to 40 meters. These two images are combined and is shown in the Figure 7.11. The top of this Figure represents the reference image of the Stellarton with mine tunnels going along the strike of dipping coal layers and the bottom of the Figure 7.11 represents the image which was obtained after inversion of Rayleigh waves data from the Stellarton site. Three low velocity zones, which are located at 6 to 15 meters, 25 to 35 meters, 72 to 82 meters in the inverted image. All these zones match the low velocity zones present in the geological cross section of the site. The depth of these three low velocity zones are from 3 to 15 meters. It can be observed that horizontal positions as well as depth of the three tunnel in the image after inversion, as shown in the Figure 7.11 approximately match the positions in reference image. From this result it is clear that VFSR technique can be used for inverse modeling to obtain subsurface image with anomalies.

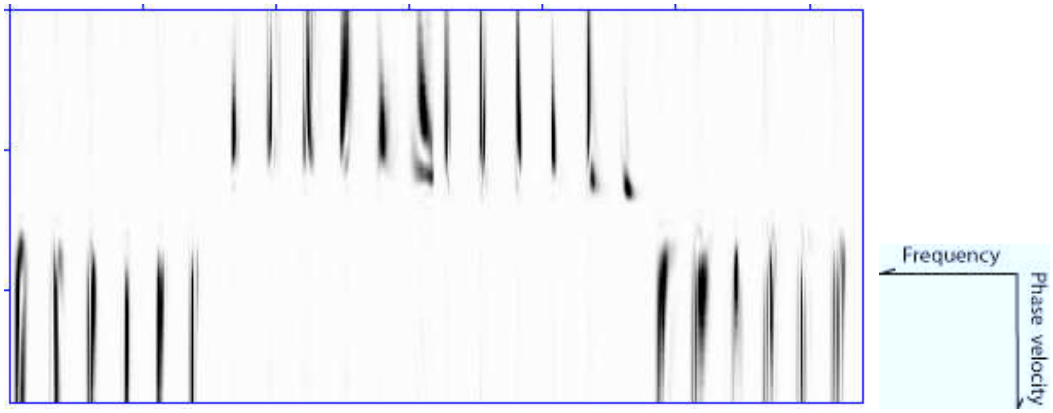

Figure 7.6: Dispersion curves of Rayleigh waves field data.

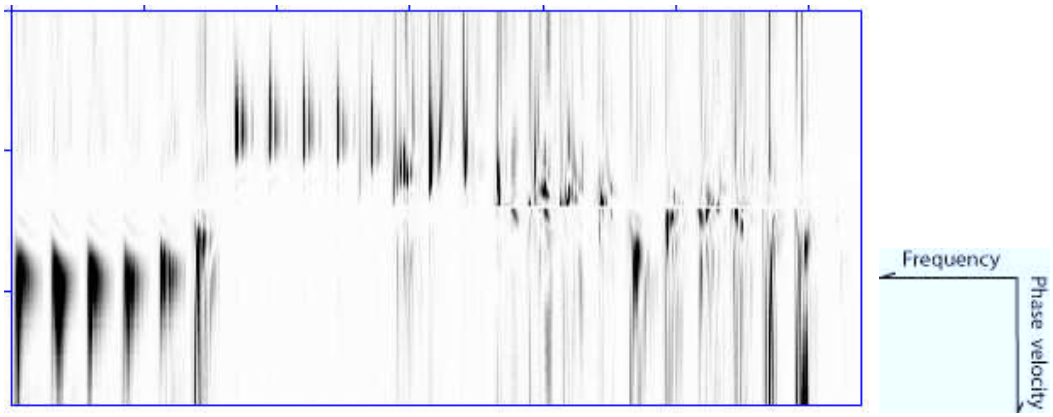

Figure 7.7: Dispersion curves of Rayleigh waves numerical data after 19000 iterations.

7.8 Imaging Issues, Challenges and Expectations

This chapter discussed the successes in imaging Stellarton data using VFSR technique. This random search method optimize the function without converging to a local optimum. Hence the solution obtained using this technique should be a close solution to the reference one. VFSR was tested for the inversion of several known numerical models before it applied to the Stellarton data set. The test results are given in the Appendix B. It was found that this methods works very well when the subsurface structure is known. Therefore VFSR method may break while imaging the subsurface where both geology and anomaly location may be partially known.

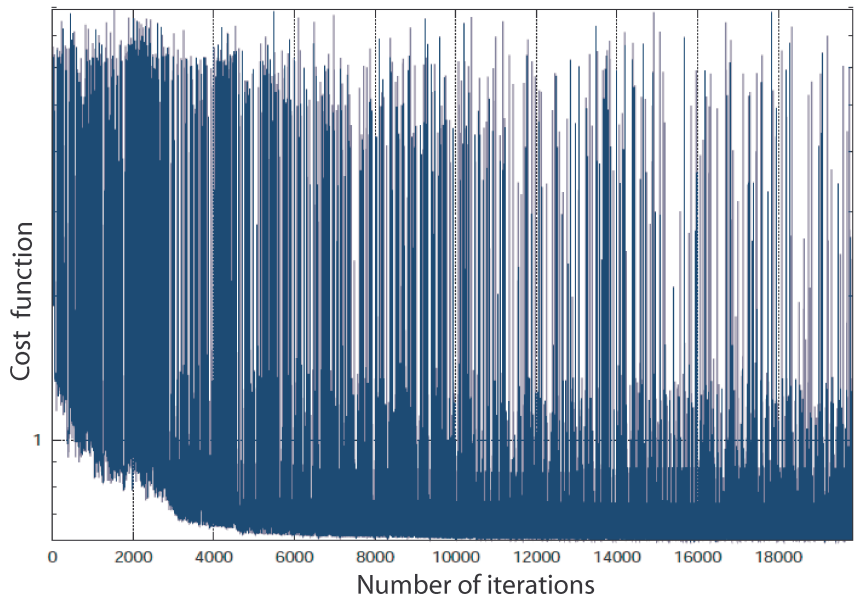

Figure 7.8: Cost functions versus number of iterations.

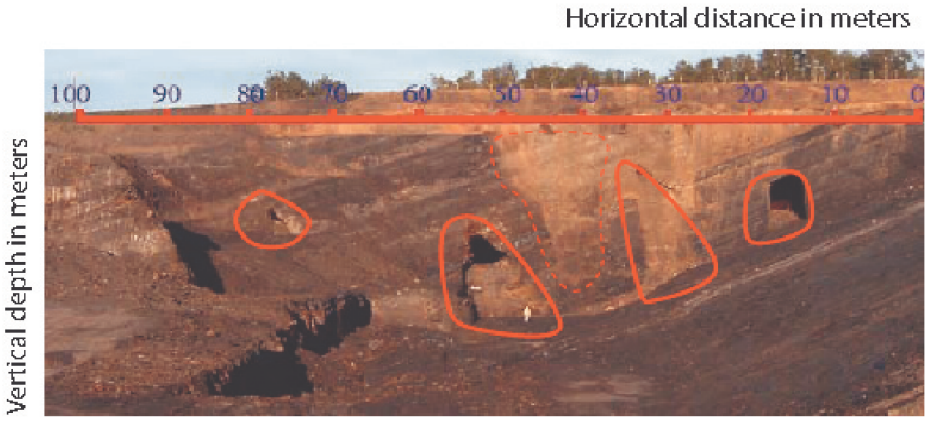

Figure 7.9: Geological cross section of the Stellarton site.

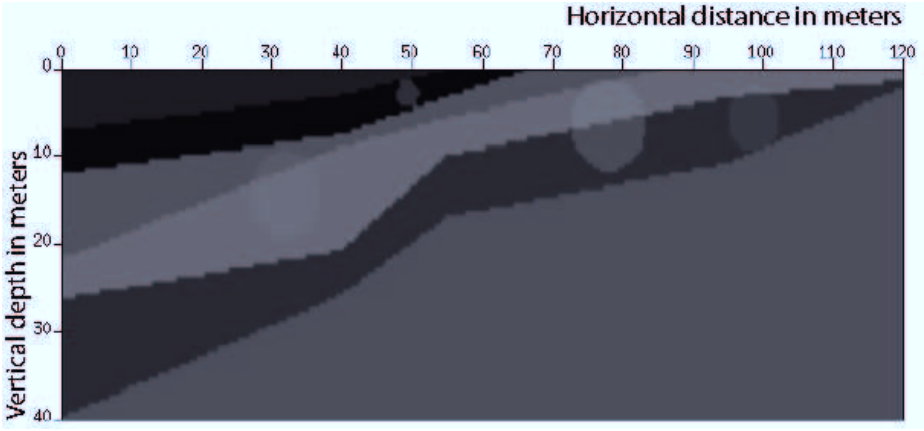

Figure 7.10: Numerically inverted image of Stellarton site.

Figure 7.11: Mine tunnels in Stellarton coal field (top). Subsurface image of Stellarton with mine tunnels obtained after inversion (bottom).

Chapter 8

Conclusions and Future Work

There are many techniques available for near surface imaging but they needs to be improved for better imaging resolution. This research achieved success in developing improved methodology to image near surface with lateral heterogeneity. The methodology of near surface imaging, developed in this research, has generalized the flat layer assumptions into a completely inhomogeneous media. Rayleigh wave data were inverted using VFSR. This chapter will present advantages of the methodology which was developed in this research for imaging laterally inhomogeneous medium. The possible recommendations to improve this technique for future research will also be discussed.

8.1 Conclusions

The summary of conclusion of this research are as follows: Proposed and demonstrated a new technique to detect and locate subsurface anomaly by modeling Rayleigh waves propagating in inhomogeneous or non flat layered models. Numerical modeling involves solution of 2-D elastic wave equation using staggered grid. Partitioned multichannel data into horizontal panels to compute localized dispersion curves. This domain partitioning resolves lateral heterogeneity in the subsurface. A highly non linear optimization method, VFSR was used for Rayleigh waves inverse modeling to retrieve subsurface image of Stellarton mine site of Nova Scotia, Canada.

The research findings are:

- A 2-D finite difference staggered technique was used to model Rayleigh waves by solving elastic wave equation. This staggered grid scheme has advantages of computing different components of velocity and stress at different node points. It was found that, the number of grid points per wavelength to model Rayleigh wave is more than 20.

- A new idea of laterally panelizing multichannel data into a sequence of traces was introduced for localized computation of Rayleigh wave dispersion curve using slant stack technique. The changes in velocity in lateral direction can be studied on Rayleigh wave dispersion curves through the panelization of multichannel data.

- The numerical scheme was used to conduct a series of parametric study to investigate the effect of layer's depth, dip, size and shape of near surface anomalies on Rayleigh wave propagation.

- Rayleigh wave is not dispersive i.e. phase velocity of Rayleigh wave does not depend on frequency when it travels in a homogeneous medium. Hence, the S wave and the Rayleigh wave travel almost with same velocity in a homogeneous medium.

- The phase velocity of Rayleigh wave decreases with an increase of frequency when the velocity increases with depth and the interface is in between one third to one half of a minimum wavelength of Rayleigh wave down from the surface. Rayleigh wave is not dispersive if the interface is at less than one third of a minimum wavelength of Rayleigh wave down from the surface. In this case, the energy of Rayleigh wave travel with the high velocity i.e. the velocity of lower layer.

- The phase velocity of Rayleigh wave increases with an increase of frequency when the velocity decreases with depth and the interface is in between one third to one half of a minimum wavelength of Rayleigh wave down from the surface. Rayleigh wave's phase velocity does not depend on the frequency if the interface is at less than one third of a minimum wavelength of Rayleigh wave down from the surface. The energy of Rayleigh wave travel with the low velocity i.e. the velocity of lower layer.

- The Rayleigh waves phase velocity increases and decreases with the increase of frequency when a softer layer is present in between two stiffer layers and the interface is in between one third to half of a minimum wavelength of Rayleigh

wave down from the surface. The energy traps and reverberates within soft the layer. Higher mode of Rayleigh wave as well as the energy attenuates at particular frequency band which is related to the depth of soft layer when the interface is in between one third to one half of a minimum wavelength of Rayleigh wave.

- Shot records and the dispersion curves computed from the front and back shots are same when subsurface does not contain dipping layer.
- The front and back shot records are different when subsurface contains dipping layer. Rayleigh wave is dispersive in the near offsets for down dip for the front shot and in the far offsets for up dip for the back shot.
- Rayleigh wave dispersion curve does not resolve well in level one, consisting of all traces of multichannel data when subsurface contains dipping layer. Phase velocity versus frequency axis resolve well after paneling the first level into sequence of traces for the computation of dispersion curves in each panel. Rayleigh wave travels more in the high velocity region in extreme up dip and gradually travels to the low velocity region in down dip.
- The velocity slopes in all directions were considered in computing dispersion curves using slant stack while studying the effect of an anomaly on Rayleigh waves dispersion curves. The positive dispersion curve measures the variation of phase velocity with frequency, while negative dispersion curve measures reflected energy from front and rare face of an anomaly.
- When material contrast of an anomaly increases from +25% to +75% from the surrounding, the reflection of P, S and Rayleigh wave increases from the front and rare sides of the anomaly in shot records. The amplitudes in the negative dispersion curve increases when material contrast of the anomaly increases from +25% to +75%.
- When material contrast of an anomaly decrease from -25% to -75% from the surrounding, energy traps inside the anomaly and causes reverberation. Reverberated energy is present in the shot records. Absence of Rayleigh wave

energy at particular frequency in the positive dispersion curves is related to the depth of an anomaly with a very low material contrast from the surrounding. The width of an anomaly can be determined by computing the wavelength of reflected waves from the front and rare face of an anomaly in the negative dispersion curves.

- Effect of material contrast of circular anomaly on Rayleigh wave propagation is similar to the effect of material contrast of rectangular anomaly except, the reflected wave from the circular anomaly is more curved and less linear.

- Reflection from the front and rare face of the anomaly with high material contrast from the surrounding is strong, when it is approximately one fifth to one third of a minimum wavelength of Rayleigh wave down from the surface. Reflection from the anomaly decreases and low frequencies are increasingly reflected when the depth of an anomaly increases upto a wavelength down from the surface.

- The anomaly with very low material contrast and at a depth of one fifth to one third of a minimum wavelength of Rayleigh wave down from the surface traps more energy and reflects more energy than at deeper depth upto a wavelength down from the surface. This is evident in the negative dispersion curves. Attenuation of Rayleigh wave energy at a particular frequency band is related to the depth of an anomaly.

- Reflection from outer and inner face of a circular anomaly of +75% material contrast increases as the radius of the anomaly increase in the shot record. This is evident in the amplitudes of negative dispersion curves. Circular anomaly of -75% material contrast traps more energy as the radius of the anomaly increases. Amplitudes in the negative dispersion curve increases as the radius of the anomaly increase. Energy attenuated at particular frequency band in the positive dispersion curves is related to the depth of an anomaly.

- When the height of a rectangular anomaly of +75% material contrast from the surrounding increases from one fifth to a minimum wavelength of Rayleigh

wave, the reflection from the front and rare side of the anomaly increases. Amplitudes in the negative dispersion curves increases with the increase of height of rectangular anomaly in that case. On the other hand, more energy traps when height of a rectangular anomaly of -75% material contrast from the surrounding increase. Low amplitude zone in the positive dispersion curves move to lower frequency with the increase of height as the lower frequencies are more affected as the height of an anomaly of low material contrast from the surrounding increases.

- As the width of the anomaly of +75% material contrast of the surrounding increases from one fifth to a minimum wavelength of Rayleigh wave, the distance between the reflections of front and rare face of the anomaly increase in the shot records. Anomaly with -75% material contrast of the surrounding traps energy with the increase of width from one fifth to a wavelength of a minimum wavelength of Rayleigh wave.

- As width of the anomaly of +75% material contrast from the surrounding is one fifth and height is a wavelength then strong reflection from the sides of the anomaly is evident in the shot records as well as in the negative dispersion curve

- VFSR was used for the inverse modeling of Rayleigh wave to generate shear wave velocity profile with depth. There were, total of 70 parameters in this inversion. It was not possible to update the structures and material properties of the subsurface together. Hence inversion was carried out in two stages. The first stage iterations were used to fix the structure. In the second stage all material properties, the positions and shape of the anomalies were iterated to obtain minimum cost function.

8.2 Recommendations

The opportunities for further work based on this dissertation include investigating the panel method (a localized domain decomposition), the VFSR technique non-linear optimization method was demonstrated with reference data, use of the new

techniques could be applied to more reference data cases, and clearly extensions into three dimensional near surface seismic surveys are feasible.

The panelizing methods worked well with model data and reference data. The resolution, stability, and extent of the method would benefit from detailed model studies. The current reference data experiments indicate success when subsurface contains dipping layers and/or lateral heterogeneity.

The Rayleigh waves dispersion curve process computed using slant stack algorithm is dependent on the number of traces in each panel, less than 10 directly affects result quality, hence more work in this area is needed.

The complexity of a heterogeneous model and the elastic earth model makes the seismic data fitting problem a highly nonlinear inversion problem which was addressed in this research using VFSR. This inversion method works well in imaging the subsurface of known geological structures and approximate location of anomalies.

VFSR has limitations in inversion if geological structure of the subsurface is not known. More work is needed in VFSR inversion to construct better objective functions for imaging the subsurface for a blind investigation where geology of the subsurface is not known. Further, the use of other non-linear optimization methods applied to this problem could yield better results.

The methodologies used here for near surface imaging was applied to one field data set, and should be applied to other reference field data with known complex subsurface geometry to determine the limits of the technique.

Finally, acquiring and processing 3-D Rayleigh waves data along with 3-D numerical modeling of Rayleigh waves are a logical next step to solve imaging and analysis of shallow subsurface with lateral heterogeneity.

In summary, the MASW, the layered inversion techniques have supplemented with a new and more powerful in-homogeneous seismic surface wave inversion method based on data paneling.

Bibliography

K. Aki and P. Richards. Quantitative seismology, theory and methods. *W.H. Freeman and Co.*, 1980.

N.A. Al-Shayea. *Detection of subsurface cavities by the spectral analysis of surface waves method*. PhD thesis, Civil and Environmental Engineering Department, University of Michigan, 1994.

Z. Alterman and R. Burridge. The elastic radiation from an expanding spherical cavity. *Geophysical Journal of the Royal Astronomical Society*, 30, 1972.

Z. Alterman and F.C. Karal. Propagation of elastic waves in layers media by finite difference methods. *Bulletin of Seismological Society of America*, 58, 1968.

L. Bodet, O. Abraham, A. Birti, D. Leparous, and P. Cote. Effect of dipping layers on seismic surface waves profiling: a numerical study. *Symposium on application of geophysics to engineering and environmental problems*, 2004.

D.M. Boore. Finite-difference methods for seismic wave propagation in heterogeneous materials. *Methods in computational physics II*, 11, 1972.

R.P. Bording. Finite difference modeling: nearly optimal sponge boundary conditions. *Annual Meeting Abstracts, Society of Exploration Geophysicists*, 2004.

K.E. Bullen. An introduction to the theory of seismology. *Cambridge University Press*, 1963.

J. Chen, R.P. Bording, E. Liu, Z. Zhang, and J. Badal. The application of the nearly optimal sponge boundary conditions for seismic wave propagation in poro elastic media. *Journal of Seismic Exploration*, 19, 2010.

S. Foti. *Multistation methods for geotechnical characterization using surface waves*. PhD thesis, Department of Structural and Geotechnical Engineering, Technical University of Turin, 2000.

V. Ganji, N. Gucunski, and A. Maher. Detection of underground obstacles by sasw method - numerical aspects. *Journal of geotechnical and geoenvironmental engineering*, 123, 1997.

C. Gelis, D. Leparoux, J. Virieux, A. Bitri, S. Operto, and G. Grandjean. Numerical modeling of surface waves over shallow cavities. *Journal of environmental and engineering geophysics*, 10(2), 2005.

G. Hevin, O. Abraham, H.A. Pedersen, and M. Campillo. Characterization of surface cracks with rayleigh waves: A numerical model. *NDT and E internat*, 31, 1992.

L.T Ikelle and L. Amundsen. *Introduction to petroleum seismology*. Society of exploration geophysics, Tulsa, USA, 2005.

L. Ingber. Very fast simulated reaaealing. *Mathl. Compute. Modeling*, 12(8), 1989.

L. Ingber. Simulated annealing: practice versus theory. *Statistic and Computing*, 12 (8), 1993.

K.R. Kelly, R.W. Ward, S. Treitel, and R.M. Alford. Synthetic seismograms: a finite difference approach. *Geophysics*, 41(1), 1976.

S. Kirkpatrick, C.D. Gelatt, and M.P. Vecchi. Optimization by simulated annealing. *Science*, 220(4598), 1983.

D. Leparoux, A. Bitri, and G. Grandjean. Underground cavity detection: a new method based on seismic rayleigh waves. *European journal of environmental and engineering geophysics*, 2000.

A.E.H. Love. *Some problems of geodynamics*. 1911.

G.A. McMechan and M.J. Yedlin. Analysis of dispersive wave by wave-field transformation. *Geophysics*, 46(6), 1981.

N. Metropolis, A.W. Rosenbluth, M.N. Resenbluth, and A.H. Teller. Equation of state calculations by fast computing machines. *Journal of Chemical Physics*, 21(6), 1953.

A.N. Moghaddam. *Study of the effect of lateral inhomogeneities on the propagation of Rayleigh waves in an elastic medium*. PhD thesis, Department of Civil Engineering, University of Waterloo, 2006.

S. Nazarian. *In situ determination of elastic moduli of soil deposits and pavement systems by Spectral- Analysis-of-Surface waves method*. PhD thesis, University of Texas at Austin, 1984.

C.B. Park, R.D. Miller, and J. Xia. Multichannel analysis of surface waves. *Geophysics*, 64(3), 1999.

J.W.S. Rayleigh. On waves propagated along the plane surface of an elastic solid. *Proceedings of London Mathematical Society*, 17, 1885.

F.E. Richart, J.R. Hall, and R.D. Woods. Vibrations of soils and foundations. *Prentice-Hall, Inc.*, 1970.

M.K. Sen and P.L. Stoffa. *Global optimization methods in geophysical inversion*. Elsevier Science B.V., The University of Texas at Austin, Institute for Geophysics, U.S.A, second edition, 1995.

S. Sharma, S. Butt, C. Hurich, and P. Bording. Effect of steeply dipping layers on rayleigh wave propagation: A parametric study. *Inaugural International Conference of the Engineering Mechanics Institute*, 2008.

R.E. Sheriff and L.P. Geldart. *Exploration seismology*. Cambridge university press, Houston, USA, second edition, 1998.

K.H. Stokoe, G.W. II, Wright, A.B. James, and M.R. Jose. Characterization of geotechnical sites by sasw method in woods. *R.D., Ed, Geophysical characeterization of sites: Oxford Publ.*, 1994.

J. Virieux. P-sv wave propagation in heterogeneous media: Velocity-stress finite difference method. *Geophysics*, 51(4), 1986.

J. Xia, Y. Xu, and R.D. Miller. Generating an image of dispersive energy by frequency decomposition and slant stacking. *Pure and applied geophysics*, 164, 2007.

C. Xu and S.D. Butt. Evaluation of masw techniques to image steeply dipping cavities in laterally inhomogeneous terrain. *Journal of applied geophysics*, 59, 2006.

Jon C.Q. Xu, S.D. Butt, and P.J.C. Ryall. Seismic rayleigh wave method for localizing and imaging subsurface cavities in various and complicated districts. *Symposium on the application of geophysics to engineering and environmental problems*, 2008.

O. Yilmaz. *Seismic data processing*. Society of Exploration Geophysics, Society of Exploration Geophysics, Tulsa, OK, U.S.A, first edition, 1987.

Appendix A

FORTRAN 90 Source Codes

Source codes for forward and inverse modeling were developed using FORTRAN 95. This appendix contains FORTRAN 95 code for model building, 2-D finite difference solution of elastic wave, slant stack for dispersion curve computation and VFSR inversion.

A.1 Model Building

```
module Modelbuilder
contains
subroutine mdlb(vp0,vs0,den0)
real, intent(in) :: vp0, vs0, den0 !! Background parameters
! implicit none
integer, parameter :: ndpts = 4096
integer, parameter :: ndl = 4096 !! segments and lines
dimension ip1v(ndl),ip2v(ndl)
dimension vpv(ndl),vsv(ndl),dev(ndl)
dimension iptype(ndl)
! = 1 single line segment == line
! = 2 multi-line segment == segment
character*80 line
dimension xzp(2,ndpts)
dimension kxzp(ndpts)
real, allocatable :: vp(:,:)
real, allocatable :: vs(:,:)
real, allocatable :: den(:,:)
integer :: nt, nx, ny, nz
```

```
real :: dt, h, dx, dz, lb, ub
open(17, file="model.dat",form="formatted",status="unknown")
read(17,*) nt
read(17,*) dt
read(17,*) h
read(17,*) nx,ny,nz
close(17)
dx = h
dz = h
xmin = 0.0
zmin = 0.0
xmax = (nx-1)*dx - xmin
zmax = (nz-1)*dz - zmin
open ( 11, file="velline.dat",form="formatted",status="unknown")
ipc = 0
write(6,*) " line inputs "
write(6,*) " Point 1, Point 2, Vp, Vs, Density "
99 continue
read( 11,"(a)",end=100) line
write(6,"(a)") line(1:4)
if( line(1:4) .eq. "Line" ) then
itype = 1
go to 99
endif
if( line(1:4) .eq. "line" ) then
itype = 1
go to 99
endif
if( line(1:4) .eq. "Segm" ) then
itype = 2
```

```
go to 99
endif
if( line(1:4) .eq. "segm" ) then
itype = 2
go to 99
endif
read(line,*) ip1,ip2,vpl,vsl,denl
write( 6, *) ip1,ip2,vpl,vsl,denl
ipc = ipc + 1
iptype(ipc) = itype
ip1v(ipc) = ip1
ip2v(ipc) = ip2
vpv(ipc) = vpl
vsv(ipc) = vsl
dev(ipc) = denl
go to 99
100 continue
npc = ipc
close(11)
kxzp = 0
open ( 11, file="velpts.dat",form="formatted",status="unknown")
read( 11, *) xp_scale,zp_scale
write( 6, *) " x,z scale ",xp_scale,zp_scale
98 continue
read( 11,*,end=101) ixzp,xp,zp
kxzp(ixzp) = 1
xzp(1,ixzp) = xp*xp_scale
xzp(2,ixzp) = zp*zp_scale
if( xzp(1,ixzp) .lt. xmin ) xzp(1,ixzp) = xmin
if( xzp(1,ixzp) .gt. xmax ) xzp(1,ixzp) = xmax
```

```
!if( xzp(2,ixzp) .lt. zmi n ) xzp(2,ixzp) = zmin
!if( xzp(2,ixzp) .gt. zmax ) xzp(2,ixzp) = zmax
!!write( 6, *) " grid point number, x,z ", ixzp,xp,zp,xzp(1,ixzp),xzp(2,ixzp)
go to 98
101 continue
close(11)
allocate(vp(nx,nz))
allocate(vs(nx,nz))
allocate(den(nx,nz))
vp = vp0
vs = vs0
den = den0
do ipc=1,npc
ip1a = ip1v(ipc)
ip2a = ip2v(ipc)
if( ip1a .gt. ip2a ) then
ittp = ip1a
ip1a = ip2a
ip2a = ittp
endif
if( kxzp(ip1a) .eq. 1 ) then
if( kxzp(ip2a) .eq. 1 ) then
if( iptype(ipc) .eq. 1 ) then
kip = ip2a-ip1a
endif
if( iptype(ipc) .eq. 2 ) then
kip = 1
endif
write(6,*) ip1a,ip2a,kip
do ip1=ip1a,ip2a,kip
```

```
if( ip1 .ne. ip2a ) then
if( iptype(ipc) .eq. 1 ) then
ip2 = ip1+kip
endif
if( iptype(ipc) .eq. 2 ) then
ip2 = ip1 + 1
endif
xa = xzp(1,ip1)
za = xzp(2,ip1)
xb = xzp(1,ip2)
zb = xzp(2,ip2)
write(6,*) xa,za,xb,zb
if( xb .lt. xa ) then
xt = xa
xa = xb
xb = xt
zt = za
za = zb
zb = zt
endif
ia = (xa-dx)/dx
ib = (xb+dx)/dx
if( ia .lt. 1 ) ia = 1
if( ib .gt. nx ) ib = nx
do i = ia,ib
xxp = (i-1)*dx + xmin
if( xxp .ge. xa ) then
if( xxp .le. xb ) then
amu = (xxp-xa)/(xb-xa)
zzp = za + amu*(zb-za)
```

```
ja = (zzp-2.0*dz)/dz
if( ja .lt. 1 ) ja = 1
jb = nz
do j = ja,jb
zpz = (j-1)*dz + zmin
if( zpz .ge. zzp ) then
vp(i,j) = vpv(ipc)
vs(i,j) = vsv(ipc)
den(i,j) = dev(ipc)
endif
enddo
endif
endif
enddo
endif
enddo
else
write(6,*) " error p1 or p2 is bad ",ip1,ip2
endif
endif
enddo
!! Write parameters to vp.dat, vs.dat and den.dat
nrecl = nx*nz*4
open ( 20, file="vp.dat",form="unformatted", &
access="direct",status="unknown",recl=nrecl)
write(20,rec=1) ((vp(i,j),j=1,nz),i=1,nx)
close(20)
write(6,*) " vp.dat, vs.dat and den.dat are ",nx," by ",nz
nrecl = nx*nz*4
open ( 20, file="vs.dat",form="unformatted", &
```

```
access="direct",status="unknown",recl=nrecl)
write(20,rec=1) ((vs(i,j),j=1,nz),i=1,nx)
close(20)
nrecl = nx*nz*4
open ( 20, file="den.dat",form="unformatted",&
access="direct",status="unknown",recl=nrecl)
write(20,rec=1) ((den(i,j),j=1,nz),i=1,nx)
close(20)
deallocate(vp)
deallocate(vs)
deallocate(den)
end subroutine mdlb
end module Modelbuilder
```

A.2 2-D Finite Difference Approximation of Elastic Wave Equation

```
module Elastic2D
use PDE_Wave
implicit none
private
real(prec), pointer :: vx(:,:) !! Velocity in x-direction
real(prec), pointer :: vz(:,:) !! Velocity in z-direction
real(prec), pointer :: txx(:,:) !! Stress tensor
real(prec), pointer :: tzz(:,:) !! Stress tensor
real(prec), pointer :: txz(:,:) !! Stress tensor
real(prec), pointer :: vp(:,: !! P-wave velocity
real(prec), pointer :: vs(:,:) !! S-wave velocity
real(prec), pointer :: lambda(:,:) !! Elastic param
real(prec), pointer :: mu(:,:) !! Elastic param
real(prec), pointer :: den(:,:) !! Density
real(prec), pointer :: bou(:,:) !! Bouyancy : 1/density
```

```
real(prec), pointer :: mem(:,:) !! Storage for movie loop real(prec) :: vmin, vmax,
cflmax !! Min, max velocity and max cfl
integer :: ileft, iright, ktop, kbottom !! Expanding grid bounds
integer :: movieframe
integer, parameter :: timestride = 4 !! Save results at receivers with stride
real(sprec), allocatable :: vxbuf(:,:) !! Sample buffer
real(sprec), allocatable :: vzbuf(:,:) !! Sample buffer
integer :: nsampletot, nbuf, nsample
public :: solve
contains
subroutine solve
integer :: it, is
real(prec) :: xshot, zshot
write (6,*) "Serial Elastic 2D solver"
call solver_init
do is = 1, tot_num_shot
isrc = ishot(is)
ksrc = kshot(is)
xshot = (isrc-1)*h
zshot = (ksrc-1)*h
write(6,"(A,I5,A,I5)") " Shot point ", is, " of ", tot_num_shot
write(6,"(A,F14.4,F14.4)") " Shot point location ",xshot,zshot
write(6,"(A,I5,I5)") " Shot point index ",isrc,ksrc
var_memory = zero !! Put all variables to zero
nsample = 0
do it = 1, nt
!! Compute expanding grid bounds
ileft = max(int(isrc-cflmax*(it-1)),1-abc_width)
iright = min(int(isrc+cflmax*(it-1)+1),nx+abc_width)
ktop = max(int(ksrc-cflmax*(it-1)),1)
kbottom = min(int(ksrc+cflmax*(it-1)+1),nz+abc_width)
```

```
if( mod(it,20000) .eq. 0 ) then
write(6,"(I5,A,I5,A)") it," of ",nt," time steps"
endif
!! call time stepper
call time_step(source(it),vx,vz,txx,tzz,txz,bou,lambda,mu, &
nx, nz, abc_width+1, ileft, iright, ktop, kbottom)
!! Write to files
call write_files(vx,vz,mem,nx,nz,abc_width+1,it)
end do
call solver_post(is)
end do
call pde_wave_post
deallocate(vxbuf,vzbuf)
close(81) !! Elastic_movie.bin
close(83) !! vx_seismic.bin
close(84) !! vz_seismic.bin
end subroutine solve
subroutine solver_init
integer :: nrecl !! frame record length
integer :: bw !! boundary width
call pde_wave_init
ny = 1
bw = abc_width+1
allocate(var_memory(1-bw:nx+bw,1,1:nz+bw,6))
var_memory = zero
vx ⇒ var_memory(:,1,:,1)
vz ⇒ var_memory(:,1,:,2)
txx ⇒ var_memory(:,1,:,3)
tzz ⇒ var_memory(:,1,:,4)
txz ⇒ var_memory(:,1,:,5)
mem ⇒ var_memory(:,1,:,6)
```

```
allocate(par_memory(1-bw:nx+bw,1,1:nz+bw,3))
par_memory = zero
vp ⇒ par_memory(:,1,:,1)
vs ⇒ par_memory(:,1,:,2)
den ⇒ par_memory(:,1,:,3)
lambda ⇒ vp
mu ⇒ vs
bou ⇒ den
call compute_source_function
call read_parameters(vp,vs,den,nx,nz,bw)
vmin = minval(vs)
vmax = maxval(vp)
mu = vs*vs*den
lambda = vp*vp*den-two*mu
bou = 1/den
nullify(vp,vs,den)
cflmax = vmax*dt/h
write(6,*) " V min is ", vmin
write(6,*) " V max is ", vmax write(6,*) " gridpts/wavelength = ", vmin/(fmax*h)
write(6,*) " CFL number = ", cflmax
open(81,file="elastic_movie.bin",form="unformatted", &
access="direct", recl=4*(nx+2*bw)*(nz+bw))
movieframe = 0
print *, 'movie frame is ', nx+2*abc_width+2, nz+abc_width+1
nrecl = 4*nt/timestride
open(83,file="vx_seismic.bin",form="unformatted", &
access="direct", recl=nrecl)
open(84,file="vz_seismic.bin",form="unformatted", &
access="direct", recl=nrecl)
allocate(vxbuf(nt/timestride,tot_num_recv))
allocate(vzbuf(nt/timestride,tot_num_recv))
```

```
end subroutine solver_init
subroutine read_parameters(vp,vs,den,nx,nz,bw)
real(prec), intent(inout) :: vp(1-bw:nx+bw,1:nz+bw)
real(prec), intent(inout) :: vs(1-bw:nx+bw,1:nz+bw)
real(prec), intent(inout) :: den(1-bw:nx+bw,1:nz+bw)
integer, intent(in) :: nx, nz, bw
integer :: nrecl, i, k, frame
real(sprec) tmp(nz)
!! Read p-wave velocities
nrecl=nz*sprec
open(11,file="vp.dat",form="unformatted", &
access="direct",status="unknown",recl=nrecl)
frame=0
do i = 1, nx
frame=frame+1
read(11,rec=frame) (tmp(k),k=1,nz)
vp(i,:) = tmp
enddo
close(11)
open(12,file="vs.dat",form="unformatted", &
access="direct",status="unknown",recl=nrecl)
frame=0
do i = 1, nx
frame=frame+1
read(12,rec=frame) (tmp(k),k=1,nz)
vs(i,:) = tmp
enddo
close(12)
open(13,file="den.dat",form="unformatted", &
access="direct",status="unknown",recl=nrecl)
frame=0
```

```
do i = 1, nx
frame=frame+1
read(13,rec=frame) (tmp(k),k=1,nz)
den(i,:) = tmp
enddo
close(13)
call parameter_continuation(vp, nx,nz,bw)
call parameter_continuation(vs, nx,nz,bw)
call parameter_continuation(den,nx,nz,bw)
end subroutine read_parameters
subroutine parameter_continuation(vec,nx,nz,bw)
real(prec), intent(inout) :: vec(1-bw:nx+bw,1:nz+bw)
integer, intent(in) :: nx, nz, bw
integer :: i, k
do k = 1, nz
vec(1-bw:0,k) = vec(1,k)
vec(nx+1:nx+bw,k) = vec(nx,k)
end do
do i = 1, nx
vec(i,nz+1:nz+bw) = vec(i,nz)
end do
vec(1-bw:0,nz+1:nz+bw) = vec(1,nz)
vec(nx+1:nx+bw,nz+1:nz+bw) = vec(nx,nz)
end subroutine parameter_continuation
subroutine write_param_cont(vec,bw,str,nstr)
real(prec), intent(in) :: vec(1-bw:nx+bw,1:nz+bw)
integer, intent(in) :: bw
character*80, intent(in) :: str
integer, intent(in) :: nstr
integer :: nrecl, frame, i
nrecl = 4*(nz+bw)
```

```
open(21,file=str(1:nstr),form="unformatted",&
access="direct",status="unknown",recl=nrecl)
frame = 0
do i = 1-bw, nx+bw
frame = frame+1
write(21,rec=frame) real(vec(i,:),4)
end do
close(21)
end subroutine write_param_cont
!! Dt vx = b * (Dx txx + Dz txz)
!! Dt vz = b * (Dx txz + Dz tzz)
!! Dt txx = (lambda+2*mu) * Dx vx + lambda * Dz vz
!! Dt tzz = lambda * Dx vx + (lambda+2*mu) * Dz vz
!! Dt txz = mu * (Dz vx + Dx vz)
!! with Dt = d/dt, Dx = d/dx and Dz = d/dz
!! in the different variables are evaluated at locations:
!! vx: (xi,zk,tn) ¡=¿ ((i-1/2)*h,(k-3/2)*h, n*dt)
!! vz: (xi,zk,tn) ¡=¿ ( (i-1)*h, (k-1)*h, n*dt)
!! txx: (xi,zk,tn) ¡=¿ ( (i-1)*h,(k-3/2)*h,(n+1/2)*dt)
!! tzz: (xi,zk,tn) ¡=¿ ( (i-1)*h,(k-3/2)*h,(n+1/2)*dt)
!! txz: (xi,zk,tn) ¡=¿ ((i-1/2)*h, (k-1)*h,(n+1/2)*dt)
!! Stress free surface boundary condition, txz=tzz=0 at z=0
!! txz(i,1,n) = 0
!! (tzz(i,1,n)+tzz(i,2,n))/2 = 0
!! vx(i,1,n), txx(i,1,n) never used in stencil
!! vz(i,1,n) is computed by the stencil
subroutine time_step(srcval,vx,vz,txx,tzz,txz,bb,lambda,mu, &
nx, nz, bw, ileft, iright, ktop, kbottom)
integer, intent(in) :: nx,nz,bw,ileft,iright,ktop,kbottom
real(prec), intent(inout) :: vx(1-bw:nx+bw,1:nz+bw)
real(prec), intent(inout) :: vz(1-bw:nx+bw,1:nz+bw)
```

```
real(prec), intent(inout) :: txx(1-bw:nx+bw,1:nz+bw)
real(prec), intent(inout) :: tzz(1-bw:nx+bw,1:nz+bw)
real(prec), intent(inout) :: txz(1-bw:nx+bw,1:nz+bw)
real(prec), intent(in) :: bb(1-bw:nx+bw,1:nz+bw)
real(prec), intent(in) :: lambda(1-bw:nx+bw,1:nz+bw)
real(prec), intent(in) :: mu(1-bw:nx+bw,1:nz+bw)
real(prec), intent(in) :: srcval
! 2nd order staggered grid
real(prec) :: ptxx, ptxz, ptzz, pvxx, pvxz, pvzz, pvzx, pl2mu
integer :: i, k
real(prec) :: dthh
real(prec) :: alpha
alpha = dt/h
dthh = dt/(h*h)
!! Update vx
do k = max(ktop,2), kbottom
do i = ileft, iright
ptxx = (txx(i+1,k)-txx(i,k))
ptxz = (txz(i,k)-txz(i,k-1))
vx(i,k) = vx(i,k)+alpha*0.25 * &
(bb(i,k)+bb(i+1,k)+bb(i,k-1)+bb(i+1,k-1))*(ptxx+ptxz)
enddo
enddo
!! Add source function
vx(isrc,ksrc) = vx(isrc,ksrc) + 0.25*dthh*srcval
vx(isrc,ksrc+1) = vx(isrc,ksrc+1) + 0.25*dthh*srcval
vx(isrc-1,ksrc+1) = vx(isrc-1,ksrc+1) + 0.25*dthh*srcval
vx(isrc-1,ksrc) = vx(isrc-1,ksrc) + 0.25*dthh*srcval
!! Update vz
do k = ktop,kbottom
do i = ileft, iright
```

```
ptxz = (txz(i,k)-txz(i-1,k))
ptzz = (tzz(i,k+1)-tzz(i,k))
vz(i,k) = vz(i,k)+alpha*bb(i,k)*(ptxz+ptzz)
enddo
enddo
!! Add source function
vz(isrc,ksrc) = vz(isrc,ksrc) + dthh*srcval
! Update txx and tzz
do k = max(ktop,2),kbottom
do i = ileft, iright
pl2mu = half*(lambda(i,k)+two*mu(i,k)+lambda(i,k-1)+two*mu(i,k-1))
pvxx = (vx(i,k)-vx(i-1,k))
pvzz = (vz(i,k)-vz(i,k-1))
txx(i,k) = txx(i,k)+alpha*pl2mu*pvxx+alpha*lambda(i,k)*pvzz
tzz(i,k) = tzz(i,k)+alpha*pl2mu*pvzz+alpha*lambda(i,k)*pvxx
enddo
enddo
!! Surface boundary
tzz(:,1) = -tzz(:,2) ! 2nd order
txz(:,1) = 0.0 ! Could prob. be removed when things work
do k = max(ktop,2),kbottom
do i = ileft, iright
pvzx = (vz(i+1,k)-vz(i,k))
pvxz = (vx(i,k+1)-vx(i,k))
txz(i,k) = txz(i,k)+0.5*(mu(i,k)+mu(i+1,k))*alpha*(pvxz+pvzx)
enddo
enddo
call sponge2Del(5)
end subroutine time_step
subroutine write_files(vx,vz,mem,nx,nz,bw,it)
integer, intent(in) :: nx,nz,bw
```

```
real(prec), intent(in) :: vx(1-bw:nx+bw,1:nz+bw)
real(prec), intent(in) :: vz(1-bw:nx+bw,1:nz+bw)
real(prec), intent(out):: mem(1-bw:nx+bw,1:nz+bw)
integer, intent(in) :: it
real(sprec) :: umax
integer :: i, k
if (mod(it,movieloop_cnt) .eq. 0) then
mem = sqrt(vx**2+vz**2)
umax = max(maxval(mem),0.000001)
mem = mem / umax
movieframe = movieframe + 1
write(81,rec=movieframe) ((real(mem(i,k),4), &
k=1,nz+bw),i=1-bw,nx+bw)
end if if (mod(it,timestride) .eq. 0) then
nsample = nsample + 1
do i = 1, tot_num_recv
vxbuf(nsample,i) = real(vx(irecv(i),krecv(i)),4)
vzbuf(nsample,i) = real(vz(irecv(i),krecv(i)),4)
end do
end if
end subroutine write_files
subroutine solver_post(is)
integer, intent(in) :: is
integer :: nrecl,i,k
nrecl = nt/timestride
!!print *, '#samples ', nrecl, ' #recv ', tot_num_recv
do i = 1, tot_num_recv
write (83,rec=(is-1)*tot_num_recv+i) (vxbuf(k,i),k=1,nrecl)
write (84,rec=(is-1)*tot_num_recv+i) (vzbuf(k,i),k=1,nrecl)
end do
end subroutine solver_post
```

```
subroutine sponge2Del(nvar) integer, intent(in) :: nvar !! #variables to sponge out
integer :: i
real(prec) :: weight, w
w = -abc_weight/(abc_width*abc_width)
do i = 1, abc_width
weight = exp(w*i*i)
var_memory(1-i,:,:,1:nvar) = weight*var_memory(1-i,:,:,1:nvar)
var_memory(nx+i,:,:,1:nvar) = weight*var_memory(nx+i,:,:,1:nvar)
var_memory(:,:,nz+i,1:nvar) = weight*var_memory(:,:,nz+i,1:nvar)
end do
end subroutine sponge2Del
end module Elastic2D
```

A.3 Model Update

```
module Inversion
use Modelbuilder
implicit none
private
integer, parameter :: prec = 8
real(prec), parameter :: one=1.0_prec,two=2.0_prec,three=3.0_prec
real(prec), parameter :: zero=0.0_prec,half=0.5_prec
real(prec) :: xmax, zmax, h, dt
integer :: nx, ny, nz
real(prec) :: lbvp, ubvp, lbnu, ubnu, lbaa, ubaa
real(prec) :: stablimit = 0.65_prec
real(prec), allocatable :: LB0(:), UB0(:)
public :: read_param, update_param
contains
subroutine read_param(X,LB,UB,LB0,UB0,T,DX,C,n)
real(8), intent(inout) :: X(:),LB(:),UB(:),LB0(:),UB0(:),T(:),DX(:),C(:)
```

```
integer, intent(in) :: n
integer :: i,nobj,j,ilast
integer, parameter :: zero = 0.0D0
character*100 :: str
character*100 :: strtmp
X = zero
LB = zero
UB = zero
LB0 = zero
UB0 = zero
T = zero
DX = zero
C = zero
call inversion_init
open(10, file="inversion.dat", form="formatted",&
status="unknown")
read(10,*) nobj
ilast = 0
do i=1,nobj
read(10,"(a)") str
if (str(1:13) .eq. "layered_media") then
call read_layered_media(str,X,LB,UB,LB0,UB0,T,DX,C,ilast)
else if (str(1:6) .eq. "circle") then
call read_circle(X,LB,UB,LB0,UB0,T,DX,C,ilast)
else
print *, 'Not found', str
stop
end if
end do
close(10)
end subroutine read_param
```

```
subroutine update_param(X,LB,UB,LB0,UB0,n)
real(8), intent(inout) :: X(:)
real(8), intent(inout) :: LB(:)
real(8), intent(inout) :: UB(:)
real(8), intent(in) :: LB0(:)
real(8), intent(in) :: UB0(:)
integer, intent(in) :: n
character*100 :: str
integer :: nobj, ilast
integer :: j,ii
call inversion_init
open(10, file="inversion.dat", form="formatted",&
status="unknown")
read(10,*) nobj
ilast = 0
do j = 1, nobj
read(10,"(a)") str !! Assume only one background "object"
if (str(1:13) .eq. "layered_media") then
call update_layered_media(str,X,LB,UB,LB0,UB0,ilast)
else if (str(1:6) .eq. "circle") then
call update_circle(X,LB,UB,ilast)
else
print *, 'Not found', str(1:10)
stop
end if
end do
LB = max(LB,LB0)
UB = min(UB,UB0)
close(10) end subroutine update_param
subroutine sort(vec)
real(8), intent(inout) :: vec(:)
```

```
integer :: n
integer :: i, j
real(8) :: tmp
n = size(vec)
do j = n-1,1,-1
do i = 1, j
if (vec(i+1) ¡ vec(i)) then
tmp = vec(i)
vec(i) = vec(i+1)
vec(i+1) = tmp
end if
end do
end do
end subroutine sort
subroutine inversion_init
logical, save :: first = .true.
integer :: nt
if (.not. first) return
first = .false.
open(11, file="model.dat", form="formatted",&
status="unknown")
read(11,*) nt
read(11,*) dt
read(11,*) h
read(11,*) nx,ny,nz
close(11)
xmax = (nx-1)*h
zmax = (nz-1)*h
end subroutine inversion_init
subroutine read_layered_media(str,X,LB,UB,LB0,UB0,T,DX,C,ilast)
character*100, intent(in) :: str
```

```
real(prec), target, intent(inout) :: X(:)
real(prec), target, intent(inout) :: LB(:)
real(prec), target, intent(inout) :: UB(:)
real(prec), target, intent(inout) :: LB0(:)
real(prec), target, intent(inout) :: UB0(:)
real(prec), target, intent(inout) :: T(:)
real(prec), target, intent(inout) :: DX(:)
real(prec), target, intent(inout) :: C(:)
integer, intent(inout) :: ilast
integer :: ix,iz,ivp,inu,iaa,j,i
integer :: nc, nl !! #columns, #layers
character*100 :: strtmp
real(prec) :: line(100), vmax
real(prec), pointer :: xpoint(:), zpoint(:), vp(:), nu(:), aa(:)
call system("cat inversion.dat")
read(str,*), strtmp,nc,nl
ix = ilast
iz = ix+nc-2
ivp = iz+nc*nl
inu = ivp+nl+1
iaa = inu+nl+1
ilast = ilast+(nl+1)*(nc+3)-2
do i = ix+1, ilast
read(10,*) X(i), LB0(i), UB0(i), T(i), DX(i), C(i)
end do
LB(ix+1:ilast) = LB0(ix+1:ilast)
UB(ix+1:ilast) = UB0(ix+1:ilast)
end subroutine read_layered_media
subroutine update_layered_media(str,X,LB,UB,LB0,UB0,ilast)
character*100, intent(inout) :: str
real(prec), target, intent(inout) :: X(:)
```

```
real(prec), target, intent(inout) :: LB(:)
real(prec), target, intent(inout) :: UB(:)
real(prec), target, intent(in) :: LB0(:)
real(prec), target, intent(in) :: UB0(:)
integer, intent(inout) :: ilast
character*100 :: str2
integer :: nc, nl, cnt, i, j, ii
real(prec) :: vp, vs, rho
integer :: ix,iz,ivp,inu,iaa
read(str,*) str2, nc, nl
ix = ilast
iz = ix+nc-2
ivp = iz+nc*nl
inu = ivp+nl+1
iaa = inu+nl+1
ilast = iaa+nl+1
do j = ix+1, ilast !! Read dummy to get to next object
read(10,*) str
end do
call sort(X(ix+1:iz))
do j = 1, nc
call sort(X(iz+j:ivp:nc))
end do
open(12, file="velpts.dat", form="formatted", &
status="unknown")
write(12,*) 1.0D0, 1.0D0
cnt = 1
write(12,*) cnt, 0.0D0, 0.0D0
do i = 1, nc-2
cnt = cnt+1
write(12,*) cnt, X(ix+i), 0.0D0
```

```
end do
cnt = cnt+1
write(12,*) cnt, xmax, 0.0D0
do j = 1, nl
cnt = cnt + 1
write(12,*) cnt, 0.0D0, X(iz+(j-1)*nc+1)
do i = 2, nc-1
cnt = cnt + 1
write(12,*) cnt, X(ix+i-1), X(iz+(j-1)*nc+i)
end do
cnt = cnt + 1
write(12,*) cnt, xmax, X(iz+(j-1)*nc+nc)
enddo
close(12)
open(13, file="velline.dat", form="formatted",&
status="unknown")
do j = 1, nl+1
vs = X(inu+j) !! Back to the original param
vp = X(ivp+j)*vs
rho = X(iaa+j) !! Back to the original param
write(13,"(A)") 'segment'
write(13,"(I4,I4,F23.15,F23.15,F23.15)") (j-1)*nc+1,j*nc,vp,vs,rho
end do
close(13)
call mdlb(100.0,100.0,1.0)
end subroutine update_layered_media
subroutine read_circle(X,LB,UB,LB0,UB0,T,DX,C,ilast)
real(prec), intent(inout) :: X(:)
real(prec), intent(inout) :: LB(:)
real(prec), intent(inout) :: UB(:)
real(prec), intent(inout) :: LB0(:)
```

```
real(prec), intent(inout) :: UB0(:)
real(prec), intent(inout) :: T(:)
real(prec), intent(inout) :: DX(:)
real(prec), intent(inout) :: C(:)
integer, intent(inout) :: ilast
real(prec) :: lbvp, ubvp, lbvs, ubvs, lbden, ubden, ubradius
real(prec) :: xx, zz, rr, vp, vs, den
integer :: i
!! Read parameter bounds
do i = ilast+1, ilast+6
read(10,*) X(i), LB0(i), UB0(i), T(i), DX(i), C(i)
end do
LB(ilast+1:ilast+6) = LB0(ilast+1:ilast+6)
UB(ilast+1:ilast+6) = UB0(ilast+1:ilast+6)
ilast = ilast + 6
end subroutine read_circle
subroutine update_circle(X,LB,UB,ilast)
real(prec), intent(in) :: X(:)
real(prec), intent(in) :: LB(:)
real(prec), intent(in) :: UB(:)
integer, intent(inout) :: ilast
character*100 :: str
integer :: i, k, nrecl
real(4), allocatable :: velp(:), vels(:), dens(:)
real(prec) :: xx, zz, rr, vp_perc, vs_perc, rho_perc, rho,vs
integer :: imin, imax, kmin, kmax
do i = 1, 6
read(10,*) str
end do
xx = X(ilast+1)
zz = X(ilast+2)
```

```
rr = X(ilast+3)
vp_perc = X(ilast+4)
vs_perc = X(ilast+5)
rho_perc = X(ilast+6)
imin = (xx-rr)/h
imax = (xx+rr)/h+2
kmin = (zz)/h
kmax = (zz+2*rr)/h+2
imin = max(imin,1)
imax = min(imax,nx)
kmin = max(kmin,1)
kmax = min(kmax,nz)
allocate(velp(nz),vels(nz),dens(nz))
nrecl=nz*4
open(94,file="vp.dat",form="unformatted", &
access="direct",status="unknown",recl=nrecl)
open(95,file="vs.dat",form="unformatted", &
access="direct",status="unknown",recl=nrecl)
open(96,file="den.dat",form="unformatted", &
access="direct",status="unknown",recl=nrecl)
do i = imin, imax
read(94,rec=i) (velp(k),k=1,nz)
read(95,rec=i) (vels(k),k=1,nz)
read(96,rec=i) (dens(k),k=1,nz)
do k = kmin, kmax
if (((i-1)*h-xx)**2 + ((k-1)*h-zz-rr)**2 .le. rr**2 ) then
velp(k) = vp_perc * velp(k)
vels(k) = vs_perc * vels(k)
dens(k) = rho_perc * dens(k)
end if
end do
```

```
write(94,rec=i) (velp(k),k=1,nz)
write(95,rec=i) (vels(k),k=1,nz)
write(96,rec=i) (dens(k),k=1,nz)
end do
close(94)
close(95)
close(96)
deallocate(velp,vels,dens)
ilast = ilast + 6
end subroutine update_circle
end module Inversion
```

A.4 Slant Stack

```
module Slantstack
implicit none
private
integer :: nsamp, tsamp, nsweep, nv, nf, nshot, nrecv
integer :: ishot, irecv, iii
real(8) :: tmax, dt, fmin, fmax, vmin, vmax
real(8), allocatable :: time_velocity_vec(:,:)
real(8), allocatable :: time_amplitude_vec(:,:), freq(:)
integer, allocatable :: min_trace(:)
integer, allocatable :: max_trace(:)
real(8), allocatable :: shotloc(:,:), recvloc(:,:)
integer, parameter :: sample_stride = 1
real(8), allocatable :: sweep(:) !! sweep source trace
real(4), allocatable :: vz(:,:)
real(8), allocatable :: array_block (:,:)
public :: slantstack_run, slantstack_final
contains
```

```
subroutine slantstack_run(vmin_in,vmax_in,nv_in,nf_out,ndisp,nfreq)
real(8), intent(in) :: vmin_in, vmax_in
integer, intent(in) :: nv_in
integer, intent(out) :: nf_out
integer, intent(in) :: ndisp !! Tot num of disp curves
integer, intent(inout) :: nfreq(ndisp)
integer i, j,n,l,ipanel,maxpanel,npanel
integer nrecl
real(8) summ, tmp1, tmp2
logical, save :: first_time = .true.
vmin = vmin_in
vmax = vmax_in
nv = nv_in
iii = 0
open (32, file = "amplitudes.bin", form = "unformatted", &
access="direct",status = "unknown",recl=4*(2*nv+1))
if (first_time) then
open (83, file="slantstack.dat", form="formatted",&
status="unknown")
read(83,*)nrecv !! # receivers
read(83,*)tsamp !! # seismic samples
read(83,*)nsweep !! # sweep samples
read(83,*)tmax !! max time
read(83,*)dt !! dt
read(83,*)fmin !! fmin
read(83,*)fmax !! fmax
close(83)
nsamp = tsamp+nsweep-1
allocate(sweep(nsweep))
allocate(vz(tsamp,nrecv)) !! vertical velocity
allocate(array_block(nsamp/sample_stride,nrecv))
```

```
allocate(time_velocity_vec(-nv:nv,nsamp/sample_stride))
allocate(time_amplitude_vec(-nv:nv,nsamp/sample_stride))
allocate(freq(nsamp/sample_stride))
open(11,file="shotloc.dat",form="formatted",status="unknown")
read(11,*) nshot
allocate(shotloc(2,nshot)) !! 2 since 2D
do i = 1, nshot
read(11,*) tmp1, shotloc(1,i), tmp2, shotloc(2,i)
end do
close(11)
open(12,file="recvloc.dat",form="formatted",status="unknown")
read(12,*) nrecv
allocate(recvloc(2,nrecv)) !! 2 since 2D
do i = 1, nrecv
read(12,*) tmp1, recvloc(1,i), tmp2, recvloc(2,i)
end do
close(12)
sweep = 0.0
call csrc(sweep)
end if
open (30, file = "panel.dat", form = "formatted",&
status = "unknown")
read (30,*) maxpanel
allocate(min_trace(maxpanel),max_trace(maxpanel))
nsamp = tsamp+nsweep-1
vz = 0.0
nrecl = 4*tsamp*nrecv
open(81,file="vz_seismic.bin",form="unformatted",&
access="direct",status="unknown",&
recl=nrecl)
ipanel = 0
```

```
do ishot = 1, nshot
read(81,rec=ishot) ((vz(i,j),i=1,tsamp),j=1,nrecv) !! Read seismics to vz
do j = 1, nrecv
vz(:,j) = vz(:,j)/max(maxval(abs(vz(:,j))),0.0000000001)
end do
min_trace = 100000
max_trace = -1
read(30,*) npanel
do i = 1, npanel
read (30,*) min_trace(i), max_trace(i)
end do
array_block = 0.0
do irecv = minval(min_trace), maxval(max_trace)
do n = sample_stride,nsamp,sample_stride
summ=0.0
do l=max(1,n+1-tsamp),min(nsweep,n)
summ=summ+sweep(l)*vz((n+1)-l,irecv)
enddo
array_block(n/sample_stride,irecv)=summ
enddo
enddo
nsamp = nsamp / sample_stride
call phasevel_comp(array_block,ipanel,nfreq,npanel)
end do ! ishot
close(81)
close(30)
close(32)
deallocate(max_trace,min_trace)
nf_out = nf
first_time = .false.
end subroutine slantstack_run
```

```
subroutine slantstack_final
if (allocated(sweep)) deallocate(sweep)
if (allocated(vz)) deallocate(vz)
if (allocated(array_block)) deallocate(array_block)
if (allocated(shotloc)) deallocate(shotloc)
if (allocated(recvloc)) deallocate(recvloc)
if (allocated(min_trace)) deallocate(min_trace)
if (allocated(max_trace)) deallocate(max_trace)
if (allocated(time_velocity_vec)) deallocate(time_velocity_vec)
if (allocated(time_amplitude_vec)) deallocate(time_amplitude_vec)
if (allocated(freq)) deallocate(freq)
end subroutine slantstack_final
subroutine csrc (src)
real(8), intent(inout) :: src(:)
integer :: i, nrecl
real(8) :: pi, t, difr
pi=3.1415926
difr = pi*(fmax-fmin)/tmax
do i = 1,nsweep
t=(i-1)*dt
src(i) = sin(2*pi*fmin*t + difr*t*t)
enddo
nrecl = 4*nsweep
open(20,file="srcsweep.bin",form="unformatted",&
access="direct",&
status="unknown",&
recl=nrecl)
write(20,rec=1) (real(src(i),4),i=1,nsweep)
close(20)
end subroutine csrc
subroutine phasevel_comp(array_block,ipanel,nfreq,npanel)
```

```
real(8), intent(in) :: array_block(:,:)
integer, intent(inout) :: ipanel
integer, intent(inout) :: nfreq(:)
integer, intent(in) :: npanel
integer q,mid_trace
integer i,j,k,ii,ioffset,pan,imin
character*60 str
real(8) dv,velocity,dtv, df
real(8) dist,time,ds,vel,fre
dv = (vmax-vmin)/(nv-1)
df = (fmax-fmin)/(nsamp-1)
dtv = dt*vmax
do pan = 1, npanel
ipanel = ipanel + 1
write(str,'(A,I4,A)') 'dispe', ipanel,'.bin'
do q = 6, 8
if (str(q:q).eq." ") str(q:q) = "0"
end do
open (31, file = str(1:13), form = "unformatted", status = "unknown", &
access="direct",recl=8*(2*nv+2))
mid_trace = (min_trace(pan)+max_trace(pan))/2
time_velocity_vec = 0.0
time_amplitude_vec = 0.0
ds = 1.0D0 !! 2DO Hardcoded FIX!
do irecv = min_trace(pan), max_trace(pan)
dist = (irecv-mid_trace)*ds !! Ignore variation in depth!!
do j = -nv,nv
if (j == 0) cycle
velocity = vmin+(abs(j)-1)*dv
if (j ¡ 0) velocity = -velocity
do i = 1, nsamp
```

```
time = dist/velocity
ioffset = ((1.0/dt)*time) + sign(0.5D0,time)
if (ioffset ¿= 1-i .and. ioffset ¡= nsamp-i) then
time_velocity_vec(j,i) = time_velocity_vec(j,i) &
+ (array_block(i+ioffset,irecv))
end if
enddo !irecv
enddo !j
enddo !irecv
ii = 1
imin = 0
do i = 2, nsamp
if (array_block(i-1,mid_trace) .lt. 0 .and. &
array_block(i,mid_trace) .gt. 0) then
fre = fmin + (i-1)*df
do j = -nv, nv
if (j == 0) cycle
vel = vmin + (j-1)*dv
enddo
time_amplitude_vec(:,ii) = dtv*time_amplitude_vec(:,ii)/(i-imin)
freq(ii) = fre
if (ii¿=2 .and. freq(ii) ¡ freq(ii-1)) print *, 'WARNING Decreasing freq'
ii = ii+1
imin = i
endif
time_amplitude_vec(:,ii) = time_amplitude_vec(:,ii) + &
time_velocity_vec(:,i)**2
enddo !i
nf = ii-1
nfreq(ipanel) = nf
time_amplitude_vec(:,1:nf) = time_amplitude_vec(:,1:nf) / &
```

```
maxval(abs(time_amplitude_vec(:,1:nf)))
do ii = 1, nf
iii = iii + 1
write(31,rec=ii) freq(ii),(time_amplitude_vec(j,ii),j=-nv,nv)
write(32,rec=iii) (real(time_amplitude_vec(j,ii),4),j=-nv,nv)
end do
close (31)
enddo !pan
end subroutine phasevel_comp
end module Slantstack
```

A.5 VFSR Inversion

```
PROGRAM SIMANN
use Inversion
use Slantstack
use Elastic2D
implicit none
integer, parameter :: fp = 8, N=70
real(fp), parameter :: one=1.0_fp, two=2.0_fp, zero=0.0_fp
real(fp) :: X(N),XN(N),XOPT(N),XOPT2(N),FOPT2
real(fp) :: F,FN,FOPT
real(fp) :: LB(N),UB(N),LB0(N),UB0(N)
real(fp) :: C(N),T(N),Tp(N),T0(N),DX(N),S(N),Sp(N),kp(N)
real(fp) :: EPS,P,PP,TMIN,qq,SMAX
integer :: i, it, nt, rand1, rand2, k, maxiter, MAXOPT, NOPT
MAXOPT = 3 !! #opts before reannealing
NOPT = 0 !! #opts since last reannealing
EPS = 1.0D-6 ! Not used
maxiter = 2000000
rand1 = 47
```

```
rand2 = 11
NT = 20
qq = 0.70_fp
open(71, FILE='cost.txt')
open(72, FILE='param.txt')
open(73, FILE='optcost.txt')
open(74, FILE='optparam.txt')
open(75, FILE='temperature.txt')
write(71,*) "Cost function values"
write(72,*) "Parameter values"
write(73,*) "Optimal cost function values"
write(74,*) "Optimal parameter values"
write(75,*) "Temperatures"
call read_param(X,LB,UB,LB0,UB0,T0,DX,C,n)
print *, "Initial parameter list with bounds"
do i = 1, N
print "(I4,F9.4,A,F9.4,A,F9.4)", i, LB(i), "←", X(i), "←", UB(i)
end do
T = T0
Tp = T0

Sp = one CALL FCN(N,X,LB,UB,LB0,UB0,F)
XOPT = X
FOPT = F
write(73,*) FOPT
write(74,*) XOPT
call system("cp amplitudes.bin refamp.bin")
flush(73)
flush(74)
call reanneal
call init_random_seed
```

```
do k = 1, maxiter !! Outermost loop
do it = 1, nt !! Loop with same temperature
!! Update each parameter separately
call random_number(XN)
XN = sign(one, two*XN-one)*Tp * &
((one+one/max(Tp,1.0D-50))**abs((two*XN-one))-one)
do i = 1, N
if (XN(i) < zero) then
XN(i) = X(i) + XN(i)*(UB(i)-X(i))
else
XN(i) = X(i) + XN(i)*(X(i)-LB(i))
end if
end do
CALL FCN(N,XN,LB,UB,LB0,UB0,FN)
if (FN łF) then !! Parameters accepted
X = XN
F = FN
if (FN łFOPT)
NOPT = NOPT + 1
XOPT = X
FOPT = F
write(73,*) FOPT
write(74,*) XOPT
flush(73)
flush(74)
call system("cp amplitudes.bin refamp.bin")
end if
else !! Update sometimes
P = exp(-(FN-F)/TMIN)
call random_number(PP)
if (P > PP) then
```

```
X = XN
F = FN
end if
end if
if (NOPT >= MAXOPT) then
NOPT = 0
call reanneal
end if
end do !! it = 1, nt
X = XOPT
F = FOPT
kp = (log(Sp*T0/max(Tp,1.0D-50))/C)**(one/qq)
T = T0*exp(-C*(kp+one)**qq)
Tp = Sp*T
TMIN = minval(Tp,Tp>=1.0D-50)
print *, 'New temperatures: ', k, TMIN
write(75,*) (Tp(i),i=1,N)
flush(75)
end do !! k = 1, maxiter
close(71)
close(72)
close(73)
close(74)
close(75)
CONTAINS
SUBROUTINE FCN(N,X,LB,UB,LB0,UB0,H)
use Inversion
use Slantstack
use Elastic2D
integer, intent(in) :: N
real(fp), intent(inout) :: X(:)
```

```
real(fp), intent(inout) :: LB(:)
real(fp), intent(inout) :: UB(:)
real(fp), intent(in) :: LB0(:)
real(fp), intent(in) :: UB0(:)
real(fp), intent(out) :: H
integer :: nv, nfmod,i, ndisp
real(fp) :: vsmin, vsmax
real(fp) :: costfun
parameter (vsmin = 100.0)
parameter (vsmax = 500.0)
parameter (nv = 70 )
parameter (ndisp = 24 )
integer :: nfreq_mod(ndisp)
integer :: nfreq_ref(ndisp)
open (11,file='Ref/nfreq_ref.dat')
read(11,*) nfreq_ref
close(11)
call update_param(X,LB,UB,LB0,UB0,n)
call solve
call slantstack_run(vsmin,vsmax,nv,nfmod,ndisp,nfreq_mod)
if (minval(nfreq_ref)==0) then
print *, 'WARNING! nfreq_ref = ', nfreq_ref
H = 100.0D0
return
end if
if (minval(nfreq_mod)==0) then
print *, 'WARNING! nfreq_mod = ', nfreq_mod
H = 100.0D0
return
end if
H = costfun(nv,ndisp,nfreq_ref,nfreq_mod)
```

```
print *, 'Function evaluation is = ', H
write(71,*) H
write(72,*) (real(X(i),4),i=1,n)
flush(71)
flush(72)
END SUBROUTINE FCN
SUBROUTINE init_random_seed()
INTEGER :: i, n, clock
INTEGER, DIMENSION(:), ALLOCATABLE :: seed
CALL RANDOM_SEED(size = n)
ALLOCATE(seed(n))
CALL SYSTEM_CLOCK(COUNT=clock)
seed = clock + 37 * (/ (i - 1, i = 1, n) /)
CALL RANDOM_SEED(PUT = seed)
DEALLOCATE(seed)
END SUBROUTINE init_random_seed
subroutine reanneal
real(fp) :: hh
write(99,*) k, it, "START REANNEALING"
write(99,*) 'T', (Tp(i),i=1,N)
flush(99)
XN = XOPT
XOPT2 = XOPT
FOPT2 = FOPT
do i = 1, N
if (Tp(i) ł1.0D-50) then
T(i) = zero
S(i) = zero
cycle
end if
write(99,*) i
```

```
hh = min(DX(i),0.5_fp*(UB(i)-LB(i)))
XN(i) = XOPT(i) + hh
if (XN(i) >= UB(i)) then
XN(i) = XOPT(i) - hh
end if
CALL FCN(N,XN,LB,UB,LB0,UB0,S(i))
if (S(i) ‹FOPT2) then
FOPT2 = S(i)
XOPT2 = XN
write(73,*) FOPT2
write(74,*) XOPT2
flush(73)
flush(74)
end if
S(i) = max(abs(S(i)-FOPT)/max(abs(XN(i)-XOPT(i)),1.0D-8),1.0D-8)
XN(i) = XOPT(i)
end do
i = maxloc(S,1)
SMAX = S(i)
Sp = zero
where (S > zero) Sp = SMAX/S
Tp = Sp*T
TMIN = minval(Tp,Tp>=1.0D-50)
print *, 'New temperatures after re-annealing: ', TMIN
write(75,*) (Tp(i),i=1,N)
flush(75)
write(99,*) 'S', (S(i),i=1,N)
write(99,*) 'SMAX', SMAX
write(99,*) 'Sp', (Sp(i),i=1,N)
write(99,*) 'T', (Tp(i),i=1,N)
write(99,*) 'TMIN', TMIN
```

```
flush(99)
if (FOPT2 łFOPT) then
FOPT = FOPT2
XOPT = XOPT2
call system("cp amplitudes.bin refamp.bin")
end if
end subroutine reanneal
END PROGRAM
```

Appendix B

Numerical Inversion

VFSR inversion method was tested for several geological models with known parameters before it was implemented to Stellarton data set. In this study different starting guesses were considered in order to regenerate the reference model through inversion using VFSR. It was also tested whether the location of anomalies can be regenerated if background structure in the first guess model is different than the reference model. This method can retrieve the subsurface geology as well the associated material properties, if the parameters for the starting guess are close to the reference parameters. This appendix contains the test results of numerical inversion using VFSR and its limitations.

B.1 First Guess Model-1

Reference model in all inversion study has six dipping layers and four circular anomalies. The first test for the inversion was performed with a starting guess model with same background structures and material properties as in the reference model. The location of anomalies were perturbed in the starting guess. It was observed that inverted image did retrieve the locations of anomaly as shown in Figure B.1. The difference between reference and inverted models is given in Figure B.3.

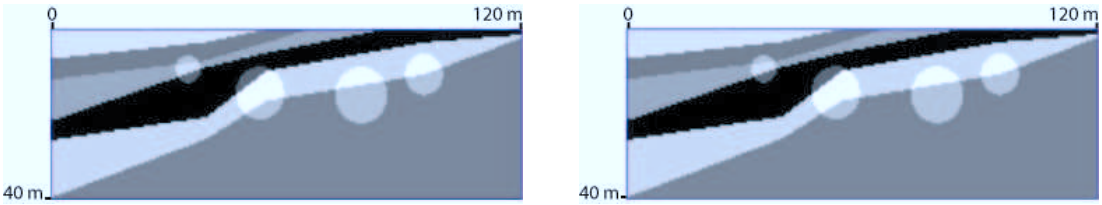

Figure B.1: Reference model (left)and inverted model (right).

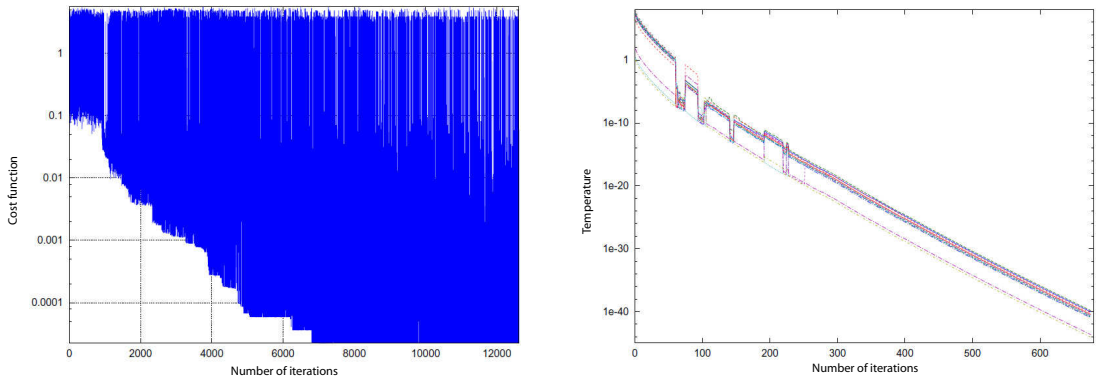

Figure B.2: Cost function (left)and temperature (right) for reannealing.

Figure B.3: Difference of inverted and reference model.

B.2 First Guess Model-2

The back ground structure of first guess model was kept same as in the reference model. The P wave velocity of each layer of first guess model has changed to ± 4% of reference model and location of the anomalies were perturbed. In this case, anomaly locations were retrieved in the inverted model as shown in Figure B.4 and the difference between reference and inverted image is presented in the Figure B.6.

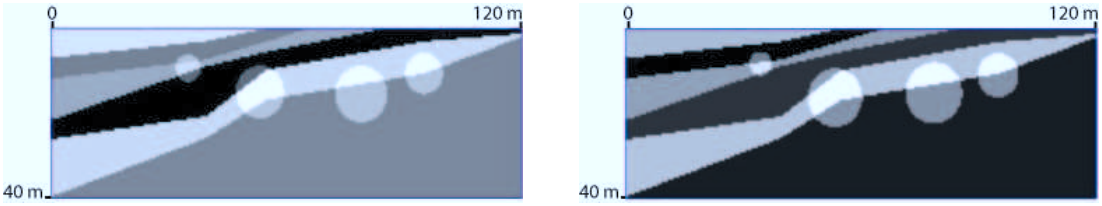

Figure B.4: Reference model (left)and inverted model (right).

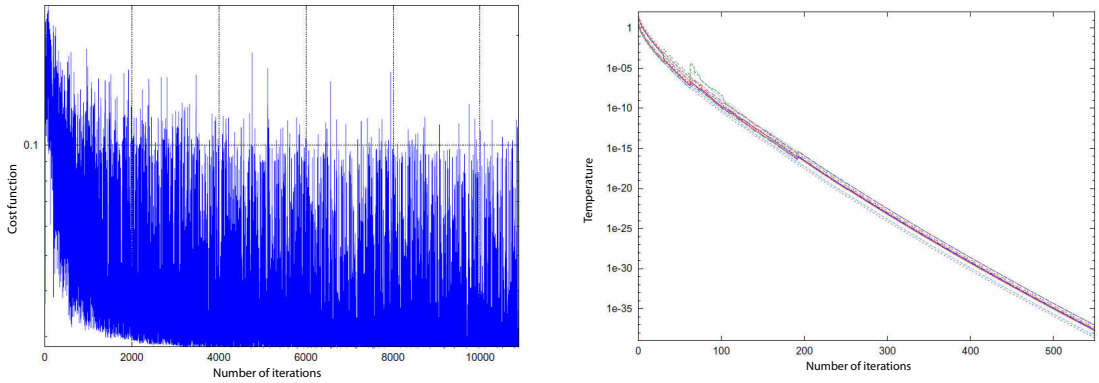

Figure B.5: Cost function (left)and temperature (right) for reannealing.

Figure B.6: Difference of inverted and reference model.

B.3 First Guess Model-3

The background structure of first guess model was kept same as in the reference model. The S wave velocity of each layer of first guess model has changed to ± 4% of reference model and locations of the anomaly were perturbed. In this case, three of the anomaly locations were retrieved in the inverted model as shown in Figure B.7. One anomaly which is located in the far right side of the model was not able to regenerate. The difference between reference and inverted image is shown in the Figure B.9.

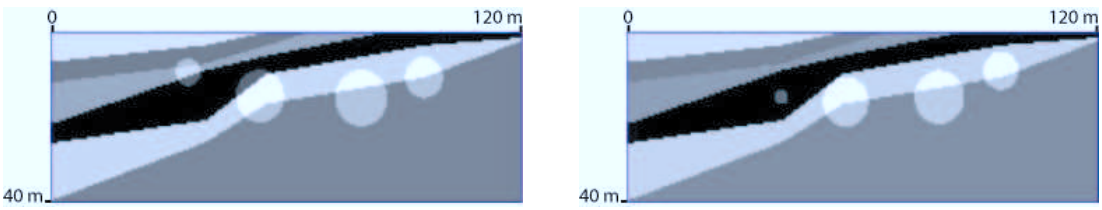

Figure B.7: Reference model (left)and inverted model (right).

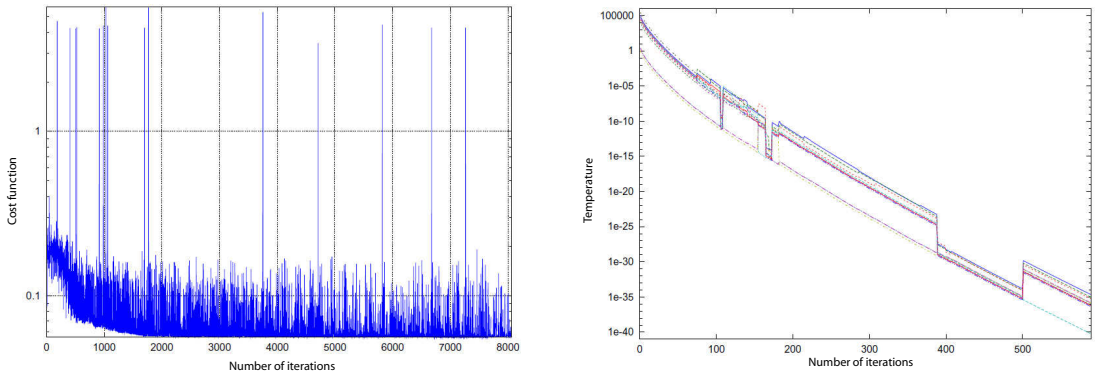

Figure B.8: Cost function (left)and temperature (right) for reannealing.

Figure B.9: Difference of inverted and reference model.

B.4 First Guess Model-4

The background structure of first guess model was kept same as in the reference model. The density of each layer of first guess model has changed to ± 4% of reference model and locations of the anomaly were perturbed. In this case, the locations of all four anomaly were regenerated after inversion as shown in Figure B.10. The difference between reference and inverted image is shown in the Figure B.12.

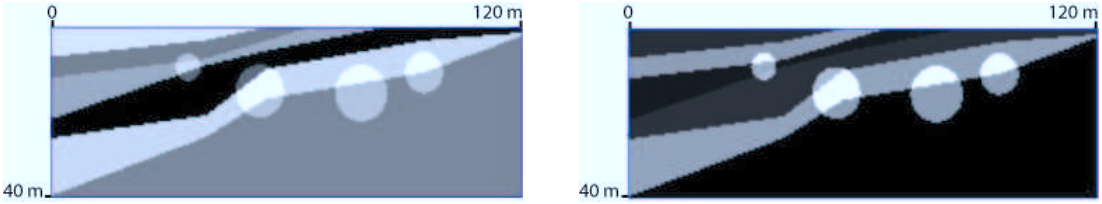

Figure B.10: Reference model (left)and inverted model (right).

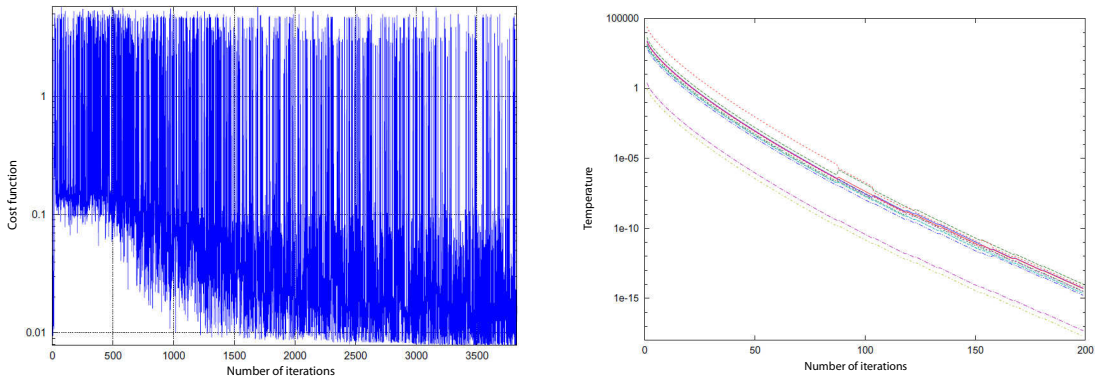

Figure B.11: Cost function (left)and temperature (right) for reannealing.

Figure B.12: Difference of inverted and reference model.

B.5 First Guess Model-5

The background structure of first guess model was changed by rotating fifth layer and locations of the anomaly were perturbed. In this case, the locations all four anomaly were not be able to regenerate after inversion as shown in Figure B.13. The difference between reference and inverted image is shown in the Figure B.15.

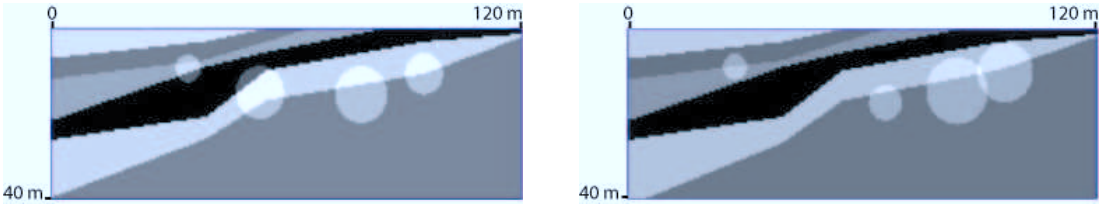

Figure B.13: Reference model (left) and inverted model (right).

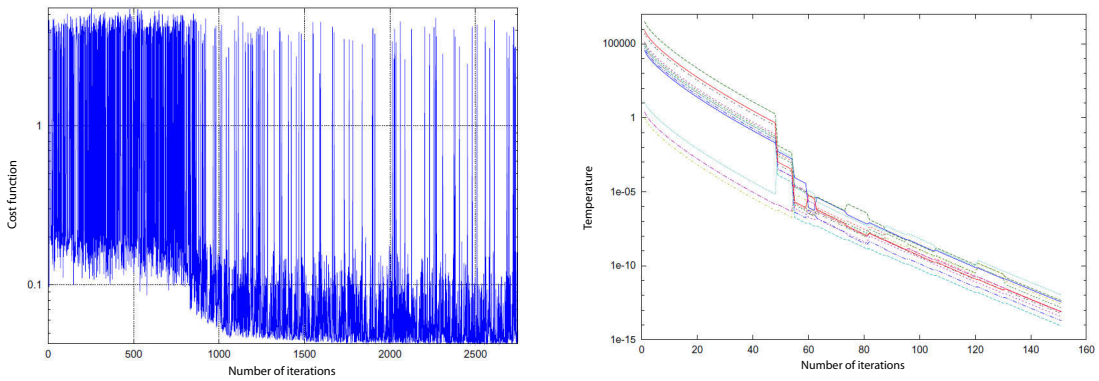

Figure B.14: Cost function (left)and temperature (right) for reannealing.

Figure B.15: Difference of inverted and reference model.

B.6 First Guess Model-6

The fifth layer in first guess model was moved upto 2 meters and locations of the anomaly were perturbed. In this case, the location of anomaly were not be able to regenerate after inversion as shown in Figure B.16. The difference between reference and inverted image is shown in the Figure B.18.

B.7 Results Summary of Inverse Modeling

- Subsurface geometry can be retrieved using VFSR inversion, if the parameters for starting guess are close to the reference data.
- In order to obtain the locations of anomaly, it is recommended that inversion using VFSR should be performed in two sages. First stage involves inverting the background structure and the second stage involves inversion of locations of the anomaly.

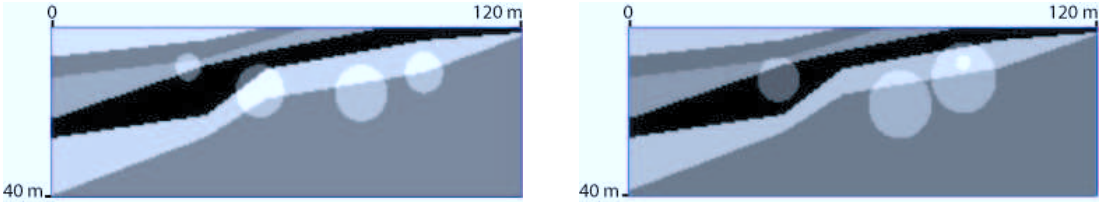

Figure B.16: Reference model (left) and inverted model (right).

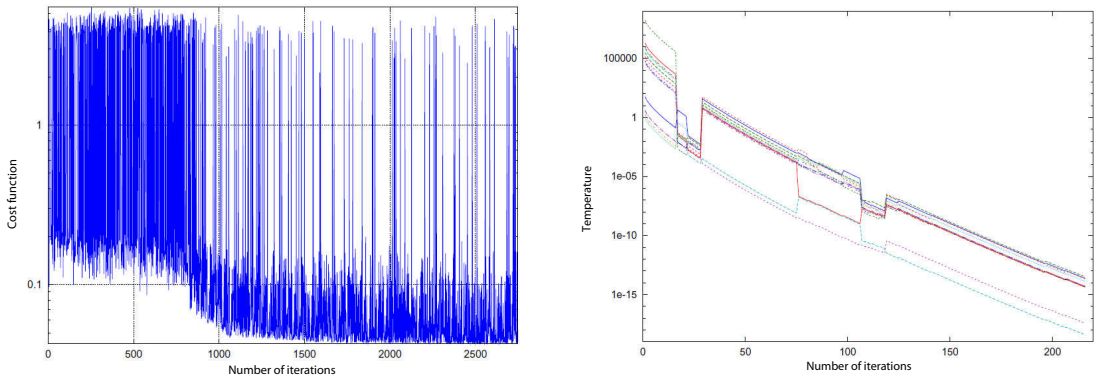

Figure B.17: Cost function (left)and temperature (right) for reannealing.

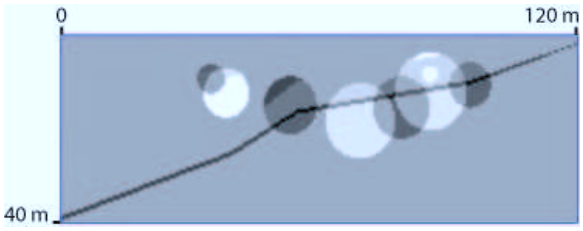

Figure B.18: Difference of inverted and reference model.